Green superlubricity mechanisms of OH-containing lubricants for hard carbon and Si-based materials

Yun Long

THESE de DOCTORAT DE L'UNIVERSITE DE LYON
opérée au sein de l'Ecole centrale de Lyon

Ecole Doctorale des Matériaux de Lyon (ED N°34)

Spécialité de doctorat :
Génie des Matériaux

Soutenue le 10 Décembre 2020, par :

Yun LONG

N°d'ordre NNT: 2020LYSEC40

Green superlubricity mechanisms of OH-containing lubricants for hard carbon coatings and Si-based ceramics

Mécanismes de supraglissement durables pour céramiques à base de silicium et revêtements DLC

Devant le jury composé de : Prof.Moseler Michael (président du jury)

Spencer, Nicholas	Professeur, ETH Zurich	Rapporteur
Donnet, Christophe	Professeur, Université Jean Monnet	Rapporteur
Moseler, Michael	Professeur, Fraunhofer institute	Examinateur
Luo, Jianbin	Professeur, Tsinghua University	Examinateur
Lubrecht, Ton	Professeur, INSA Lyon	Examinateur
Dörr, Nicole	Maître de conférences, AC2T	Examinatrice
Thiebaut, Benoit	Total	Invité
De Barros Bouchet, Maria-Isabel	Maître de conférences, ECL	Directrice de thèse
Martin, Jean-Michel	Professeur, ECL	Co-Directeur de thèse

Abstract

The trends toward greater energy conservation and the reduction of greenhouse gases demand a reduction in the fuel consumption of mechanical systems. Solid and liquid lubrications may play essential roles in energy preservation, as many moving parts are present in mechanical systems. In recent years, significant improvements in lowering energy consumption have been achieved by lowering the friction.

A number of hard materials such as diamond-like-carbon (DLC) and silicon-based ceramics (SiC and Si_3N_4) have been studied as solid lubricants for over two decades owing to their exceptional tribological and mechanical properties, such as low friction. A unique tribological feature of certain ceramics is their ultra-low friction force (0.01 <friction coefficient (CoF) <0.1) in the presence of biodegradable, green lubricants such as water, alcohols, or unsaturated fatty acids. Therefore, the prospect of achieving "near-zero" friction or "superlubricity" (CoF <0.01) by identifying specific types of material tribopairs, lubricants, and test conditions is extremely valuable for preserving not only energy resources but also for protecting our planet from catastrophic health and environmental disasters.

However, in contrast to DLC coatings, water lubrication of certain hard ceramic materials, primarily SiC and Si_3N_4, provides superlow frictions after significant tribochemical wear of the material in the contact zone that involves gross material removal and a decrease in the contact pressure, finally leading to lubrication by a hydrodynamic film.

Thus, further decreasing the CoF of DLC coatings and Si-based ceramics without excessive wear scarring has garnered significant research attention. Experiments have been attempted by adding acid, salt, nanoparticles, and long chain polymers to water. However, the majority of these experiments require a high sliding speed to realize superlow friction.

In this thesis, alternative means to minimize friction and wear, and to achieve superlubricity are demonstrated. The goal is to generate low-friction termination surfaces in situ and/or carbonaceous frictionless species. For instance, by analyzing the wear of steel after the friction of a steel/ta-C DLC tribopair in glycerol, a strong FeOOH signal was detected. The OH branches in FeOOH serve as a low friction ‘brush’ and prohibit the formation of strong interfacial bonding. Interestingly, by changing from steel/ta-C to Si_3N_4/Si_3N_4, the chemical reaction between glycerol and Si_3N_4 drove the generation of graphene-nitride nanolayers, which controlled the superlubricity over a wide range of temperatures. Inspired by this result,

hypericin, a molecule rich in 6-fold carbon rings, was directly added to glycerol. The presence of hypericin sharply reduced the running-in time of the steel/SiC pair, achieving superlubricity. Unlike other aromatic additives, this molecule exhibits great affinity to the steel surface and continuously feeds the contact zone during the friction process. Moreover, hypericin seems to be photosensitive, which impacts its friction performance.

Recent research performed by De Barros Bouchet et al. and Takuya et al. illustrated that tribo- and/or mechano-chemical reactions can rehybridize the ta-C surface from sp^3 to sp^2 orbitals. Therefore, the tribological performance differences between a-C and ta-C were directly compared in vegetable castor oil. sp^2-rich carbon film a-C exhibits lower friction than sp^3-rich carbon film ta-C under identical lubrication conditions, and the sliding speed required to reach superlubricity was slower for a-C. Furthermore, by tailoring the tribopair, the importance of amorphous a-C, with a high sp^2/sp^3 ratio and interesting mechanical properties, is emphasized to achieve superlubricity in castor oil. Steel/steel or steel/ceramic tribopairs inevitably increase the surface roughness, resulting in a CoF below 0.01.

As the primary component of castor oil, the lubricity of fatty ricinoleic acid is examined afterward. This work reveals that ricinoleic acid does not cause steel surface oxidation or increases in the surface roughness. On the contrary, when ricinoleic acid lubricates steel/Si_3N_4 under suitable conditions, superlubricity can be achieved. Owing to the presence of an OH group, the lubricity of ricinoleic acid is superior to that of oleic or linoleic acids for the steel/Si_3N_4 system. Similar to glycerol lubricating steel, the OH functionalities on fatty acid molecules prohibit interdigitation of fatty acid chains and reduce friction.

Keywords: Superlubricity mechanisms, Si-based ceramics, DLC materials, OH-based lubrication, surface aromatization, sustainable chemical polishing.

Résumé

L'efficacité énergétique et la réduction des émissions de gaz à effet de serre exigent une diminution de la consommation de carburant des systèmes mécaniques. La lubrification solide et liquide, permettant de diminuer les pertes par frottement, peut jouer un rôle essentiel dans la préservation d'énergie des systèmes mécaniques qui comportent de nombreuses pièces mobiles. Ainsi, ces dernières années, la réduction de la consommation d'énergie a été considérablement améliorée grâce à de nouvelles technologies de lubrification.

Certains matériaux durs comme les Diamond-Like-Carbon (DLC) et les céramiques à base de silicium (SiC et Si_3N_4) sont étudiés depuis plus de deux décennies comme lubrifiants solides en raison de leurs propriétés tribologiques et mécaniques exceptionnelles, en particulier un coefficient de frottement (CoF) faible. Une caractéristique tribologique unique et étonnante de certaines céramiques est leur capacité à présenter un frottement ultra-faible (CoF inférieur à 0,04) en présence de certains lubrifiants verts biodégradables comme l'eau, les alcools ou les acides gras insaturés...

Cependant, à l'opposé des revêtements DLC, la lubrification à l'eau de certaines céramiques dures, principalement SiC et Si_3N_4, fournit un frottement extrêmement faible après une forte usure tribochimique du matériau, impliquant un enlèvement brut de matière et une diminution de la pression de contact, qui provoque finalement une transition vers un régime de lubrification hydrodynamique.

Ainsi, de nombreuses études sur la manière de réduire davantage le CoF des DLC et des céramiques à base de Si sans engendrer une forte usure sont en cours. Des essais ont été faits en ajoutant de l'acide, du sel, des nanoparticules et des polymères à longue chaîne dans le solvant aqueux. Cependant, dans la plupart de ces cas, une vitesse de glissement très élevée est nécessaire pour atteindre l'objectif ci-dessus.

Dans cette thèse, nous proposons de nouvelles technologies pour atteindre des niveaux de frottement super faibles, également appelés supraglissement (CoF inférieur ou égal à 0,01) et des taux d'usures modérés. L'idée directrice est de générer *in situ* des espèces fournissant du frottement faible. Par exemple, en analysant la trace d'usure formée sur l'acier après frottement d'un tribo-couple acier/ta-C (DLC) dans le glycérol, un fort signal du composé FeOOH est détecté. Les terminaisons -OH sur le FeOOH conduisent à un faible frottement en empêchant la formation d'une liaison forte à l'interface. Il est intéressant de noter qu'en

remplaçant l'acier par le Si_3N_4, la réaction chimique entre le glycérol et ce dernier entraîne la génération de nanostructures de nitrures de graphene permettant l'obtention de supraglissement sur une plage de température très large. Inspirée par ce résultat, l'hypéricine, une molécule riche en cycles carbonés sextuples, est directement ajoutée au glycérol comme additif. Sa présence dans le glycérol réduit considérablement la période d'induction nécessaire pour atteindre le régime de supraglissement du couple acier/SiC. Contrairement à d'autres additifs aromatiques, l'hypéricine présente une grande affinité avec la surface en acier et alimente continument le contact pendant le glissement.

Les recherches les plus récentes de De Barros Bouchet and al. et Takuya and al. nous éclairent sur le fait qu'une réaction tribo- et/ou mécanochimique peut provoquer une réhybridation du carbone sp^3 vers sp^2 de la surface du ta-C. C'est pourquoi, dans l'huile de ricin, nous comparons les performances tribologique des revêtements a-C et ta-C. Le premier, riche en carbone sp^2, surpasse les performances du second en terme de réduction de frottement. De plus, le régime supraglissant est prolongé pour des vitesse de glissement plus faibles avec le a-C. De plus, l'importance du revêtement a-C pour atteindre le supraglissement en présence d'huile de ricin est mise en évidence par l'utilisation des couples acier/acier et acier/céramique qui conduisent inévitablement à une augmentation de la rugosité de surface lors du frottement provoquant une augmentation du CoF.

En tant que principal composant de l'huile de ricin, le pouvoir lubrifiant de l'acide ricinoléique est étudié. Ce travail révèle que l'acide ricinoléique n'est pas la cause d'une oxydation de la surface de l'acier et de l'augmentation de la rugosité de surface. Au contraire, lorsqu'il lubrifie le couple acier/Si_3N_4 dans des conditions appropriées, le supraglissement peut être établie. De plus, en raison de la présence d'un groupement OH sur sa molécule, son pouvoir lubrifiant est supérieur à celui de l'acide oléique et de l'acide linoléique pour le couple acier/Si_3N_4. Comme dans le cas de l'acier lubrifié au glycérol, la fonction -OH de la molécule d'acide gras permet de limiter l'interaction entre les chaînes d'acides gras réduisant ainsi le frottement.

Mots clés : Supraglissement, céramiques à base de Si, revêtements DLC, lubrification aqueuse, polissage chimique, aromatisation de surface.

Contents

General introduction 10
1. Introduction and state of the art 12
1.1. Types of superlubricity 13
1.2. Lubricity in vacuum and gas 15
1.2.1. Superlubricity of the DLC family 15
1.2.2. Superlubricity of transition metal dichalcogenide 20
1.3. Superlubricity in liquids 21
1.3.1. Water 21
1.3.2. Polyalkylene glycol (PAG) 23
1.3.3. Phosphoric acid 24
1.3.4. Saturated and unsaturated fatty acids 28
1.3.5. Polyols 30
1.3.6. Glyceride of fatty acid 33
1.4. Additives 35
1.4.1. Silica 35
1.4.2. Graphitic materials 37
1.5. References 40
2. Methods and calculations 48
2.1. Introduction of tribometer and measured CoF. 49
2.2. Central film thickness calculations 50
2.3. Theoretical CoF arisen from liquid (Couette flow) 51
2.4. Flash temperature calculation. 52
2.5. Analytical tools 52
2.6. The information depth calculation of element peak from XPS 53
2.7. Surface roughness, the radius of ball curvature, wear volume obtained from the interferometer. 53
2.8. References 54
3. Superlubricity in vacuum 55
3.1. Wearless superlubricity by sliding Si_3N_4/aC:H in ultrahigh vacuum 56
3.1.1. Experimental parts 56
3.1.2. Results 56
3.1.3. Conclusions 60
3.2. References 61
4. Superlubricity in polyols 62

4.1. Superlubricity of glycerol by self-sustained chemical polishing: the case of steel/ta-C in glycerol 63
Sci.Rep. Doi:10.1038/s41598-019-42730-9 63
4.1.1. Experimental parts 63
4.1.2. Results 64
4.1.3. Discussions 70
4.1.4. Conclusions 76
4.2. In situ synthesis of graphene-nitride nanolayers on glycerol-lubricated Si_3N_4 surfaces leads to superlubricity 77
Accepted by ACS Appl. Nano Mater. 77
4.2.1. Experimental parts 77
4.2.2. Results 77
4.2.3. Discussions 85
4.2.4. Conclusions 87
4.3. Superlubricity induced by long-term sliding of steel/SiC in glycerol 88
4.3.1. Experimental parts 88
4.3.2. Results 89
4.3.3. Discussions 96
4.3.4. Conclusions 98
4.4. Superlubricity enabled by antiviral – hypericin 99
4.4.1. Experimental parts 99
4.4.2. Friction results 99
4.4.3. Discussions 105
4.4.4. Conclusions 107
4.5. References 108
5. Superlubricity in vegetable oils 112
5.1. Controllable green superlubricity of amorphous carbon/Si_3N_4 tribopair assisted by castor oil 113
Under review of Carbon 113
5.1.1. Experimental parts 113
5.1.2. Results 114
5.1.3. Discussions 122
5.1.4. Conclusions 123
5.2. Role of tribo-pair for reaching superlubricity in castor oil 124
5.2.1. Experimental parts 124
5.2.2. Results 125
5.2.3. The key to superlubricity in castor oil 131
5.2.4. Conclusions 134

5.3. References 135
6. Superlubricity of fatty acids 138
6.1. Improving C_{18} fatty acid lubrication performances: investigating the role of C=C and OH function groups in the aliphatic chain 139
6.1.1. Experimental parts 139
6.1.2. Results 140
6.1.3. Superlubricity 145
6.1.4. Conclusions 147
6.2. References 148
7. Summaries and perspectives of Ph.D. work 149
7.1. Vacuum 150
7.2. Glycerol 151
7.3. Glycerol+hypericin 153
7.4. Castor oil 153
7.5. Ricinoleic acid 154
7.6. General mechanism 154
7.7. Perspectives 155
7.8. References 157

General introduction

The industrial revolution has not only brought prosperity to modern society but has also aggravated environmental pollution to a significant level. It has triggered severe problems such as global warming, resource scarcity, and energy crisis. Globally, governments have implemented environmental protection acts and actively encourage citizens to purchase fuel-efficient vehicles. The high frictions and thermal efficiencies of traditional motor vehicles limit their lifetime, emit toxic gases such as carbon dioxide and nitrogen oxides, and increase energy consumption.

Recently, Kenneth et al. reported that 20% of the world's total energy consumption can be traced back to friction and insufficient lubrication technologies. However, it may be possible to reduce total energy consumption by 8.7% and CO_2 emission by 3.140 million tons in fifteen years.[1] Apart from reducing friction, lubrication technologies can also provide wear protection to tribological components. Lubrication prolongs the lifetime of machinery by protecting raw materials. Therefore, global requirements for lubricants have remained high (approximately 35 million tons) between 2010 and 2015.[2]

Lubricants are widely applied in internal combustion engines, motors of vehicles, turbines, and so on. To augment the performance of lubricants, such as anti-wear, anticorrosion, and low friction between components, sulfur- or phosphorous-based additives have been inserted in the lubricant. For example, utilizing sulfur under extreme pressures can prevent scuffing and galling. However, these additives are toxic to humans and the environment. Therefore, it is important to develop biodegradable, green lubricants.

Simultaneously, these new eco-friendly lubricants should operate more efficiently than traditional mineral lubricants. Two general pathways are employed to improve lubricant performance: exchanging lubricants with alternative performants, such as vegetable oil (sunflower oil, soybean oil[3], castor oil[4] etc.) and mixing lubricant with additives (graphene oxide-GO[5], black phosphorus[6], nanoparticles[7] etc.). The ultimate goal is to make friction disappear. To date, a regime that approaches this goal is called superlubricity, also defined by a kinetic friction coefficient (CoF) <0.01[8].

In this research, a low friction state is realized using hard ceramic materials such as silicon nitride (Si_3N_4) and silicon carbide (SiC) owing to their superior hardness and high resistance to wear and heat. Moreover, they are electrically non-conductive and exhibit minimal thermal

expansion, enabling chemical stability and suitability for application under severe conditions. Diamond-like carbon is also examined in this work since, even in non-lubricated conditions, it is chemically stable and exhibits low friction and high resistance to wear. The tribological performances of hard materials have been modified by incorporating biodegradable lubricants (alcohols, unsaturated fatty acids, and vegetable oils). Various experimental processes are performed to determine the best combination of hard solid materials and green lubricants with respect to tribological performances. The mechanisms are thoroughly studied by analyzing and simulating tribolayers formed on rubbed surfaces. The studies and results are presented in seven chapters.

In chapter one, a brief introduction of superlubricity is presented. Subsequently, superlubricity achieved in vacuum and gas is discussed. Afterwards, superlubricity in aqueous media and vegetable oil is also presented. This chapter concludes with the effect of additives in liquid.

In chapter two, the experimental instruments are illustrated and discussed. In addition, theoretical calculations of the liquid film CoF, liquid film thickness, flash temperature, and information depth of X-ray photoelectron spectroscopy (XPS) analysis are also described.

In chapter three, superlubricity induced by film transfer of aC:H on Si_3N_4 is demonstrated.

In chapter four, three superlubricity phenomena are presented: steel/ta-C in glycerol, Si_3N_4/Si_3N_4 in glycerol, and steel/SiC in glycerol. Moreover, the effect of hypericin as an additive is also discussed.

In chapter five, superlubricity realized using castor oil is shown. This chapter includes studies on:

- how the sp^2/sp^3 ratio of ta-C influences the tribological performance.
- how different tribopairs function with lubrication by castor oil.

In chapter six, superlubricity is realized using ricinoleic acid. The effect of the OH functional group on the tribological performance of fatty acids is determined by comparing ricinoleic, oleic, and linoleic acids.

After chapter six, summaries and perspectives of this Ph.D. work are presented.

Chapter I

1. Introduction and state of the art

1.1. Types of superlubricity

Superlubricity was discovered in a study that aimed to understand the intrinsic cause of friction [9,10]. Friction occurs when translational kinetic energy is converted into internal kinetic energy. However, if no such energy transition takes place, no energy dissipation occurs and a superlubric state is established. In order to maintain a constant translational kinetic energy, the sum of atomic forces should be equal to zero and the contact between surfaces should be incommensurate. In reality, friction never completely vanishes owing to limitations in the precision of measurements and other factors [11]. Therefore, superlubricity refers to a CoF <0.01 [12].

It is important to separate superlubricity realized by an elastohydrodynamic liquid (EHL) film from other types of superlubricity because, with lubrication by an EHL film, asperities are not in contact. The key to govern friction is linked to the properties of the lubricant. In general, a lubricant with a relatively low viscosity (η) and visco-pressure coefficient (a) is likely to function in the superlubric state, for instance, full film lubrication using glycerol [13], PAO (polyalphaolefin) [14] and vegetable oil [15] with suitable η and a.

In contrast to EHL lubrication, superlubricity fully or partially originates from contact with asperities and has been widely studied in the last decade. A good example of contact between asperities resulting in superlubricity is structure lubricity, where crystalline surfaces shear in an incommensurate manner. The first experimental observation of this phenomenon dates back to 1993 when the tribological performance of MoS_2 was studied under a high vacuum [16]. The superlubricity was linked to the reorientation of MoS_2 basal planes along the direction of shearing and disordered orientation to the axis perpendicular to the sliding direction. In addition, WS_2 also achieved superlubricity under a high vacuum and at a low temperature [17]. However, the underlying mechanism of superlubricity was not discussed. On the atomic scale, by sliding a tungsten tip along graphite, superlubricity periodically disappeared at every rotation angle of $61° \pm 2°$ [18]. This confirmed that the superlubricity of graphite originates from incommensurate contact between atomic layers. When graphite or MoS_2 were used directly, their tribological performance strongly relied on the orientation of atomic layers. To overcome this limitation, a graphite/hexagonal boron nitride (hBN) layered heterojunction was studied. Even at the same orientation, incommensurate contact was observed between graphite and hBN owing to the intrinsic lattice vector misfit [19].

Superlubricity arising from incommensurate contact was observed at the macroscale in dry air for the first time [20], where nano-diamond particles and graphene were deposited on SiO_2. Under shearing, graphene nanoscrolls were generated when the graphene wrapped around the nano-diamond particles. Hence, an incommensurate contact was established. Similarly, by depositing MoS_2 and nano-diamond particles on SiO_2 and sliding against a H-DLC(hydrogenated diamond like carbon) in nitrogen, superlubricity was also achieved. Incommensurate contact was generated by the formation of onion-like carbon (here, carbon originated from the graphitization of nano-diamond particles).

In addition to structural superlubricity, the superlubricity of a hydrogenated DLC in vacuum has been thoroughly studied and applied in aerospace machinery. The superlubricity stemmed from hydrogen passivation. Therefore, the hydrogen content is crucial[21]. More details are provided in the following section.

Superlubricity can also be achieved by grafting long polymer chains on various surfaces. The loading capacity of the polymer layers significantly increased under shearing due to the repulsive force between polymer layers [22]. In particular, charged polymer chains (polyelectrolytes) prohibited the interpenetration of polymer brushes and hence reduced energy dissipation. Moreover, a hydration layer is expected to be formed on charged species. Profiting from both polymer and hydration layer separation, a CoF as low as 0.0006 was observed. However, when the average pressure was above 0.3 MPa, the polymer chains were sheared off the surfaces, and the friction increased[23].

Superlubricity can also be achieved by liquid and surface functionalization; for example, the repulsion between charged surfaces [24], and the formation of easy-shear layers such as a hydrogen-bonded layer [25], silica layer[26], etc. on the surface. More details are provided in the next section. However, once a liquid makes contact, it is difficult to determine whether or not superlubricity only originates from contact between asperities. In general, when lambda is less than one, the liquid contribution can be neglected. However, the removal of lubricants[27] and a decrease in the sliding speed[5] eventually increase the friction. Additional research is required in this regard.

1.2. Lubricity in vacuum and gas

1.2.1. Superlubricity of the DLC family

The environment has a significant influence on the performance of DLC coatings. Choosing the best combination of DLC types and the environment is fundamental for reducing wear and friction. In a high vacuum (10^{-6} Pa), the CoF of self-mated ta-C stabilized at approximately 0.6 in 2 min, while that of aC:H stabilized with a value below 0.01. Interestingly, no wear track was observed when aC:H was used[28]. The high friction of ta-C in a vacuum was explained by the formation of a strong covalent C–C interfacial bond[29].

Unlike ta-C, the surface of aC:H is passivated by H terminations, inhibiting the formation of interfacial bonds and resulting in low friction. However, the duration of superlubricity achieved by aC:H is strongly associated with the hydrogen content. For aC:H samples with hydrogen contents below or equal to 34%, a CoF of approximately 0.6 was obtained after a short stay in the superlubricity regime. When the friction sharply increased, desorption of H_2 and CH_4 was observed. Moreover, when the friction was high, the tribodesorption of gas became remarkable. This desorption was not triggered by a limited temperature rise during sliding[30]. Since the increase in friction was linked to desorption of H_2, the H_2 content was maintained by conducting experiments in a hydrogen atmosphere, and this turns out to be an efficient method to retain superlubricity[31]. Another alternative is to use a high hydrogen content aC:H (40%). Compared with a 34% H content aC:H that fails to retain superlubricity after 40 cycles, superlubricity was preserved up to 500 test cycles by using a 40% H content aC:H. This difference was explained by the 40% H content aC:H possessing a significantly larger hydrogen reservoir that compensated for the loss of hydrogen during friction[21]. The hydrogen content also influenced the wear status after friction. The wear scar for the 34% H content aC:H was black with a large amount of wear debris, whereas the wear scar of the 40% H content aC:H was white and smooth.

The initial high friction of aC:H originates from interfacial bond formation since dangling bonds are present even with 45% hydrogen in the aC:H film. For the case of self-mated aC:H, unbound carbon forms interfacial bond with methylene group from the counterpart[32]. Driven by sliding, methylene group will be stripped from aC:H substrate and saturates unbound carbon. Accompanying surface saturation, the number of carbons that exist in a ring transitions from seven to five atoms. Moreover, these rings tend to align themselves parallel

to the sliding direction. This ring realignment requires an internal carbon-carbon bond to be sp^2 hybridized, not sp^3, which is perpendicular to the sliding surface. This speculation is consistent with the fact that the sp^2 content increases after interfacial friction in self-mated aC:H. In summary, interfacial bonds in aC:H are prohibited by either surface passivation or surface sp^2 hybridization.

The superlubricity of aC:H was extended by incorporation with other materials. Using a 40% hydrogen content aC:H sliding against steel, the of aC:H film was transferred onto the steel surface. The surface of steel is covered by oxide and adventitious carbon layers. To determine the role of each layer, steel was sputtered with Ar ions. The removal of adventitious carbon reduced the running-in period, while the removal of both the adventitious carbon and oxide layers enabled CoF to stabilize at lower value compared with the aC:H alone. This signifies that the adventitious carbon layer delayed the settling in of aC:H transfer[33]. It is interesting to explore whether the transferred aC:H film is the only requisite for achieving superlubricity. Steel containing transferred aC:H film was reused to slide against a different region on the aC:H. A short running-in period was always required to achieve superlubricity [34]. Unfortunately, this superlubricity was highly dependent on the hydrogen content.

The difference in hydrogen content also determines how aC:H reacts to load. For a hydrogen content higher than the superlubricity threshold, an increase in the contact pressure from 121 to 464 MPa not only reduced the running-in period but also decreased the stable CoF[35]. A high load corresponds to more compact and smoother films transferred to steel. In contrast, using an aC:H film with a hydrogen content lower than the threshold, sustainable low friction can only be obtained under a normal force equal to 1 N. Once the force is above 1 N, the CoF rapidly rises after a short running-in[36]. This result was further confirmed by simulation. Comparing two aC:H films with 30% and 45% hydrogen, a higher hydrogen content always guaranteed a lower probability to form interfacial bonds, notwithstanding whether the pressure is 1 or 5 GPa; hence, the friction curve was more stable. For the lower hydrogen content aC:H, a high load enhanced the formation of interfacial bonds, therefore, CoF was high[32]. aC:H prepared by RF high-density plasma required only 30% hydrogen to achieve superlubricity, whereas the hydrogen requisites for samples manufactured by plasma-enhanced chemical vapor deposition and plasma-assisted chemical vapor deposition were 40% and 50%, respectively[37].

To overcome the limitations of hydrogen content, surface modification and amelioration of the production process have been studied. Thermal treatment of aC:H at 300 °C led to an increase in the sp^2 fraction. This was accompanied by a slight decrease in the hydrogen content due to dissociation of the C–H bond. The final hydrogen content was calculated to be 21%. The CoF of aC:H after thermal treatment was five times lower than that without thermal treatment. Thermal treatment produced a thinner and more unified transfer film on sapphire. However, the authors attributed this superlubricity to the formation of sp^3-rich wear tracks on the aC:H disk, and the high hydrogen content provided surface passivation. The authors' argument remains questionable because they attribute the hardness and density increase inside the wear track to the increased sp^3 content. The increase in hardness and density may be caused by the removal of the oxide layer on aC:H by friction (TEM images of worn and unworn surfaces)[38]. In addition to tailoring the temperature to increase the surface sp^2 content, a more direct way is to coat graphene oxide on aC:H. aC:H alone exhibited a sharp increase in the CoF after a short stay in superlubricity. With three and five layers of graphene oxide coated on aC:H, the CoF remained at approximately 0.025 until the test ended[39].

Additionally, by tailoring the coating precursors, the sp^2 content in aC:H can be controlled. A higher H/C ratio in the precursors corresponds to a higher sp^2 content in aC:H. In dry nitrogen, the lowest CoF (0.02) was observed when highly hydrogenated and sp^2 hybridized aC:H slid against steel. The film transferred on steel was further sp^2 hybridized[40]. However, the authors changed the hydrogen and sp^2 contents simultaneously. As such, it is difficult to determine which produced the low friction.

Another option to generate low friction when the hydrogen content of aC:H is relatively low is to slide the film against Al_2O_3 and ZrO_2. Cui et al. showed that when the hydrogen content of aC:H was approximately 8%, choosing SiC and Si_3N_4 as counterpart produced a high CoF of approximately 0.5 with the formation of a carbonaceous transfer film on ceramics. However, when Al_2O_3 and ZrO_2 were chosen, the CoF remained under 0.1 with no carbonaceous transfer film generated inside the wear track. Owing to the low adhesion between Al_2O_3, ZrO_2, and aC:H films, ceramic oxides inhibited sliding between the two carbonaceous layers[41]. To date, researchers have not agreed whether the carbonaceous transfer layer should be avoided or not [42,43].

As the debate continues, a more thorough study of the aC:H film structure is required. For self-mated aC:H with 40% hydrogen, when P_{max} is under 0.93 GPa, no structural change

occurred. Superlubricity was achieved by hydrogen passivation. However, when P_{max} increased to 1.17 GPa, the CoF stabilized at 0.001, one quarter of the value of the low load case, owing to the formation of a 3 nm layer with both high sp^2 and hydrogen contents. When steel was used as a counterpart, instead of directly reacting with iron, aC:H bonded with the iron oxide layer and formed a C–Fe–O sublayer. Consequently, a hydrogenated sp^2 layer grew, serving as a driving force to achieve superlubricity. The sp^2 content of the transfer film was further increased to 80% when Si_3N_4 was employed. The other 20% of C bonding existed in the form of C–H bonds and not C–C, crucial for achieving superlubricity[44].

In terms of sliding aC:H against ceramic, besides conventional film transfer triggered by adhesion, a novel film transfer mechanism was proposed by Wang [45]. The hydrocarbons present on the DLC substrate first detached from the surface by triboemission without forming an interfacial bond. During sliding, the hydrocarbons searched for active sites and finally bonded with the SiC surface. Consequently, the aC:H film was transferred onto SiC. For aC:H, film transfer induced by hydrocarbon emission was more pronounced compared with surface adhesion. As for a-C, with no hydrogen in the bulk material, surface adhesion was the primary method of film transfer. Comparing a-C and aC:H, surface adhesion and hydrocarbon emission were more noticeable for aC:H. This indicates that the existence of hydrogen in the bulk material facilitates film transfer.

Moreover, doping an aC:H film with Si is also an alternative technique to stabilize friction at low hydrogen contents. By introducing less than 10% Si into aC:H, no dramatic increases in the CoF were observed after running-in. The CoF still varied with hydrogen content, however, it stabilized at 0.015 for aC:H with 17.3% hydrogen. Superlubricity was achieved when the hydrogen content was increased to 20%. For self-mated aC:H:Si films, a film on a ball was rapidly worn out, whereas disks exhibited a newborn tribolayer. The average thickness of this tribolayer was between 100 and 200 nm and the top surface is rich in C_xH_y species, whereas the outer wear track displayed a lower content of C_xH_y species. This suggests that the wear surface was passivated and saturated by hydrogen. It is worth noting that no phase transition was observed on the disk by Raman spectroscopy. Carbon remained in the form of sp^3 on the micron scale. In contrast, a phase transition from sp^3 to sp^2 was observed on the ball. This phase transition occurred during the running-in process and was driven by high energy dissipation and the formation of sp^2 rings oriented parallel to the sliding direction, leading to smoothening of the wear surface. Although this tribolayer most likely existed in an amorphous form on the ball, it still acted as a low friction shear band. Simultaneous surface

passivation, carbon rehybridization, and shear localization generated superlubricity[46]. A more detailed analysis was performed in a subsequent study [44]. The tribofilm thickness on the aC:H:Si ball was 18 nm with iron present since the substrate utilized was γ-Fe. This signifies that the aC:H:Si coating was removed by friction. Subsequently, the tribofilm grew on γ-Fe. A similar phenomenon was also observed for steel balls sliding against aC:H:Si disks. The C=C and C-H contents increased in the first 10 nm of the disk. Hence, both dangling bond saturation and sp^2 hybridization occurred on the aC:H:Si disk. The top 10 nm of tribofilm resembled highly hydrogenated graphite-like carbon, favoring energy dissipation. It is interesting to note that introducing Si into the aC:H film did not always decrease the friction. A low percentage of Si increased the friction and the most suitable Si percentage was 9.3%. This produced a porous structure inside the aC:H:Si film, which bore stress and began crack propagation and plastic deformation in the aC:H:Si layer. This percentage of Si also favors the generation of a polymeric tribolayer with one eighth the hardness of the original aC:H:Si film. Similar polymeric tribolayers containing highly hydrogenated graphite-like carbon were observed when the Si content was 9.3% and 5.7%, however, when the Si content was 5.7%, the CoF was 16 times higher than those samples containing 9.3% and 5.7% Si.

In terms of friction reduction, doping 5.4% oxygen into the aC:H matrix produced a CoF of 0.004 while the CoF of the pure aC:H film in a N_2 atmosphere was 0.008. The introduction of oxygen to aC:H was accompanied by a decrease in the hardness and elastic modulus. However, further augmentation of the oxygen content to 9.5% increased the CoF due to the generation of a relatively rough surface compared with aC:H containing 5.4% oxygen. Moreover, a shear band at approximately 10 nm, rich in C–O bonds, was also generated by friction. This C–O bonding formed interfacial C–O–C bonds, leading to 'cold weld'. Therefore, the friction increased[46].

Owing to the similarity of C–H and C–F bonds, the H content threshold required to activate superlubricity is drastically decreased by introducing F into aC:H. As a-C:F:H only contains 5% H and 18% F, a stable CoF of 0.005 was observed after 600 cycles [37]. Indeed, replacing H with F stabilized the CoF at superlubricity for a longer duration. However, this superlubricious state eventually collapsed [47]. Simulations showed that the uppermost carbon underwent graphitization within 0.02 ps due to plastic deformation, and this graphite layer transferred to the Fe region a short time later. Such a graphite layer on the Fe surface captured carbon from the a-C:F:H substrate and exhibited excellent adhesion. Therefore, the authors

concluded that the failure of aC:F:H in vacuum was directly linked to the formation of a graphitized carbon layer.

1.2.2. Superlubricity of transition metal dichalcogenide

Surface passivation is not the only way to achieve superlubricity in vacuum. Lamellar layers also pave the way for superlubricity. The first superlubricity demonstration in MoS_2 was reported in 1993 by sliding MoS_2 coated disks against hemispherical SiC pins in an UHV [48,49]. The superlubricity lasted 91 cycles, and a drastic increase in the CoF was recorded. Additionally, the superlubricity behavior of MoS_2 was extremely sensitive to the atmosphere. Even in HV, superlubricity was not observed and a CoF of approximately 0.012 was determined. In addition, compared with UHV, in a nitrogen atmosphere the CoF slightly increased. It is important to highlight that the manufacturing process for MoS_2 coatings should not introduce oxygen, since even 1 at% oxygen in MoS_2 leads to an increased CoF. Experimentally, exposing the MoS_2 coating to oxygen flux resulted in a stabilized CoF of 0.06. This was attributed to the substitution of S by O, which introduced atomic-scale defects and discontinuities in the smooth S plane, functioning as an energy barrier that hinders sliding. Before friction, the oxygen-free MoS_2 coating aligned perpendicular to the substrate. However, after friction, the basal plane of MoS_2 oriented in the sliding direction[50]. Within this plane, two MoS_2 sheets were superimposed at rotation angles of 16° and 29°, where the incommensurable angle of MoS_2 sheets is 30°. The misfit angle of the MoS_2 sheets is not required to be 30° to achieve superlow friction. A slight misfit angle can induce a drastic decrease in the friction. Concisely, friction drives alignment of the atomically clean MoS_2 sheets parallel to the sliding direction at a certain misfit angle owing to weak van de Waals forces between sheets. This creates an incommensurate structure, leading to friction vanishing. Superlubricity of WS_2 coatings can also be achieved in an UHV but only at −130 °C[17]. The reason for this was not elucidated.

To extend the application of MoS_2 in air, a coating composed of MoS_2 nanoparticles was scrutinized. The MoS_2 nanoparticle film was fabricated by localized high-pressure arc discharge and exhibited a pronounced (0002) peak in the X-ray diffraction spectrum, whereas a film produced by sputtering MoS_2 does not. This indicates that the MoS_2 nanoparticle film primarily stacks in layers. The MoS_2 nanoparticle film exhibited an excellent low friction (CoF = 0.008) while sliding against uncoated steel in air with 45% relative humidity. In contrast, the sputtered MoS_2 film presented a CoF above 0.1 that increased sharply

afterwards. A similar tendency was observed upon sliding the sputtered MoS_2 film in nitrogen, where the initial CoF was 0.03. The MoS_2 nanoparticle film also showed a lower wear rate than the sputtered MoS_2 film. The transferred MoS_2 nanoparticle film fully covered a steel ball, whereas the transferred sputtered MoS_2 film only partially covered the steel ball. This extraordinary lubricating feature of the MoS_2 nanoparticle film was linked with the presence of a highly ordered MoS_2 plane after friction, whose wear debris exhibited curved hexagonal planes.

1.3. Superlubricity in liquids

1.3.1. Water

In terms of the visco-pressure coefficient and viscosity, water is not considered to be a good lubricant because of its poor ability to form a thick liquid film that separates contact between asperities. However, water was proven to be extremely efficient for lubricating ceramics at high sliding speeds[51,52,53]. For instance, sliding of Si_3N_4/Si_3N_4 in water at 120 mm/s, over approximately 1100 m established a superlubric state[26]. This running-in process involved a sharp drop in the mean contact pressure to 6 MPa. The normal force was 5 N, and the diameter of contact area was 1062 μm. The Hertz contact area of the equivalent radius (R1) and the contact area radius (B) follows the equation[54]:

$$B = (3WR1/2E')^{1/3}$$

where W is the normal force and E' is the reduced elastic modulus.

Therefore, R1 was calculated to be 6.1 m. Since the visco-pressure coefficient of water is zero, the water film present between the contact surfaces was isoviscous. As the authors stated, the water film thickness at 120 mm/s was 80 nm. The thickness did not exceed three times the composite roughness. Thus, the normal force was not only supported by the liquid film, but also by the boundary silica film lubrication layer formed on both surfaces. The tribochemical reactions that occurred between Si_3N_4 and water were given as follows:

$$Si_3N_4+6H_2O=3SiO_2+4NH_3$$

$$SiO_2+2H_2O=Si(OH)_4$$

This assumption was supported by the fact that ammonia was detected upon grinding Si_3N_4 powder in water [55]. The formation of SiO_x was suggested using electron energy loss spectra to analyze wear particles containing not only Si and O but also C and N [56]. Furthermore, SiO_2 was dissolved in water by reacting to from silicic acid [57].

Similarly, self-mated SiC also exhibited low friction in water at 120 mm/s[58]. Regardless of the initial roughness of SiC, the final CoF was stable at approximately 0.01. The authors suggested that the following reaction took place during sliding:

$SiC+2H_2O=SiO_2+CH_4$

Regarding the final CoF difference between SiC and Si_3N_4, the authors explained that it originated from the energy gap difference between ceramics and water. The difference between Si_3N_4 and water is 3 eV, whereas the difference between SiC and water is 5.2 eV. A lower energy gap difference indicates a higher reaction rate. Colloidal silica was more difficult to generate by triboreaction for SiC compared with Si_3N_4. Moreover, a longer running-in period was observed for SiC compared with self-mated Si_3N_4. The most recent first-principles molecular dynamic simulation showed that the tribochemical reaction occurred more easily for self-mated Si_3N_4 than for SiC because the triboreaction barrier of Si_3N_4 is lower than that of SiC and highly coordinated Si atom intermediates of Si_3N_4 also promoted the reaction[59].

Additionally, sliding a Si_3N_4 ball against Al_2O_3 in water at 1 m/s also led to superlubricity where CoF was determined to be 0.004[60]. When sliding occurred between self-mated oxide-based ceramics such as Al_2O_3 and ZrO_2 (PSZ-1), from 0.1 to 0.8 m/s, the CoF was always above 0.2[52]. The surface of ZrO_2 after friction was covered with scratches, whereas the surfaces of SiC, Si_3N_4, and Al_2O_3 were exceptionally smooth. The cause of this difference remains unknown.

These studies have shown that liquid water lubricates ceramics well at a high sliding speed. The lowest sliding speed reported to reach superlubricity was 60 mm/s for self-mated Si_3N_4[51]. Below this speed, the CoF began to increase as the sliding speed decreased. At 10 mm/s, the final CoF was approximately 0.7 for Si_3N_4 and 0.25 for SiC. When water lubricated in the gas phase, although it changed the humidity of air or was directly added to the N_2 atmosphere, a CoF above 0.5 was observed for Si_3N_4 and above 0.2 for SiC[52]. All of these results highlight the importance of a thick water film to achieve superlubricity.

1.3.2. Polyalkylene glycol (PAG)

PAG is a copolymer consisting of ethylene and propylene oxides. When pure PAG was used to lubricate steel surfaces at a sliding speed of 0.2 m/s, the final CoF was approximately 0.1. A slight decrease in the CoF was observed upon increasing the viscosity of PAG from 15 MPa·s to over 100 MPa·s. However, the final CoF was always above 0.03[61]. The CoF was further reduced by sliding the steel tribopair in an aqueous polyethylene glycol (PEG) solution to form O–H bonds on the steel surfaces. The tribopair was subsequently slid in PAG. Although sliding steel tribopairs in PEG increased the surface roughness from 10 to 40 nm, the generation of a large wear scar (490 μm) significantly increased the equivalent radius of the steel ball, increasing the PAG film thickness and completely preventing asperities from coming into contact with one another. Hence, superlubricity was achieved.

For a Si_3N_4 ball sliding against an Al_2O_3 disk, researchers added water to the PAG to achieve superlubricity[62]. At a sliding speed of 24 mm/s, an aqueous PAG solution was used as a droplet state or reservoir and once the PAG concentration was in the 30 to 60 wt% range, superlubricity was achieved (Fig. 1b). This superlubricity was associated with the presence of free water in the aqueous PAG solution because, although the solution functions as an EHL with a theoretical liquid CoF below 0.01, upon lubricating the pure PAG solution, the CoF was approximately 0.1. PAG chains were absorbed on the surface of the ceramic to support the load and water offered a low-energy dissipation pathway.

The impact of the degree of polymerization of PAG on the friction was later studied by sliding a Si_3N_4 ball against a SiO_2 disk[38]. The authors termed the highest concentration of aqueous PAG solution where superlubricity emerged as the threshold concentration. In brief, when the molecular weight (MW) was below 2000, the threshold concentration decreased as the MW of PAG increased. Above a MW of 2000, no clear impact on the threshold concentration was observed when the MW of PAG was changed (Fig. 1a). Moreover, the CoF was augmented as the MW increased at the threshold concentration. A model was proposed to explain this (Fig. 1c–d). Below the threshold concentration, the free water and PAG chains formed an easy-shear layer that minimized the friction. When the concentration reached a threshold value, free water was not present between the contacts, however, bound water prevented direct entanglement of PAG chains with the absorption layers. Finally, as the PAG concentration was further increased, interfacial PAG chains were created. These impeded the shearing of surfaces. Therefore, superlubricity vanished at high concentrations.

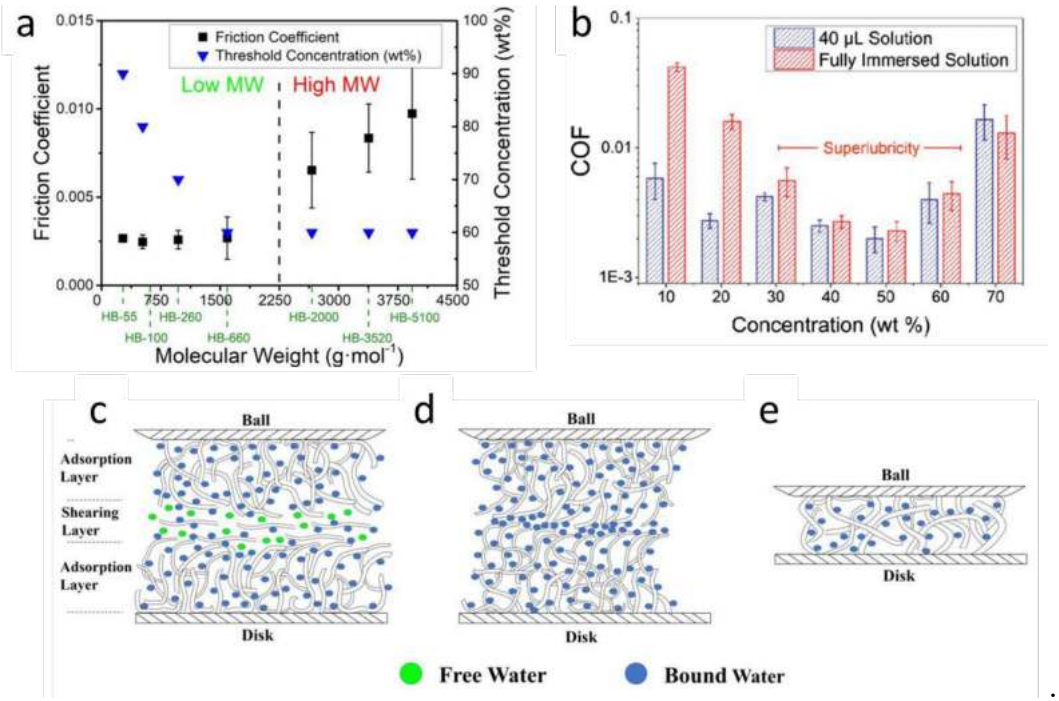

Fig. 1 a For tribopair of Si_3N_4/SiO_2, threshold concentration and corresponding CoF of PAG aqueous solutions with different MWs[63]. **b** For tribopair of Si_3N_4/Al_2O_3, Final friction coefficient of 40 μL and fully immersed PAG aqueous solutions (HB-260)[62] (Reproduced from Ref. 62 with permission from WILEY-VCH Verlag GmbH & Co. KGaA, Weinheim) Schematic illustration of the proposed lubrication model between two sliding solid surfaces. Model for PAG aqueous solutions **c** below the threshold concentration; **d** at the threshold concentration; **e** beyond the threshold concentration[63] (Reproduced from Ref. 61 with permission from American Chemical Society).

1.3.3. Phosphoric acid

An aqueous phosphoric acid solution is an excellent lubricant. By sliding a Si_3N_4 ball against glass in a 30 μL aqueous phosphoric acid solution for 10 min, the CoF dropped to 0.004 with no further increase (Fig. 2a). It is noteworthy that in the immersion state, the CoF remained at approximately 0.04. A friction test generated a transparent gel-like film on both the ball and disk (Fig 2b and c). This film was primarily composed of phosphoric acid. With no direct contact between surfaces, a transparent gel-like film was formed on the tribopair along with the evaporation of water. This film lubricated surfaces with no liquid solution present. A 3 N normal load was applied on the film-coated tribopair and the CoF stabilized at 0.02. The CoF further reduced to 0.004 when 5 mL water was added to the contact (Fig. 2d). The authors attributed the enhanced friction to the low shear strength of water, present between H networks in H_3PO_4 and water (Fig. 2e). The composition of this transparent film formed by

shearing was confirmed by in situ Raman analysis (Fig. 2f). The evolution of the CoF with time was divided into 3 stages and the major change of species between the contacts occurred in stage 2 (Fig. 2a), where the symmetric stretching of the P–OH bond shifted from 891 to 910 cm^{-1}. Simultaneously, peaks indicating hydrogen bonding in water at 3240 and 3415 cm^{-1} disappeared with a new peak observed at 3510 cm^{-1}. All of these changes confirmed the formation of a hydrogen-bonded network consisting of water, H_3PO_4, and $H_2PO_4^-$.

The excellent tribological properties of the phosphoric acid solution are not limited to tribopairs. Sliding ruby against sapphire in a phosphoric acid solution also generated superlubricity when the sliding speed was above 4.7 mm/s[64]. Similarly, a phosphoric acid solution was used in the droplet state instead of the immersion state. This suggested that the lubricity of the phosphoric acid solution was governed by the air humidity. Superlubricity was only achieved when the humidity was below 90%. The authors concluded that the failure of the phosphoric acid solution at high humidity resulted in the destruction of the hydrogen bond network. Because the sliding speed influenced the final CoF, the thickness of the hydrogen bond network was important for reducing the friction. Therefore, the contact between surfaces was divided into three regimes: H-bond contact, stern layer contact formed by hydrogen ions, and direct contact. The idea was to minimize direct contact and to allow water and H-bond networks to lubricate surfaces.

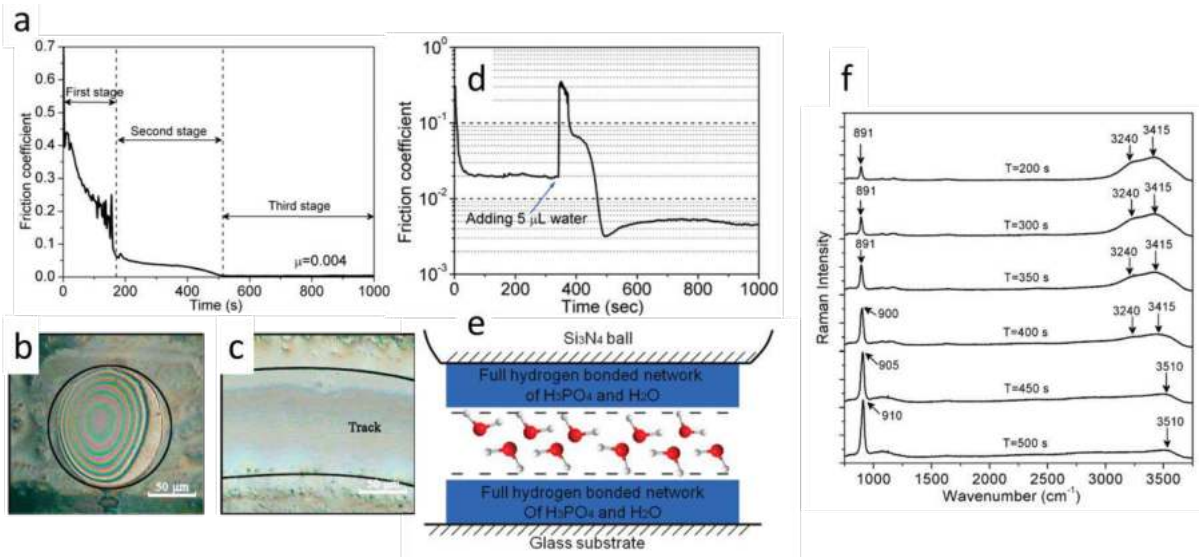

Fig. 2 Sliding Si_3N_4 ball against the glass in 30 μL phosphoric acid aqueous solution (pH=1.5) **a** Friction coefficient with time[27] **b** Optical image of the top region of the ball[65]. **c** Optical image of the track on the glass substrate[65] **d** CoF with time after a load of 3N was applied to glass substrate who is covered by phosphoric acid film. After about 300s passes, a droplet of deionized water (about 5 μL) is

added to the track[65] **e** Schematic illustration of the likely structure between the two friction surfaces[65]. The red atom represents oxygen, and the white atom represents hydrogen (Reproduced from Ref. 65 with permission from American Chemical Society) **f** Raman spectrum of the solution confined between two friction surfaces in the second stage[27]. (Reproduced from Ref. 27 with permission from AIP Publishing LLC)

Although the tribopairs Si_3N_4/SiO_2 and Al_2O_3/Al_2O_3 exhibited similar variations in the CoF and sliding speed when the sliding speed was below 0.26 m/s, when the sliding speed was above this value, only the Al_2O_3/Al_2O_3 tribopair displayed superlubricity[66]. For the Si_3N_4/SiO_2 pair, as the sliding speed increased, the roughness of the Si_3N_4 ball increased from 15 to 370 nm. Such an increase in the surface roughness makes it impossible for the liquid film to separate contact between asperities. For instance, the calculated liquid film thickness at 0.334 m/s was approximately 20 nm, while the roughness of the Si_3N_4 ball after friction increased to approximately 270 nm. The authors attributed the failure of superlubricity to the lack of a hydrated water layer on the contact surfaces.

To investigate the role of H ions on the surfaces, Si_3N_4 balls were slid against SiO_2 disks in phosphoric acid solutions with varying pH. Superlubricity was only obtained when the pH was between 0.75 and 1.75. When the pH was outside this range, the CoF increased to values above 0.01. As the pH increased, the wear diameter increased. This is because water preferentially reacted with ceramics rather than phosphoric acid. Therefore, when the pH was below 0.5, an insufficient amount of water was present to create a large wear scar before its evaporation, resulting in a high contact pressure. The load capacities of the formed stern layer and H-bond network were limited. A high pressure led to a more direct contact between asperities. Thus, the CoF increased. However, when the pH was above 2.25, the surfaces do not capture a sufficient amount of hydrogen ions to form a stern layer that covers the majority of surfaces owing to the scarcity of H_3PO_4. A higher amount of direct contacts was also observed in this case[67].

As discussed previously, the presence of positive ions such as H^+ is necessary to realize superlubricity. As such, it would be interesting to study whether the positive ions in salt reduce the barriers to reach superlubricity. In contrast to Si_3N_4/SiO_2 and Al_2O_3/Al_2O_3 in phosphoric acid, at 0.094 m/s, the CoF of Si_3N_4/Al_2O_3 stabilized at 0.022. However, if Si_3N_4/Al_2O_3 was initially slid in phosphoric acid, and the acid was subsequently removed and a KCl solution added to the contact, a CoF of 0.005 was achieved. It is worth mentioning that

the KCl solution alone cannot achieve superlubricity under these experimental conditions[68]. Sliding in KCl and H_3PO_4 solutions increased the SiO_2 content on the silicon nitride surface. The highest content was attained when running-in was first performed in the H_3PO_4 solution, followed by sliding in the KCl solution. Since the SiO_2 layer provided more active sites to react with water and to form hydroxyl groups on the silica layer, the SiO_2 layer was negatively charged and attracted positive ions such as potassium. A hydration shell surrounded the potassium ions and provided a repulsive force to support a large charge. Water present between hydration shells acted as an easy-shear layer. Therefore, superlubricity was established. It is worth noting that HCl and H_2SO_4 can replace phosphoric acid in the running-in process without increasing the final CoF.

In addition to the KCl solution, friction reduction can also be realized using a divalent or trivalent chloride solution. It is worth mentioning that the change in lubricant induces variations in the critical velocity required to reach superlubricity. Briefly, the critical velocity required for superlubricity follows this sequence: monovalent, divalent, and trivalent chloride, from fastest to slowest. For instance, the critical velocity for a KCl solution was determined to be 47 mm/s, whereas the value for $MgCl_2$ was approximately 30 mm/s[24]. For $AlCl_3$ and other trivalent chloride solutions, superlubricity was achieved even at 3 mm/s. The concentration of the chloride solution was fixed at 1 mol/L. Achieving superlubricity and running-in with a H_3PO_4 solution is indispensable. The reason why multivalent ions are preferred to achieve superlubricity is as follows. Negatively charged ceramic surfaces attract positive ions through Coulombic forces. However, the affinity between ions and negatively charged surfaces is directly linked to the ion charge. In particular, for a trivalent chloride solution, an increase in its concentration results in a change of the zeta potential from negative to positive (unique to trivalent ions). This indicates that the charge of the ceramic surface changes at high concentrations, corresponding to excessive adsorption of trivalent ions. The adsorption of hydrate trivalent ions on surfaces supports a high load and provides an easy-shear interface. Another advantage of using trivalent Al^{3+} is that it provides H^+ ions since Al^{3+} reacts with water to produce $Al(OH)_3$ and H^+.

In all the aforementioned studies, superlubricity was achieved when a H_3PO_4 solution was either directly used as a lubricant or as a surface modifier during the running-in process. If H_3PO_4 only provides H^+ ions, then other acids should also be capable of achieving superlubricity. Hence, the tribopair of Si_3N_4 and SiO_2 were lubricated by H_2SO_4 solutions with different pH[69]. The lowest CoF of approximately 0.03 was obtained when the pH was

1.5. This phenomenon was most likely triggered by the competing effect between the H^+ concentration and the contact pressure. When the pH increased, the H^+ concentration decreased, however, the contact pressure increased owing to the increased wear width. Regardless of how these properties change, the final CoF does not result in superlubricity. Furthermore, as the time increased, the low friction state collapsed within 20 min. The same tendency was also observed for a $H_2C_2O_4$ solution. Only a H_3PO_4 solution can guarantee an extended and stable superlubricity state.

Even with Si_3N_4/SiO_2, a H_2SO_4 solution cannot sustain extended and stable superlubricity. However, H_2SO_4 was used in the running-in period to lower the contact pressure and to functionalize the surfaces of ceramic at a suitable pH[70]. Superlubricity was only achieved in the pH range of 0.5 to 2.0. When the pH was 0, the wear diameter was approximately 180 mm, generating a contact pressure of 118 MPa. This contact pressure doubled at a pH of 1.5. When the pH was 2.5, the contact pressure was below that determined at a pH of 1.5. However, this low contact pressure created a rough surface with grooves. Without running-in in a H_2SO_4 solution, the CoF stabilized at 0.13 with visible scratches present on the ball and black substances accumulated on the disk. In addition to dropping the contact pressure, the following chemical reactions between H_2SO_4 solutions and ceramics took place:

$$Si_3N_4+6H_2O=3SiO_2+4NH_3$$

$$SiO_2+2H_2O=Si(OH)_4$$

Similar to sliding ceramics in pure water, the generation of silica favors friction reduction.

1.3.4. Saturated and unsaturated fatty acids

Unlike boric acid and sulfuric acid, which are primarily added to water to ameliorate its tribological performance, saturated and unsaturated fatty acids can either be used as friction modifiers[71] in mineral oil or directly used as lubricants [72,73]. However, when saturated and unsaturated fatty acids lubricated a steel/steel pair, no superlubricity was reported. The situation changes when ta-C is considered. At 0.05 m/s, self-mated ta-C underwent a short running-in and stabilized in the superlubricity regime[74]. Additional attention should be paid to aC:H because it is essentially composed of amorphous carbon doped with hydrogen. However, its tribological performance in oleic acid differs greatly from that of ta-C. The CoF of self-mated aC:H stabilized at a value 10 times higher than that of ta-C. Using ToF-SIMS

analysis, the authors demonstrated that oleic acid chains occupied the aC:H surface while the ta-C surface was covered with OH functional groups. Therefore, the shearing plane of aC:H was the H head in the methyl group of $C_{17}H_{33}COO^{-}$, however, the shearing plane of ta-C was between the OH functional groups. This discrepancy between the surface terminations resulted in distinctive friction behaviors when asperities were in contact.

Using simulation, Takuya explained why the intact oleic acid chain did not appear on the worn ta-C surface but small molecules such as OH did[75]. To simplify the simulation process, the author compared the tribological performance of five molecules: heptane, heptanoic acid, heptene, trans-3-heptenoic acid, and cis-3-heptenoic acid. The major differences between these molecules is the presence of COOH and C=C functional groups on the aliphatic chain, and the location of the functional groups. All molecules on ta-C can exist in 3 different states: non-bonding, anchoring, and cross-linking. With sufficient pressure, all tested molecules crosslinked on ta-C. However, the critical pressure required to achieve crosslinking varied with the type and number of functional groups on the molecular chain. The critical pressure followed this sequence: no functional group > one functional group > two functional groups (from highest to lowest) since COOH or C=C acted as reactive sites to bond with ta-C surfaces. Since molecules containing both COOH and C=C groups were inclined to crosslink on ta-C surfaces when shearing occurred, molecules such as cis-3-hepenoic acid and oleic acid underwent fragmentation and formed H, OH, and C=C terminations on ta-C surfaces, directly protecting ta-C surfaces from cold welding and providing low friction.

In addition to forming surfaces rich in OH groups, the structural change of the topmost surface of ta-C in oleic acid was also highlighted[76]. It is difficult to calibrate for ta-C samples during XPS measurements owing to the lack of a reference peak. If the C_{1s} peak is used as a reference, the ratio between sp^2 and sp^3 is hidden. Therefore, high-resolution synchrotron radiation photoemission was used to identify the ratio change in sp^2 and sp^3. The original ta-C employed in this experiment was predominantly sp^3 hybridized. By comparing with graphite and graphene, a new peak appeared on the ta-C worn scar after friction, close to the sp^2 orbital of graphite and graphene. Soft X-ray absorption near edge structure measurements further confirmed that the characteristic 1s-pi* transition sp^2 absorption peak appeared after friction. All the analyses indicated that after friction, the topmost layer of ta-C was highly sp^2 hybridized. It was most likely composed of a local graphenic structure. Considering that C–OH and C=O groups were also detected, this graphenic structure was partially oxidized.

Simulation results further confirmed that the friction behavior of ta-C was highly associated with the sp^2 content. A low sp^2 hybridized ta-C represented a sp^2/sp^3 ratio of 54%, while a high sp^2 hybridized ta-C represented a sp^2/sp^3 ratio of 73%. Under the same simulation conditions, the CoF of high sp^2 hybridized ta-C was only one sixth that of the low sp^2 hybridized ta-C. Such a drastic decrease in the CoF was associated with the disappearance of the interfacial C–C bond.

In summary, oleic acid molecules tend to crosslink on the ta-C surface. Under shearing, this molecule decomposed into OH, H, and C=C fragments that occupied the ta-C surface. Simultaneously, the ta-C topmost surface underwent a transition from sp^3 to sp^2 hybridized and generated a structure similar to graphene oxide. This structure passivated the ta-C surfaces and produced low friction.

1.3.5. Polyols

Glycerol produced an anomalously low friction (CoF = 0.02) in self-mated steel under 1 mm/s and at a maximum Hertzian contact pressure of 800 MPa[77]. Such severe lubricating conditions resulted in the realization of boundary lubrication; however, this low friction state was not sustainable in the long term. Over time, the steel surface became rough with a clear wear scar generated on the steel surface. This corresponded to a drastic decrease in the electrical contact resistance. This indicates that fewer asperities were in contact when the friction was low and that an insulated solid or liquid film was present between the steel surfaces, partially separating direct contact between asperities. In this case, the lubricating film was most likely a liquid film because chemically absorbed species on the steel surface were easily removed by Ar etching for 1 min, indicating that these species were present on the surface as a 1 nm thick steel surface. However, in general, under boundary lubrication, the influence of the liquid is negligible since the contacts between asperities are more pronounced in this regime. Therefore, the authors proposed the term ‘thin EHL film’ to highlight the importance of the liquid film in this experiment. This thin liquid film consisted of glycerol and glycerol degradation fragments, which included water. Furthermore, the worn steel surface in the low friction regime was terminated by H, OH, and other carbonaceous species. The authors attributed these carbon species to contamination from the environment since glycerol degradation products contain not only C and H, but also O. Thus, the key to low friction lies in the formation of FeOOH on the steel surface and the presence of a thin liquid EHL film.

For self-mated steel, superlubricity was achieved using an aqueous glycerol solution (30 wt%) and by adjusting the sliding speed to below 150 mm/s[25]. The preferred humidity range to realize superlubricity was from 40% to 50%. Outside this range, the friction increased and exceeded 0.01. The authors claimed that humidity regulation benefitted the absorption of FeOOH functional groups by water and glycerol molecules through hydrogen bonding. This hydrated layer consisted of water and glycerol that bore the load and easily sheared.

Superlubricity was also realized using pure glycerol to lubricate self-mated ta-C at a sliding speed of 300 mm/s[78]. A similar result was obtained by Takuya et al. below 100 mm/s[75]. Superlubricity was accomplished using ta-C/ta-C but not when steel/steel or aC:H/aC:H were used. By employing marked glycerol, ToF-SIMS analysis indicated that the parent glycerol molecule ($^{13}C_3H_7O_3^-$) and its fragments ($^{13}CH_2$, ^{13}CHO, $^{13}CH_2O$, $^{13}C_2H_3O_2$) were prevalent in the wear track and not outside it, indicating that glycerol decomposed upon shearing ta-C surfaces. Using deuterated glycerol, ^2H and O^2H terminations were more pronounced in the wear track. In summary, glycerol decomposed under shearing and terminated the ta-C surface with H, OH, and glycerol fragments.

The mechanism for superlubricity is widely debated. Two possible mechanisms are proposed:

- Under shearing (Fig. 3a), glycerol rapidly functionalizes the ta-C surface with H and OH terminations. These terminations strongly interact with glycerol through hydrogen bonds. Therefore, a monolayer of glycerol is bonded to the ta-C top surfaces. Sliding of ta-C surfaces results in the sliding of the glycerol molecule film. Such a structure is easy to shear and presents a CoF of approximately 0.03 under 0.6 GPa.
- When only one glycerol is added to make contact and the normal pressure is fixed at 5 GPa (Fig. 3b), the glycerol molecule crosslinks on ta-C surfaces and decomposes under shearing. During this process, H, OH, and ether groups are released to passivate ta-C surfaces. Only one glycerol molecule was considered. These passivation species are not sufficient to fully prevent the formation of interfacial C–C; therefore, the shear stress increases. Carbon rehybridization occurs during shearing, leading to aromatization of the top surface. This prevents cold welds between ta-C surfaces. Thus, the CoF drops to 0.02. The authors attribute this CoF to collisions between dome-shaped aromatic species, not superlubricity. The authors believe that during the experimental time scale, the dome-shaped aromatic species transform into flat aromatic species.

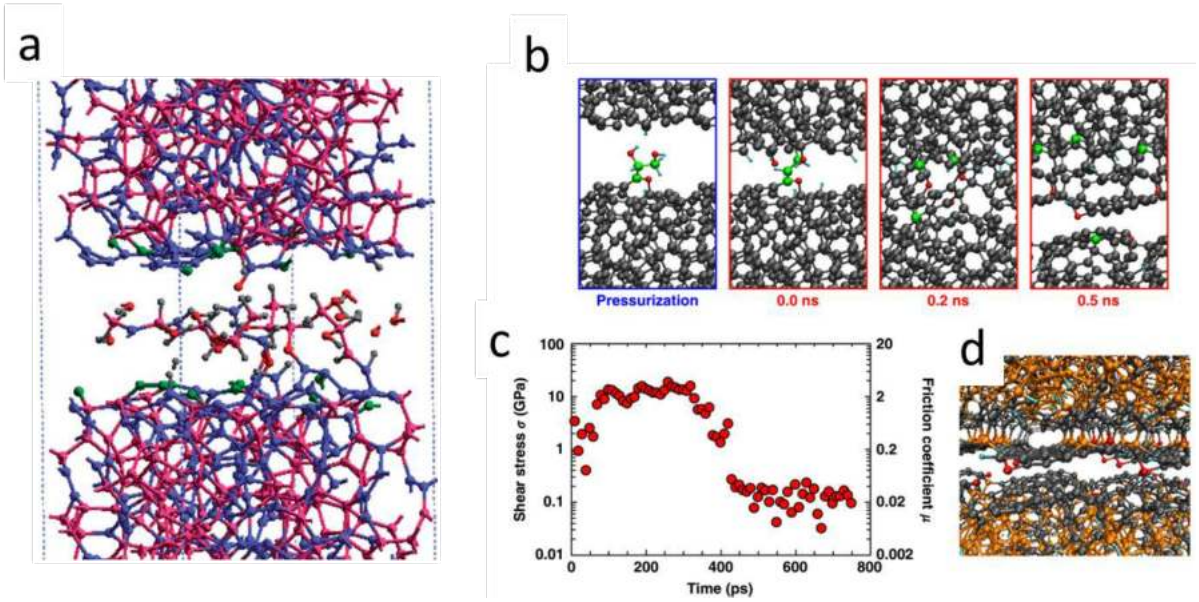

Fig. 3 a Structure of the glycerol lubricated ta-C after sliding for 20 ps at v = 100 m/s. sp3 C: pink; sp2 C: blue; sp1 C: green. O: red; H: gray. Indicate how many surface structures there are. This surface leads to μ = 0.03 at 0.6 GPa[78] (Reproduced from Ref. 78 with permission from Elsevier B.V.). A QMD simulation of two ta C surfaces lubricated with a glycerol molecule. **b** Snapshots of the 1-ns sliding simulation. **c** Evolution of the shear stress σ and friction coefficient μ. **d** Shear-induced aromatic passivation of both ta-C surfaces. 3- and 4-fold coordinated C atoms are represented in grey and orange spheres, respectively[75] (Reproduced from Ref. 75 with permission from Springer Nature).

It is worth mentioning here that when glycerol vapor was used to lubricate self-mated ta-C, a stable CoF of 0.05 was observed[79].

Glycerol also afforded excellent lubricity to Si_3N_4/SiO_2, however, superlubricity was not directly achieved at a maximum Hertzian pressure of 700 MPa and a sliding speed of 0.075 m/s[80]. Therefore, to minimize friction, a sulfuric acid solution was added to the glycerol solution. The CoF stabilized at 0.03 if the sulfuric acid solution and glycerol solutions were used separately. However, if they were used together, the CoF further decreased to 0.004. The authors explained the strong synergy between glycerol and sulfuric acid, where sulfuric acid provided hydrogen atoms to positively charge the ceramic surface by generating $SiOH_2^+$-terminated surfaces. These $SiOH_2^+$-terminated surfaces further bonded with the glycerol-water network through hydrogen bonding. The shear plane was a water layer adsorbed on the glycerol-water network. Superlubricity was realized as a result of the easy-shear properties of the water layer. Glycerol can be replaced by other polyhydroxy alcohols as long as they possess two OH groups, for example, 1,4-butanediol and 1,5-pentanediol[81].

1.3.6. Glyceride of fatty acid

Glycerol and oleic acid demonstrated excellent lubricity. Glyceryl monooleate (GMO) is a combination of these two molecules. GMO can be dissolved in commercial lubricant oils such as PAO. This opens up the possibility of direct application in industry. For the ta-C/steel tribopair, when only 1% of GMO was added to PAO, the CoF decreased from 0.06 to 0.02[78]. Moreover, Makowski et al. reported that a steel/ta-C pair reacted in GMO (40% purity) as a function of the temperature [82]. The authors demonstrated that a high temperature of approximately 80 °C was beneficial for friction reduction. However, in order to minimize wear, a low temperature of approximately 40 °C was preferred. Unfortunately, this abnormal friction behavior as a function of the temperature was not explained in the article.

Apart from GMO, castor oil is primarily composed of triglycerides of ricinoleic acid, and has also been highlighted recently, not only because it is a cheap, eco-friendly vegetable oil, but also because it exhibits excellent lubricating ability. Quinchia et al. attributed the outstanding lubricating ability of castor oil to its high viscosity. As a result, it is more likely to form a liquid film that separates solid contacts compared with other low viscosity vegetable oils, such as soybean and sunflower oils[83]. In addition to emphasizing the excellent ability of castor oil to form a liquid film, Zeng et al. focused on its boundary lubricating properties where contact between asperities dominate the friction behavior[4]. For nitinol 60 alloys sliding against steel, superlubricity was demonstrated even at a sliding speed of 3 mm/s and a lambda of approximately 0.2. The key to this superlubricity lies in the formation of metal hydroxide and hexanoic acid on each surface through a tribochemical reaction between the metal and castor oil. These species provided a repulsive electrostatic force to support the load, allowing sliding to readily occur between asperities.

To facilitate the understanding of all those articles mentioned before, a table with experimental details is demonstrated here:

Table 2: Experimental condition of superlubricity acchieved.

P_{max} is maximum hertzian contact pressure. T is temperature. v is sliding speed.P is apparent pressure. RH is relative humidity. LV is lubricant volume.

Tribo-pair	lubricant	LV	T-°C	P_{max} -MPa	p-MPa	v-mm/s	RH -%	λ	CoF
SiC /SiC	water[58]	-	-	Fn=5N	~4	120	-	-	0.01
Si_3N_4 /Si_3N_4	water[58]	-		Fn=5N	~7	120	-	-	0.004

Si_3N_4 /Al_2O_3	water[60]	-	23	P_{mean}=900 MPa	10	1000	-	-	0.002
Si_3N_4 /Si_3N_4	water[53]	-		Fn=5N		60	-	-	superlubricity
Steel /steel	PEG aqueous solution before PAG100 or PAO6[61]	50 μL	24-27°C	426	~15	200	10-20	>3	~0.005
PEG aqueous solution used here contains 33%wt PEG.									
Si_3N_4 /Al_2O_3	PAG aqueous solutions (50wt%)[62]	Full immersion	25	1680	60	24	-	2.5	~0.003
Superlubricity can only be achieved with 30 wt% - 60 wt% PAG aqueous solutions. Molecular weight of PAG is around 970 $g \cdot mol^{-1}$									
Si_3N_4 /Al_2O_3	PAG aqueous solutions (70 wt%)[63]	Full immersion	25	1680	-	24	20-40	-	~0.003
Superlubricity is achieved with 70 wt% PAG aqueous solutions. Molecular weight of PAG is around 970 $g \cdot mol^{-1}$									
Si_3N_4 /SiO_2	H_3PO_4 PH 1.5[64]	5 μL or 30 μL but not full immersion	25	700	31	56	25	-	0.004
It should highlight that in full immersion, steady CoF is 0.03									
Ai_2O_3 /SiO_2	H_3PO_4 PH 1.5[65]	10 μL	25	Fn=3N	96	4.7	30	-	superlubricity
Si_3N_4 /SiO_2	H_3PO_4 PH 1[66]	10 μL	25	700	110	56	25	-	0.006
Si_3N_4 /SiO_2	H_3PO_4 PH 1.5[67]	10 μL	25	830	56	75	60	-	0.008
Si_3N_4 /SiO_2	H_3PO_4 PH 1.5+KCl solution(50 mmol/L) [68]	H_3PO_4 100 μL +KCl solution 200 μL	25	700	250	94	20-40	-	0.005
Si_3N_4 /SiO_2	H_3PO_4 PH 1.5+salt solution($AlCl_3$,$CeCl_3$,$CrCl_3$) [24]	salt solution 200 μL	25	700	250	3.1	10-50	-	0.002
Running in with H_3PO_4, then lubricated with salt solution with 1mol/L concentration.									
Si_3N_4 /SiO_2	H_3PO_4 PH 1.5[69]	30 μL	25	700	-	56	25-35	-	0.004
Si_3N_4 /SiO_2	H_2SO_4 PH 1.5+silicone oil(100) [70]	20 μL	25	700	56	13	25-40	-	superlubricity
Running in with H_2SO_4 solution, PH should in between 0.5-2. Following by silicone oil whose viscosty is 300 mPa·s, the minimum sliding speed to superlubricity is 6 mm/s									
ta-c /ta-c	Oleic acid[75]	-	80	234	~120	157	-	0.89	0.008
ta-c /ta-c	Oleic acid[78]	10 μL	Ambient temperature	70	-	50	45	2	0.01
Steel /steel	30 wt% glycerol aqueous solution[25]	30 μL	20	667.5	40	150	50	1.81	0.005
Here, humidity at 40%, superlubricity also can be achieved.									
ta-C	glycerol[75]	-	80	234	~13	157	-	1.3	0.008

/ta-C					0				
ta-C	glycerol[78]	5000 μL	80	270	-	300	-	-	superlubricity
/ta-C									
Si_3N_4 /SiO_2	Glycerol+acid +water[80]	20 μL	25	700	-	75	45-55	-	superlubricity
Here, glycerol aqueous solution concentration should be less than 45%. Acid PH should be less than 1.									
Si_3N_4 /SiO_2	Polyhydroxy alcohol+acid +water[81]	20 μL	25	700	-	75	20-40	-	superlubricity
Ni alloy /steel	Castor oil[4]	No reservoir	Ambient temperature	280	~46	3	40	0.2	0.0005

1.4. Additives

In this section, the change in tribological performance is highlighted when silica or graphitic materials are added to a lubricant since a SiC disk embedded with graphitic material and a hydrate silica layer is an efficient friction reduction layer for Si-based ceramics.

1.4.1. Silica

In 1999, $Si(OC_2H_5)_4$ was proposed to enhance the formation of a silica layer by adding it to water[26]. The reaction with water was given as follows:

$$Si(OC_2H_5)_4 + H_2O \xrightarrow{NH_4OH} SiO_2(colloid)$$

Here, NH_4OH is a product of the tribochemical reaction between Si_3N_4 and water. With 0.1% of this additive incorporated, the running-in period was reduced by half. The change in wear was not mentioned in the article. Moreover, with unique treatment, aerogel silica[84] and alumina-silica were prepared from a mixture of $Al(C_3H_7O)_3$ and $Si(OC_2H_5)_4$. This aerogel was dispersed in oil with the assistance of copper stearate. The presence of the aerogel reduced the CoF and wear and optimized the maximum non-seize load.

Additionally, using the Stober method, silica nanoparticles were prepared and dissolved in deionized water[85]. Compared with using pure water to lubricate self-mated Si_3N_4, 0.5 wt% silica nanoparticles in water significantly reduced the friction and wear. In this case, the influence of wear protection should be emphasized because sliding self-mated Si_3N_4 in water at a high sliding speed led to a drop in the CoF into the superlubricity regime[53]. However, this

process was always accompanied by the generation of an extremely large wear scar. The wear was limited when silica nanoparticles were added. For instance, the wear scar radius was 1780 mm in pure water. When 0.5 wt% silica nanoparticles were added, the wear radius shrank to 1441 μm[86]. This wear protection was further enhanced by grafting organic chains containing NH_2, COOH, and CH_3 groups onto the surface of the silica nanoparticles (Fig. 1a). The organic chains containing NH_2 groups were superior to other functional groups since they generated the smallest wear scar and required the shortest running-in time. Moreover, by optimizing the concentration of silica nanoparticles, the diameter of the wear scar further decreased to 0.61 mm. To lubricate self-mated Si_3N_4, replacing amino-functionalized silica nanoparticles with amino-functionalized TiO_2 and ZnO nanoparticles caused a rise in the CoF[87]. When the nanoparticle concentration was above 1 wt% the wear diameter increased. This phenomenon was associated with the fact that, unlike silica, TiO_2 and ZnO nanoparticles were not capable of forming a homogeneous protective film on Si_3N_4.

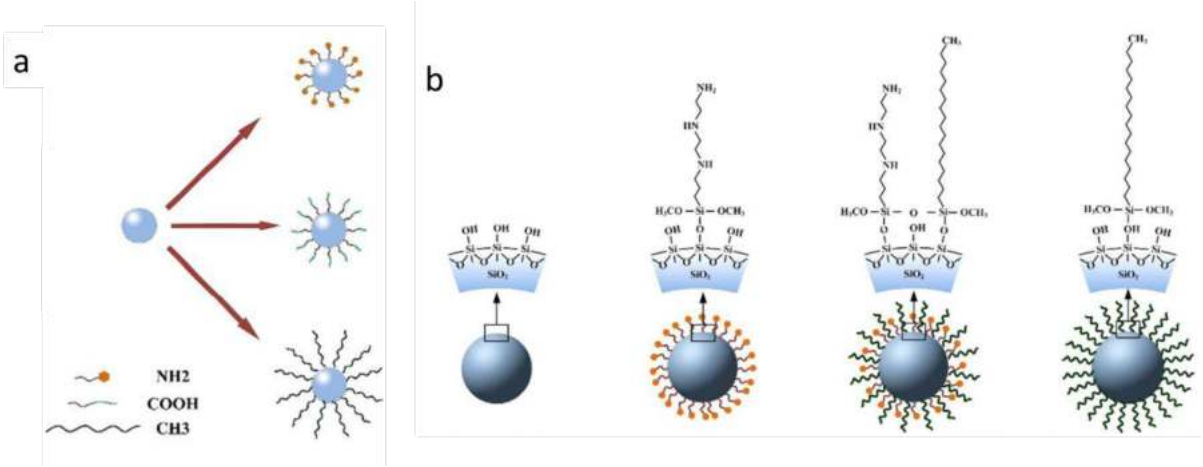

Fig. 1 a Schematic diagram of silica nanoparticle after surface modification. 3-amino-propyl triethoxysilane, N-octyl trimethoxysilane and succinic acid are sources of NH_2, COOH, CH_3 organic chain in this diagram, respectively[86]. (Reproduced from Ref. 86 with permission from Elsevier Ltd and Techna Group S.r.l.) **b** Schematic diagram of unmodified silica nanoparticles and silica nanoparticles modified with N1-(3-Trimethoxysilylpropyl) diethylenetriamine and octadecyltri methoxysilane[88]. (Reproduced from Ref. 88 with permission from Springer Nature)

Even though silica nanoparticles efficiently reduced the friction and wear, their performance was highly affected by the experimental conditions. For example, in comparison with pure water, at sliding speeds of 0.5 mm/s or 0.25 mm/s, introducing silica nanoparticles to the water significantly reduced the friction and wear. However, at 0.25 mm/s, the diameter of the wear scar tripled compared with a sliding speed of 0.5 mm/s[7]. Similarly, an increase in the

charge eventually increased the wear diameter. This wear diameter enlargement did not originate from plastic deformation due to a higher normal force. It stemmed from plastic deformation since even at the lowest normal force used in the study, the wear scar produced at 15 N was approximately 900 μm in size, exceeding the Hertzian contact diameter of 137 μm.

The tribological properties of modified silica nanoparticles are highly associated with tribopairs and lubricants. For instance, NH_2-modified silica overrides the lubricating properties of CH_3-modified silica in water for self-mated Si_3N_4. In PAO, when used to lubricate steel, CH_3-modified silica exhibited a lower CoF and wear scar diameter at additive concentrations of 0.5, 2, and 4 wt %, except at an additive concentration of 1 wt%[88]. At certain concentrations, a slight improvement was observed when both CH_3 and NH_2 organic chains were grafted onto the silica nanoparticles. However, compared with the tribological performance of the CH_3-modified silica nanoparticles, the improvement in the CoF and wear was below 10% when bifunctional silica nanoparticles were employed.

1.4.2. Graphitic materials

The tribological performance of graphitic materials employed as tribopairs is now presented. Graphite superlubricity has been widely observed at the microscale [89,90,91] or in a vacuum [92]. To realize superlubricity in a vacuum, the edge plane containing dangling bonds should be eliminated. Otherwise, owing to interfacial adhesion of the graphite edge planes, the friction increases and the lifetime of graphite sharply decreases[93]. However, when graphite was used as a tribopair in ambient air, the CoF was high. For instance, sliding ultrafine-grained graphite HPG510 against steel, ZrO_2, and Si_3N_4 produced a CoF of approximately 0.25[94]. Feeding these contacts with 2D materials such as GO, fluorinated graphene, and WS_2 resulted in a reduction of the CoF to approximately 0.05. However, the added 2D materials were rapidly consumed during sliding, and the CoF increased. The authors also proposed depositing a DLC coating on graphite to limit wear and reduce friction.

In 2018, Li et al. demonstrated that instantaneous superlubricity can be achieved by sliding highly oriented pyrolytic graphite against steel in air [95]. Multilayered graphene nanoflakes were observed on the steel surface. Although these graphene nanoflakes were irregularly distributed and did not cover the entire steel wear scar, they were considered to be the cause of superlubricity. The authors explained this instantaneous superlubricity as a statistical result where the majority of graphene nanoflakes slid against graphite without crossing atomic steps.

These atomic steps originated from a topographic height change in the multilayered graphene nanoflakes.

In addition to using bulk graphite, graphenic materials such as GO, fluorine graphene, and graphene can be directly used as a coating to achieve superlubricity. Even when only one side of the tribopair was coated with GO, graphenic materials were present on both surfaces after sliding in an aqueous glycerol solution[96]. Moreover, coating the graphenic species on silica resulted in a decrease in the CoF from 0.012 to the superlubricity regime at a sliding speed of 100 mm/s. It is important to note that even with a graphenic coating on silica, a decrease in the sliding speed eventually caused a rise in the CoF. At approximately 20 mm/s, the CoF is above 0.05, regardless of the type of graphene coating used.

Graphene nanoflakes can also be coated on a steel surface along with $MoWS_4$[97]. This coating created an intrinsic mismatch at the graphene/$MoWS_4$ interface. Sliding graphene/$MoWS_4$ coated steel in argon formed nanoscrolls, which not only prevent direct contact between steel surfaces but also generate an incommensurate sliding interface. Thus, superlubricity was achieved.

Apart from coating graphite-related materials, their properties as additives to lubricants have also drawn attention. Upon adding 0.2 mg/mL rGO to PEG200 for the lubrication of self-mated steel, the CoF decreased from 0.22 to 0.05[98]. Meanwhile, wear was reduced by 50%. The authors discovered that once the concentration of rGO exceeded a critical value, its ability to reduce friction and wear disappeared because at high concentrations, graphene oxide tended to agglomerate. The critical concentration was determined to be 0.5 mg/mL for the experimental conditions employed. Moreover, this study provides another explanation of how graphene reduces the friction and wear. In addition to directly occupying the steel wear scar, rGO formed a tribofilm with PEG molecules through hydrogen bonding in liquid. A low friction was also provided by the interlayer sheets of this tribofilm.

To facilitate the use of GO, thermal reduction is a straightforward technique that can be applied at the industrial level. However, thermal reduction creates folds and wrinkling on the GO layers. Therefore, Zhao et al. optimized the thermal reduction of GO by performing the process in sulfuric acid[99]. Using this optimized method, no obvious folds or wrinkling were observed on the GO layers. Furthermore, the interlayer spacing was enlarged, lowering the shear strength of GO. The lubrication properties correlated with the experimental conditions.

When the sliding speed was above 30 mm/s, irrespective of the maximum contact pressure (1, 1.5, or 1.86 GPa), no significant reduction of the friction was observed upon adding GO. However, when the sliding speed was 2.4 mm/s, adding 0.5 wt% GO in PAO6 stabilized the CoF at approximately 0.1 (a 10% variation in the CoF was recorded when the contact pressure changed). Notably, pure PAO6 lubricated the self-mated steel with a CoF of approximately 0.2. Wear was reduced by up to 75% upon addition of GO to PAO6.

Undoubtedly, both silica and graphitic materials can improve the tribological performance of pure lubricants. However, adding these materials does not always guarantee superlow friction, and their performance is related to the experimental conditions employed as well as the location where the lubricant serves as a carrier. Achieving a good combination of these and providing suitable conditions for silica or graphitic materials to function are part of the studies performed in this thesis.

1.5. References

[1] Holmberg, K., & Erdemir, A. (2017). Influence of tribology on global energy consumption, costs and emissions. *Friction*, *5*(3), 263-284.

[2] Mang, T., & Dresel, W. (2017). Lubricants and their market, Third Edition. Wiley-VCH verlag GmbH & Co.KGaA.

[3] Alves, S. M., Barros, B. S., Trajano, M. F., Ribeiro, K. S. B., & Moura, E. J. T. I. (2013). Tribological behavior of vegetable oil-based lubricants with nanoparticles of oxides in boundary lubrication conditions. *Tribology International*, *65*, 28-36.

[4] Zeng, Q., Dong, G., & Martin, J. M. (2016). Green superlubricity of Nitinol 60 alloy against steel in presence of castor oil. *Scientific reports*, *6*(1), 1-9.

[5] Ge, X., Li, J., Luo, R., Zhang, C., & Luo, J. (2018). Macroscale superlubricity enabled by the synergy effect of graphene-oxide nanoflakes and ethanediol. *ACS applied materials & interfaces*, *10*(47), 40863-40870.

[6] Wang, W., Xie, G., & Luo, J. (2018). Superlubricity of black phosphorus as lubricant additive. *ACS applied materials & interfaces*, *10*(49), 43203-43210.

[7] Lin, B., Ding, M., Sui, T., Cui, Y., Yan, S., & Liu, X. (2019). Excellent water lubrication additives for silicon nitride to achieve superlubricity under extreme conditions. *Langmuir*, *35*(46), 14861-14869.

[8] Müser, M. H. (2015). Theoretical studies of superlubricity. In *Fundamentals of Friction and Wear on the Nanoscale* (pp. 209-232). Springer, Cham.

[9] Hirano, M., & Shinjo, K. (1990). Atomistic locking and friction. *Physical Review B*, *41*(17), 11837.

[10] Shinjo, K., & Hirano, M. (1993). Dynamics of friction: superlubric state. *Surface Science*, *283*(1-3), 473-478.

[11] Li, J., & Luo, J. (2013). Advancements in superlubricity. *Science China Technological Sciences*, *56*(12), 2877-2887.

[12] Erdemir, A., & Martin, J. M. (Eds.). (2007). *Superlubricity*. Elsevier.

[13] Habchi, W., Matta, C., Joly-Pottuz, L., De Barros, M. I., Martin, J. M., & Vergne, P. (2011). Full film, boundary lubrication and tribochemistry in steel circular contacts lubricated with glycerol. *Tribology Letters*, *42*(3), 351.

[14] Zolper, T., Li, Z., Chen, C., Jungk, M., Marks, T., Chung, Y. W., & Wang, Q. (2012). Lubrication properties of polyalphaolefin and polysiloxane lubricants: molecular structure–tribology relationships. *Tribology Letters*, *48*(3), 355-365.

[15] Ohno, N., Shiratake, A., Kuwano, N., & Hirano, F. (1997). Behavior of some vegetable oils in EHL contacts. In *Tribology Series* (Vol. 32, pp. 243-251). Elsevier.

[16] Martin, J. M., Donnet, C., Le Mogne, T., & Epicier, T. (1993). Superlubricity of molybdenum disulphide. *Physical Review B*, *48*(14), 10583.

[17] Iwaki, M., Le Mogne, T., Fontaine, J., Martin, J. M., Watanabe, S., & Noshiro, J. (2005, January). Superlow friction of WS2 coatings in ultrahigh vacuum at low temperature. In *World Tribology Congress* (Vol. 42029, pp. 931-932).

[18] Dienwiebel, M., Verhoeven, G. S., Pradeep, N., Frenken, J. W., Heimberg, J. A., & Zandbergen, H. W. (2004). Superlubricity of graphite. *Physical review letters*, *92*(12), 126101.

[19] Song, Y., Mandelli, D., Hod, O., Urbakh, M., Ma, M., & Zheng, Q. (2018). Robust microscale superlubricity in graphite/hexagonal boron nitride layered heterojunctions. *Nature materials*, *17*(10), 894-899.

[20] Berman, D., Deshmukh, S. A., Sankaranarayanan, S. K., Erdemir, A., & Sumant, A. V. (2015). Macroscale superlubricity enabled by graphene nanoscroll formation. *Science*, *348*(6239), 1118-1122.

[21] Fontaine, J., Donnet, C., Grill, A., & LeMogne, T. (2001). Tribochemistry between hydrogen and diamond-like carbon films. *Surface and Coatings Technology*, *146*, 286-291.

[22] Klein, J., Perahia, D., & Warburg, S. (1991). Forces between polymer-bearing surfaces undergoing shear. *Nature*, *352*(6331), 143-145.

[23] Raviv, U., Giasson, S., Kampf, N., Gohy, J. F., Jérôme, R., & Klein, J. (2003). Lubrication by charged polymers. *Nature*, *425*(6954), 163-165.

[24] Han, T., Zhang, C., Li, J., Yuan, S., Chen, X., Zhang, J., & Luo, J. (2019). Origins of Superlubricity Promoted by Hydrated Multivalent Ions. *The Journal of Physical Chemistry Letters*, *11*(1), 184-190.

[25] Chen, Z., Liu, Y., Zhang, S., & Luo, J. (2013). Controllable superlubricity of glycerol solution via environment humidity. *Langmuir*, *29*(38), 11924-11930.

[26] Xu, J., & Kato, K. (2000). Formation of tribochemical layer of ceramics sliding in water and its role for low friction. *Wear*, *245*(1-2), 61-75.

[27] Li, J., Ma, L., Zhang, S., Zhang, C., Liu, Y., & Luo, J. (2013). Investigations on the mechanism of superlubricity achieved with phosphoric acid solution by direct observation. *Journal of Applied Physics*, *114*(11), 114901.

[28] Andersson, J., Erck, R. A., & Erdemir, A. (2003). Frictional behavior of diamondlike carbon films in vacuum and under varying water vapor pressure. *Surface and Coatings Technology*, *163*, 535-540.

[29] Andersson, J., Erck, R. A., & Erdemir, A. (2003). Friction of diamond-like carbon films in different atmospheres. *Wear*, *254*(11), 1070-1075.

[30] Rusanov, A., Fontaine, J., Martin, J. M., Le Mogne, T., & Nevshupa, R. A. (2008, March). Gas desorption during friction of amorphous carbon films. In *Journal of Physics: Conference Series* (Vol. 100, No. 8, p. 082050).

[31] Fontaine, J., Belin, M., Le Mogne, T., & Grill, A. (2004). How to restore superlow friction of DLC: the healing effect of hydrogen gas. *Tribology International*, *37*(11-12), 869-877.

[32] Pastewka, L., Moser, S., & Moseler, M. (2010). Atomistic insights into the running-in, lubrication, and failure of hydrogenated diamond-like carbon coatings. *Tribology Letters*, *39*(1), 49-61.

[33] Fontaine, J., Le Mogne, T., Loubet, J. L., & Belin, M. (2005). Achieving superlow friction with hydrogenated amorphous carbon: some key requirements. *Thin Solid Films*, *482*(1-2), 99-108.

[34] Fontaine, J. (2008). Towards the use of diamond-like carbon solid lubricant coatings in vacuum and space environments. *Proceedings of the Institution of Mechanical Engineers, Part J: Journal of Engineering Tribology*, *222*(8), 1015-1029.

[35] Liu, S., Zhang, C., Osman, E., Chen, X., Ma, T., Hu, Y., ... & Ali, E. (2016). Influence of tribofilm on superlubricity of highly-hydrogenated amorphous carbon films in inert gaseous environments. *Science China Technological Sciences*, *59*(12), 1795-1803.

[36] Wu, Y., Li, H., Ji, L., Ye, Y., Chen, J., & Zhou, H. (2014). Vacuum tribological properties of aC: H film in relation to internal stress and applied load. *Tribology International*, *71*, 82-87.

[37] Fontaine, J., Loubet, J. L., Mogne, T. L., & Grill, A. (2004). Superlow friction of diamond-like carbon films: a relation to viscoplastic properties. *Tribology Letters*, *17*(4), 709-714.

[38] Manimunda, P., Al-Azizi, A., Kim, S. H., & Chromik, R. R. (2017). Shear-induced structural changes and origin of ultralow friction of hydrogenated diamond-like carbon (DLC) in dry environment. *ACS applied materials & interfaces*, *9*(19), 16704-16714.

[39] Song, H., Chen, G., Chen, J., Li, H., Ji, L., & Jiang, N. (2019). Improving the Wear Life of aC: H Film in High Vacuum by Self-Assembled Reduced Graphene Oxide Layers. *Nanomaterials*, *9*(12), 1733.

[40] Sanchez-Lopez, J. C., Erdemir, A., Donnet, C., & Rojas, T. C. (2003). Friction-induced structural transformations of diamondlike carbon coatings under various atmospheres. *Surface and Coatings Technology*, *163*, 444-450.

[41] Cui, L., Lu, Z., & Wang, L. (2013). Toward low friction in high vacuum for hydrogenated diamondlike carbon by tailoring sliding interface. *ACS applied materials & interfaces*, *5*(13), 5889-5893.

[42] Donnet, C., & Erdemir, A. (Eds.). (2007). *Tribology of diamond-like carbon films: fundamentals and applications*. Springer Science & Business Media.

[43] Scharf, T. W., & Singer, I. L. (2009). Role of the transfer film on the friction and wear of metal carbide reinforced amorphous carbon coatings during run-in. *Tribology Letters*, *36*(1), 43-53.

[44] Chen, X., Zhang, C., Kato, T., Yang, X. A., Wu, S., Wang, R., ... & Luo, J. (2017). Evolution of tribo-induced interfacial nanostructures governing superlubricity in aC: H and aC: H: Si films. *Nature communications*, *8*(1), 1-13.

[45] Wang, Y., Xu, J., Ootani, Y., Ozawa, N., Adachi, K., & Kubo, M. (2019). Proposal of a new formation mechanism for hydrogenated diamond-like carbon transfer films: Hydrocarbon-emission-induced transfer. *Carbon*, *154*, 7-12.

[46] Chen, Xinchun, Takahisa Kato, and Masataka Nosaka. "Origin of superlubricity in aC: H: Si films: a relation to film bonding structure and environmental molecular characteristic." *ACS applied materials & interfaces* 6, no. 16 (2014): 13389-13405.

[47] Zhang, R. H., Wang, L. P., & Lu, Z. B. (2015). Probing the intrinsic failure mechanism of fluorinated amorphous carbon film based on the first-principles calculations. *Scientific reports*, *5*, 9419.

[48] Donnet, C., Le Mogne, T., & Martin, J. M. (1993). Superlow friction of oxygen-free MoS2 coatings in ultrahigh vacuum. *Surface and Coatings Technology*, *62*(1-3), 406-411.

[49] Donnet, C., Martin, J. M., Le Mogne, T., & Belin, M. (1996). Super-low friction of MoS2 coatings in various environments. *Tribology International*, *29*(2), 123-128.

[50] Martin, J. M. (2007). Superlubricity of molybdenum disulfide. In *Superlubricity* (pp. 207-225). Elsevier Science BV.

[51] Tomizawa, H., & Fischer, T. E. (1987). Friction and wear of silicon nitride and silicon carbide in water: hydrodynamic lubrication at low sliding speed obtained by tribochemical wear. *ASLE transactions*, *30*(1), 41-46.

[52] Sasaki, S. (1989). The effects of the surrounding atmosphere on the friction and wear of alumina, zirconia, silicon carbide and silicon nitride. *Wear*, *134*(1), 185-200.

[53] Jahanmir, S., Ozmen, Y., & Ives, L. K. (2004). Water lubrication of silicon nitride in sliding. *Tribology Letters*, *17*(3), 409-417.

[54] Deng, M., Zhang, C., Li, J., Ma, L., & Luo, J. (2014). Hydrodynamic effect on the superlubricity of phosphoric acid between ceramic and sapphire. *Friction*, *2*(2), 173-181.

[55] Kanno, Y., Suzuki, K., & Kuwahara, Y. (1984). Ammonia formation caused by the presence of water in the wet grinding of silicon nitride powder.

[56] Jahanmir, S., & Fischer, T. E. (1988). Friction and wear of silicon nitride lubricated by humid air, water, hexadecane and hexadecane+ 0.5 percent stearic acid. *STLE TRANSACTIONS*, *31*(1), 32-43.

[57] ller, K. K.. The Chemistry Silica, John Wiley and Sons. New York (1979)

[58] Chen, M., Kato, K., & Adachi, K. (2001). Friction and wear of self-mated SiC and Si3N4 sliding in water. *Wear*, *250*(1-12), 246-255.

[59] Ootani, Y., Xu, J., Adachi, K., & Kubo, M. (2020). First-Principles Molecular Dynamics Study of Silicon-Based Ceramics: Different Tribochemical Reaction Mechanisms during the Running-in Period of Silicon Nitride and Silicon Carbide. *The Journal of Physical Chemistry C*.

[60] Ferreira, V., Yoshimura, H. N., & Sinatora, A. (2012). Ultra-low friction coefficient in alumina–silicon nitride pair lubricated with water. *Wear*, *296*(1-2), 656-659.

[61] Ge, X., Halmans, T., Li, J., & Luo, J. (2019). Molecular behaviors in thin film lubrication—Part three: Superlubricity attained by polar and nonpolar molecules. *Friction*, *7*(6), 625-636.

[62] Wang, H., Liu, Y., Li, J., & Luo, J. (2016). Investigation of superlubricity achieved by polyalkylene glycol aqueous solutions. *Advanced Materials Interfaces*, *3*(19), 1600531.

[63] Liu, W., Wang, H., Liu, Y., Li, J., Erdemir, A., & Luo, J. (2019). Mechanism of Superlubricity Conversion with Polyalkylene Glycol Aqueous Solutions. *Langmuir*, *35*(36), 11784-11790.

[64] Li, J., Zhang, C., Deng, M., & Luo, J. (2014). Investigations of the superlubricity of sapphire against ruby under phosphoric acid lubrication. *Friction*, *2*(2), 164-172.

[65] Li, J., Zhang, C., & Luo, J. (2011). Superlubricity behavior with phosphoric acid–water network induced by rubbing. *Langmuir*, *27*(15), 9413-9417..

[66] Xiao, C., Li, J., Chen, L., Zhang, C., Zhou, N., Qian, L., & Luo, J. (2017). Speed dependence of liquid superlubricity stability with H 3 PO 4 solution. *RSC advances*, *7*(78), 49337-49343.

[67] Li, J., Zhang, C., & Luo, J. (2014). Effect of pH on the liquid superlubricity between Si 3 N 4 and glass achieved with phosphoric acid. *RSC advances*, *4*(86), 45735-45741.

[68] Han, T., Zhang, C., & Luo, J. (2018). Macroscale superlubricity enabled by hydrated alkali metal ions. *Langmuir*, *34*(38), 11281-11291.

[69] Li, J., Zhang, C., Sun, L., Lu, X., & Luo, J. (2012). Tribochemistry and superlubricity induced by hydrogen ions. *Langmuir*, *28*(45), 15816-15823.

[70] Li, J., Zhang, C., Deng, M., & Luo, J. (2015). Superlubricity of silicone oil achieved between two surfaces by running-in with acid solution. *RSC Advances*, *5*(39), 30861-30868.

[71] Loehle, S., Matta, C., Minfray, C., Le Mogne, T., Martin, J. M., Iovine, R., ... & Miyamoto, A. (2014). Mixed lubrication with C18 fatty acids: effect of unsaturation. *Tribology letters*, *53*(1), 319-328.

[72] Loehlé, S., Matta, C., Minfray, C., Le Mogne, T., Iovine, R., Obara, Y., ... & Martin, J. M. (2015). Mixed lubrication of steel by C18 fatty acids revisited. Part I: Toward the formation of carboxylate. *Tribology International*, *82*, 218-227.

[73] Loehle, S., Matta, C., Minfray, C., Le Mogne, T., Iovine, R., Obara, Y., ... & Martin, J. M. (2016). Mixed lubrication of steel by C18 fatty acids revisited. Part II: influence of some key parameters. *Tribology International*, *94*, 207-216.

[74] Kano, M., Martin, J. M., Yoshida, K., & Bouchet, M. I. D. B. (2014). Super-low friction of ta-C coating in presence of oleic acid. *Friction*, *2*(2), 156-163.

[75] Kuwahara, T., Romero, P. A., Makowski, S., Weihnacht, V., Moras, G., & Moseler, M. (2019). Mechano-chemical decomposition of organic friction modifiers with multiple reactive centres induces superlubricity of ta-C. *Nature communications*, *10*(1), 1-11.

[76] Bouchet, M. I. D. B., Martin, J. M., Avila, J., Kano, M., Yoshida, K., Tsuruda, T., ... & Asensio, M. C. (2017). Diamond-like carbon coating under oleic acid lubrication: Evidence for graphene oxide formation in superlow friction. *Scientific reports*, *7*(1), 1-13.

[77] Joly-Pottuz, L., Martin, J. M., Bouchet, M. D. B., & Belin, M. (2009). Anomalous low friction under boundary lubrication of steel surfaces by polyols. *Tribology letters*, *34*(1), 21-29.

[78] Bouchet, M. I. D. B., & Kano, M. (2007). Superlubricity of Diamond/Glycerol Technology Applied to Automotive Gasoline Engines. In *Superlubricity* (pp. 471-492). Elsevier Science BV.

[79] Martin, J. M., Bouchet, M. I. D. B., Matta, C., Zhang, Q., Goddard III, W. A., Okuda, S., & Sagawa, T. (2010). Gas-phase lubrication of ta-C by glycerol and hydrogen peroxide. Experimental and computer modeling. *The Journal of Physical Chemistry C*, *114*(11), 5003-5011.

[80] Li, J., Zhang, C., Ma, L., Liu, Y., & Luo, J. (2013). Superlubricity achieved with mixtures of acids and glycerol. *Langmuir*, *29*(1), 271-275.

[81] Li, J., Zhang, C., & Luo, J. (2013). Superlubricity achieved with mixtures of polyhydroxy alcohols and acids. *Langmuir*, *29*(17), 5239-5245.

[82] Makowski, S., Schaller, F., Weihnacht, V., Englberger, G., & Becker, M. (2017). Tribochemical induced wear and ultra-low friction of superhard ta-C coatings. *Wear*, *392*, 139-151.

[83] Quinchia, L. A., Delgado, M. A., Reddyhoff, T., Gallegos, C., & Spikes, H. A. (2014). Tribological studies of potential vegetable oil-based lubricants containing environmentally friendly viscosity modifiers. *Tribology International*, *69*, 110-117.

[84] Dong, J. X., Hu, Z. S., & Chen, G. X. (1999). Preparation and tribology of aerogel silica and alumina-silica as lubricant oil additives. *Lubrication Science*, *11*(3), 285-295.

[85] Stöber, W., Fink, A., & Bohn, E. (1968). Controlled growth of monodisperse silica spheres in the micron size range. *Journal of colloid and interface science*, *26*(1), 62-69.

[86] Ding, M., Lin, B., Sui, T., Wang, A., Yan, S., & Yang, Q. (2018). The excellent anti-wear and friction reduction properties of silica nanoparticles as ceramic water lubrication additives. *Ceramics International*, *44*(12), 14901-14906.

[87] Cui, Y., Ding, M., Sui, T., Zheng, W., Qiao, G., Yan, S., & Liu, X. (2020). Role of nanoparticle materials as water-based lubricant additives for ceramics. *Tribology International*, *142*, 105978.

[88] Sui, T., Song, B., Wen, Y. H., & Zhang, F. (2016). Bifunctional hairy silica nanoparticles as high-performance additives for lubricant. *Scientific reports*, *6*, 22696.

[89] Deng, H., Ma, M., Song, Y., He, Q., & Zheng, Q. (2018). Structural superlubricity in graphite flakes assembled under ambient conditions. *Nanoscale*, *10*(29), 14314-14320.

[90] Yang, J., Liu, Z., Grey, F., Xu, Z., Li, X., Liu, Y., ... & Zheng, Q. (2013). Observation of high-speed microscale superlubricity in graphite. *Physical review letters*, *110*(25), 255504.

[91] Liu, Z., Yang, J., Grey, F., Liu, J. Z., Liu, Y., Wang, Y., ... & Zheng, Q. (2012). Observation of microscale superlubricity in graphite. *Physical review letters*, *108*(20), 205503.

[92] Liu, Y., Wang, K., Xu, Q., Zhang, J., Hu, Y., Ma, T., ... & Luo, J. (2020). Superlubricity between graphite layers in ultrahigh vacuum. *ACS Applied Materials & Interfaces*.

[93] Braithwaite, E. R. (1966). Friction and wear of graphite and molybdenum disulphide. *Industrial Lubrication and Tribology*.

[94] Qi, W., Huang, P., Chen, X., Jin, J., & Luo, J. (2020). Achieving controllable friction of ultrafine-grained graphite HPG510 by tailoring the interfacial nanostructures. *Applied Surface Science*, *512*, 145731.

[95] Li, J., Ge, X., & Luo, J. (2018). Random occurrence of macroscale superlubricity of graphite enabled by tribo-transfer of multilayer graphene nanoflakes. *Carbon*, *138*, 154-160.

[96] Liu, Y., Li, J., Ge, X., Yi, S., Wang, H., Liu, Y., & Luo, J. (2020). Macroscale Superlubricity Achieved on the Hydrophobic Graphene Coating with Glycerol. *ACS Applied Materials & Interfaces*, *12*(16), 18859-18869.

[97] Jiang, B., Zhao, Z., Gong, Z., Wang, D., Yu, G., & Zhang, J. (2020). Superlubricity of metal-metal interface enabled by graphene and MoWS4 nanosheets. *Applied Surface Science*, 146303.

[98] Gupta, B., Kumar, N., Panda, K., Dash, S., & Tyagi, A. K. (2016). Energy efficient reduced graphene oxide additives: Mechanism of effective lubrication and antiwear properties. *Scientific reports*, *6*, 18372.

[99] Zhao, J., Li, Y., Mao, J., He, Y., & Luo, J. (2017). Synthesis of thermally reduced graphite oxide in sulfuric acid and its application as an efficient lubrication additive. *Tribology International*, *116*, 303-309.

Chapter II

2. Methods and calculations

In this section, tribometers used in this thesis are introduced, which accompanies how CoF is measured, how liquid film thickness and CoF arisen from the liquid are calculated and how the flash temperature is obtained. Meanwhile, a brief introduction of analytical tools is added. The calculation of element information depth in XPS and how surface roughness is calculated are explained in detail.

2.1. Introduction of tribometer and measured CoF.

Different tribometers are used in this thesis: reciprocating ball-on disk tribometers operating under low loads and high loads and in an ambient environment and a dedicated reciprocating tribometer working in an ultrahigh vacuum or in presence of gases partial pressures. As shown in Fig. 1, both low load and vacuum tribometers have an applied normal force by pressing down the ball on the disk while the high load tribometer has a normal force by moving up the disk. The tribometer in the ambient environment follows a linear trajectory on the disk while the vacuum tribometer has a curved trajectory. The sliding speed always obeys a sine curve and reaches its maximum value in the mid of the trajectory. The reason why there are two tribometers in the ambient environment is due to the different sensibilities of force sensors. Choice has been made to measure friction either more accurately or with a large range. The tribometer designed for the high load can apply a normal force up to 250 N with a sensibility of the tangential force of 0.25 N. Concerning the tribometer operating under low load, a normal load up to 10 N is recommended and the sensibility of tangential force is around 0.005 N.

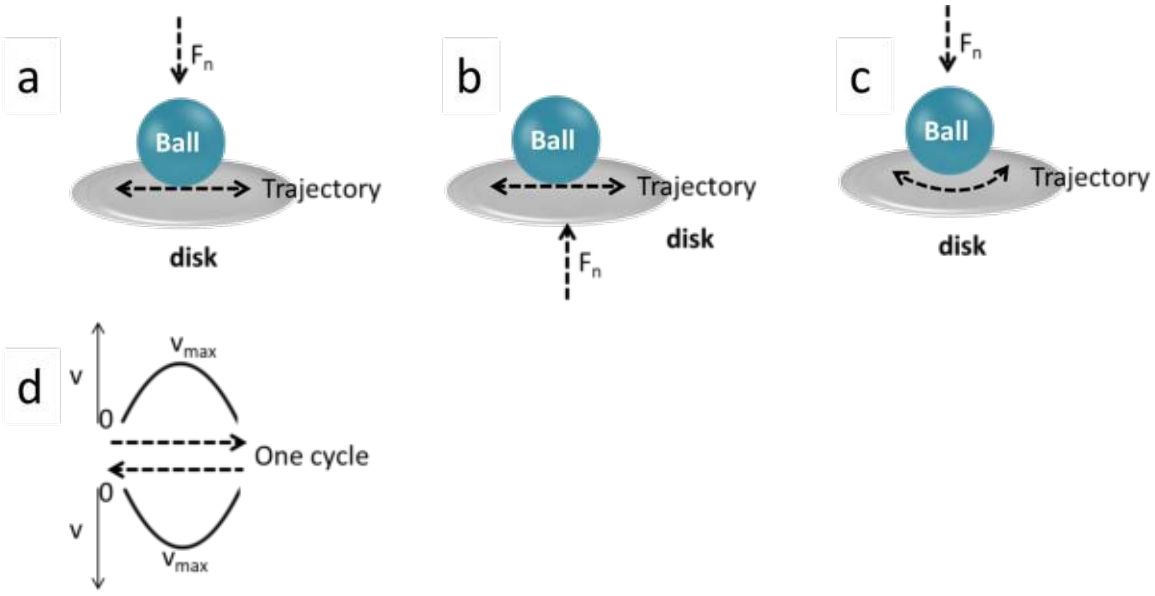

Fig. 1 Reciprocating tribometers under **a** low load, **b** high load, **c** in a vacuum. **d** correlation of position and sliding speed in one cycle.

Due to the reciprocating movement in tribometers used in this thesis, the friction coefficient (CoF) can simply be calculated as half of the tangential force difference at the same position in a round trip. Details are demonstrated in Fig.2.

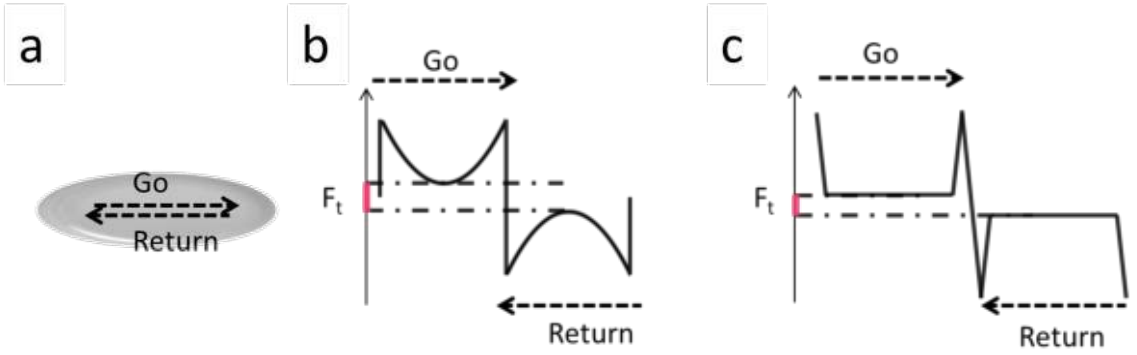

Fig. 2 a One cycle of sliding, to schematically demonstrate the difference between direction change in one round trip, trajectory with different direction are separated into 2 lines, which took place in the same line. Moreover, moving to the right side is named 'Go', moving to the left side is called 'return'. Two typical Ft shaped as a function of position are shown in **b**, **c**. Their shape is associated with the type of lubricants and materials. The half-height of the pink bar is taken as the actual friction at maximum speed and is used to calculate CoF.

2.2. Central film thickness calculations

The lubricant film thickness is calculated using the Nijenbanning-Venner-Moes[1] equation for elastohydrodynamic (EHL) lubrication of a ball on flat contact. The central film thickness h_c is calculated by

$$h_c = r_x(2U)^{0.5}\left(\left(H_{RI}^{3/2} + (H_{EI}^{-4} + H_{00}^{-4})^{-3/8}\right)^{2s/3} + (H_{RP}^{-8} + H_{EP}^{-8})^{-s/8}\right)^{1/s}$$

with $s = 1.5\left(1 + e^{-1.2\times H_{EI}/H_{RI}}\right)$. Here r_x is the radius of curvature parallel to the sliding direction and the other numbers $U, H_{00}, H_{RI}, H_{EI}, H_{RP}$ and H_{EP} are given in Table 1. The actual lubrication regimes are determined by evaluating the dimensionless lambda parameter that is defined as the ratio between the central film thickness and the composite roughness of the two surfaces:

$$\lambda = h_c / \sqrt{R_{\mathrm{RMS,pin}}^2 + R_{\mathrm{RMS,disc}}^2}.$$

Table 1: The dimensionless numbers entering the Nijenbanning-Venner-Moes formula. Here α, η_0, u, and w are pressure-viscosity coefficient, lubricant dynamic viscosities, sliding speed, and applied normal load, respectively. The reduced Young's modulus E' and reduced radius of curvature D are calculated from $1/E' = 2(1 - v_A^2/E_A + 1 - v_B^2/E_B)$ and $D = r_x/r_y$, respectively. E and ν are the elastic modulus and Poisson's ratio, respectively. r_y is the radius of curvature perpendicular to the sliding direction.

$\mathrm{H_{00}} = 1.8\mathrm{D}^{-1}$	$\mathrm{L} = \mathrm{G}(2\mathrm{U})^{0.25}$
$\mathrm{H_{RI}} = 145\left(1 + 0.796\mathrm{D}^{14/15}\right)^{-15/7}\mathrm{D}^{-1}\mathrm{M}^{-2}$	$\mathrm{M} = \mathrm{W}/(2\mathrm{U})^{0.75}$,
$\mathrm{H_{EI}} = 3.18\left(1 + 0.006\ln\mathrm{D} + 0.63\mathrm{D}^{4/7}\right)^{-14/15}\mathrm{D}^{-1/15}\mathrm{M}^{-2/15}$	$\mathrm{G} = \alpha\mathrm{E}'$
$\mathrm{H_{RP}} = 1.29(1 + 0.691\mathrm{D})^{-2/3}\mathrm{L}^{2/3}$	$\mathrm{U} = \eta_0\mathrm{u}/\mathrm{E}'\mathrm{r_x}$
$\mathrm{H_{EP}} = 1.48\left(1 + 0.006\ln\mathrm{D} + 0.63\mathrm{D}^{4/7}\right)^{-7/20}\mathrm{D}^{-1/24}\mathrm{M}^{-1/12}\mathrm{L}^{3/4}$	$\mathrm{W} = \mathrm{w}/(\mathrm{E}'\mathrm{r_x^2})$,

2.3. Theoretical CoF arisen from liquid (Couette flow)

Derived from the definition of viscosity, the shearing force (F) originated from liquid viscosity can be written as:

$F = \eta_p A v / h_c$

Where v is the sliding speed, h_c is the thickness of the center liquid film. A is the contact area. η_p is the viscosity of liquid at pressure p.

It is worthy to mention that under pressure (p), η is associated with dynamic viscosity (η_0) and visco-pressure coefficient (a). Their relationship is given in the equation:

$\eta_p = \eta_0 \times e^{(a \times p)}$

$p = F_n / A$

Here, F_n is the normal force. Therefore, CoF is finally obtained by dividing F_n by F.

2.4. Flash temperature calculation.

Maximum flash temperature rise ($\theta_{\max}$) of surfaces is calculated by Greenwood's fomula[2]:

$\theta_{\max} = 0.5895\, Q_{\text{in}}/(bk(J + 2.471)^{0.5})$,

where b is the half-width of the contact, k is the thermal conductivity, J is the non-dimensional speed of the surface relative to the contact defined as $J = ub/\chi$. Here, u is the speed of the surface relative to the contact. χ is the thermal diffusivity. Q represents heat dissipation rate in sliding contact and can be calculated as $Q = \mu w u_s$, where μ, w, u_s are the friction coefficient, normal force, and the velocity difference between the two surfaces. Q_{in} is the rate at which heat enters the surface and can be written as $Q = aQ_{\text{in}}$, where a is heat partition fraction. It follows the equation[3]:

$(1 - a)/a = (J_{\text{ball}} + 1.299)^{0.5}/(J_{\text{disk}} + 1.299)^{0.5}$,

where J_{ball} and J_{disk} is the non-dimensional speed of the ball and flat disk, respectively.

2.5. Analytical tools

In this thesis, information about all the analytical tools used is listed in table 2.

Table 2: Summary of analytical tools. SEM, EDS refers to scanning electron microscopy, energy-dispersive X-ray spectroscopy, respectively. XPS is the abbreviation of X-ray photoelectron spectroscopy. The full name of ToF-SIMS is the time of flight- secondary ion mass spectrometry. LTQ represents a linear trap quadrupole.

	Model	Supplier	Location of supplier
Digital microscopy	VHX-1000 and VHX-6000	Keyence	Osaka, Japan
Interferometry	ContourGT-X	Bruker	Billerica, USA
SEM+ EDS	MIRA3	TESCAN	Fuveau, France
Raman	inVia™ Qontor® confocal Raman microscope	Renishaw plc	Wotton-under-Edge, United Kingdom

XPS	ULVAC-PHI Versa Probe II spectrometer	ULVAC-PHI, INC.	Chigasaki, Kanagawa, Japan
ToF-SIMS	ToF-SIMS 5	IONTOF	Münster, Germany
LTQ Orbitrap XL hybrid tandem MS	Orbitrap MS	ThermoFisher Scientific	Bremen, Germany

2.6. The information depth calculation of element peak from XPS

99.7 % of element signals came from a depth of $3\lambda \sin\theta$ while 68% signals are from $\lambda \sin\theta$ [4], where λ and θ are the inelastic mean free path and take-off angle, respectively. λ can be estimated as[2]

$$\lambda = E/\{E_p^2[\beta \ln(\gamma E) - (C/E) + (D/E^2)]\},$$

where E is the energy of the electron, $E_p = 28.8(N_v\rho/M)^{0.5}$, $\beta = 0.0216 + 0.944/\left(E_p^2 + E_g^2\right)^{0.5} + 7.39 \times 10^{-4}\rho$, $\gamma = 0.191\rho^{-0.5}$, $C = 1.97 - 0.91U$, $D = 53.4 - 20.8U$, and $U = N_v\rho/M = E_p^2/829.4$. N_v, ρ, M, and E_g are the number of valence electrons, the density of the material, atomic mass, and energy gap of the material, respectively.

2.7. Surface roughness, the radius of ball curvature, wear volume obtained from the interferometer.

An interferometer is a machine to obtain 3D topographic information of samples. The typical image obtained by the interferometer is presented in Fig. 3a. Since it is a 3D map, any height distribution of x, y-axis can be acquired as the image presented at the bottom of Fig. 3a. After fitting the image by subtracting its curvature, surface roughness (S_a) can be directly calculated from this 3D profile image like in Fig. 3b through the calculation of arithmetical mean deviation. Since it is capable to subtract curvature information from a surface, by measuring the radius of its curvature, a ball radius is obtained. When wear is present on surfaces, a local radius of wear scar can be simply retrieved by subtracting curvature information of wear scar.

Similarly, comparing the 3D interferometer image Fig. 3a with a curvature which has the same radius, their difference represents the wear volume.

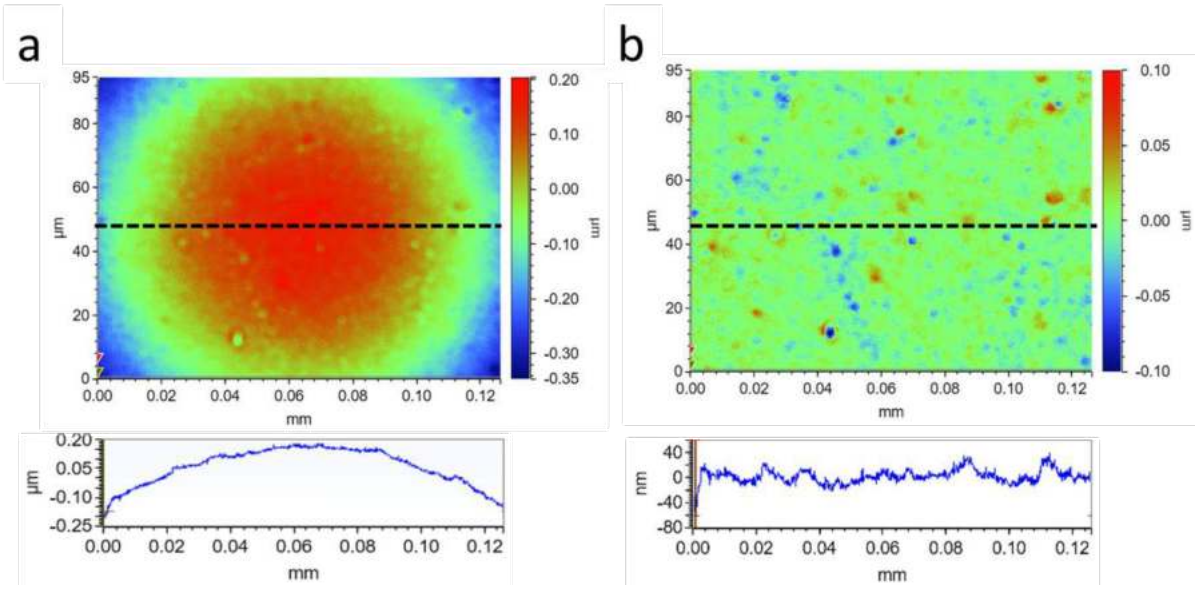

Fig. 3 3D interferometer image of a ball **a** without fitting with curvature function **b** after fitting with curvature function. Those images under are the depth profile corresponding to the black line in the upper image.

2.8. References

[1] Nijenbanning, G. C. H. H., Venner, C. H., & Moes, H. (1994). Film thickness in elastohydrodynamically lubricated elliptic contacts. *Wear*, *176*(2), 217-229.

[2] Greenwood, J. A. (1991). An interpolation formula for flash temperatures. *Wear*, *150*(1-2), 153-158.

[3] Reddyhoff, T., Schmidt, A., & Spikes, H. (2019). Thermal conductivity and flash temperature. *Tribology Letters*, *67*(1), 22.

[4] http://www.xpsfitting.com/search/label/IMFP.

Chapter III

3. Superlubricity in vacuum

3.1. Wearless superlubricity by sliding Si_3N_4/aC:H in ultrahigh vacuum

3.1.1. Experimental parts

Guiding by the sequence explained in the introduction, some experiments in UHV are presented first. The experimental details are listed in table 1:

Table 1: Experimental conditions in vacuum

Tribometer type	Reciprocating
Vacuum	500 nPa
Temperature	30°C
Max sliding speed	0.2 mm/s
Maximum Hertzian contact pressure	565 MPa

Mechanical properties of tribo-pair materials are presented in table 2:

Table 2: Mechanical properties of materials. The hydrogen content of the aC:H coating is about 36 atomic %. aC:H coatings have been deposited on steel substrate.

	Suppliers	Production method	Diameter-mm	Elastic modulus -GPa	Poisson ratio
Steel ball	Total	-	12.7	210	0.3
aC:H ball	HEF	Plasma enhanced CVD	10	80	-
SiC ball	Metalball	Hot pressing	11.12	410	0.18
Si3N4 ball	Metalball	Hot pressing	12	310	0.27
aC:H disk	HEF	Plasma enhanced CVD	-	80	-

3.1.2. Results

Using aC:H with 36% hydrogen as a coated steel disk, no matter the counter-part is steel, aC:H, SiC, or Si_3N_4, the CoF decreases down to the regime of superlubricity within 10 minutes for the 4 pairs (Fig. 1a). Only a slight difference has been recorded regarding the CoF at the end of the test. Steel/aC:H pair shows the highest CoF around 0.01 while steel/Si_3N_4 gives the lowest value of 0.0036 (Fig. 1b). Interestingly, except for the steel/aC:H case, no visible wear scar has been detected on the balls (Fig. 1c-f). The black substance visible optically on the steel ball wear scar is thought to be a transfer film of aC:H on the ball[1]. On

the disk side, except for the case of steel/aC:H showing large wear debris inside wear scar, disk wear scars of other tribo-pairs display a white color and their wear scar width is around 90 μm (Fig. 1g-j), that is slightly larger than the corresponding Hertzian diameter. This indicates that some plastic deformation occurs during shearing.

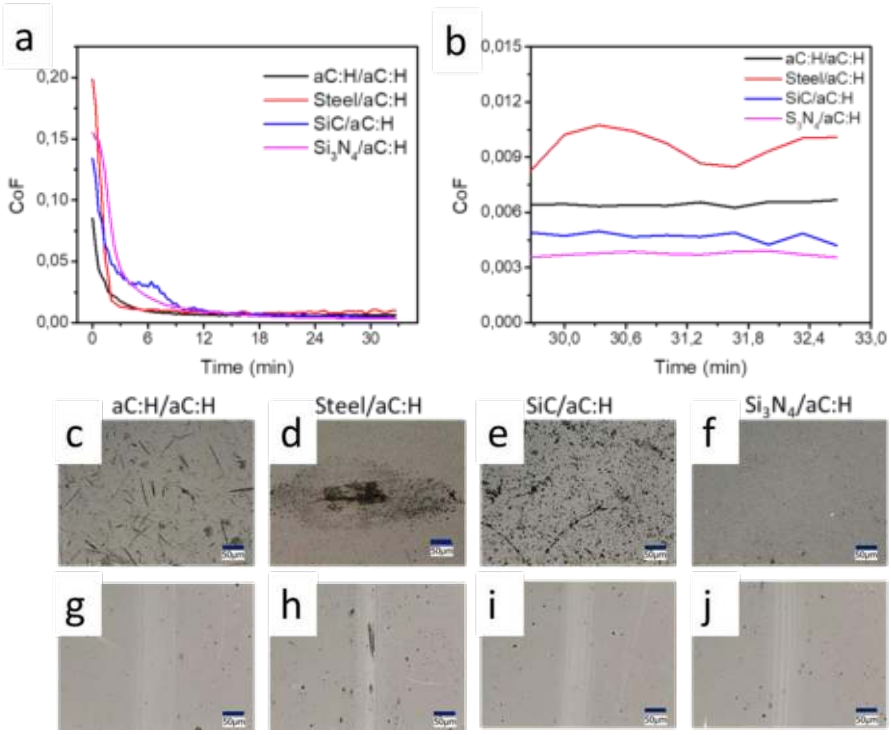

Fig. 1 a Friction evolution as a function of time for all 4 tribo-pairs **b** friction values for last 3 minutes before the end of test **c-f** optical images of wear scar on the balls, which are displayed in the following sequence from left to right: aC:H, steel, SiC, Si_3N_4 **g-j** optical images of wear scar on disks in the same sequence.

Because it demonstrates the lowest CoF without any visible wear on the Si_3N_4 ball, the a-C:H steel/Si_3N_4 case is chosen here for complementary investigations under different normal loads to understand its superlubricity mechanism. Three different normal forces of 1.9, 5, and 8 N (corresponding to maximum Hertzian pressure of 575, 794, and 919 MPa, respectively) are used in this set of experiments. The corresponding Hertzian contact diameters are 79, 110, and 128 micrometers. Fig 2a shows that an increase of normal load has the effect of cutting down the running-in period but it does not change the final CoF value. The increase of normal load leads to an increase in the wear width on the disk (Fig. 2e-g). However, the ratio between wear scar depth and calculated Hertzian diameter is always below 1.1. In all cases, the wear depth is under 10 nm because it cannot be detected by the interferometer.

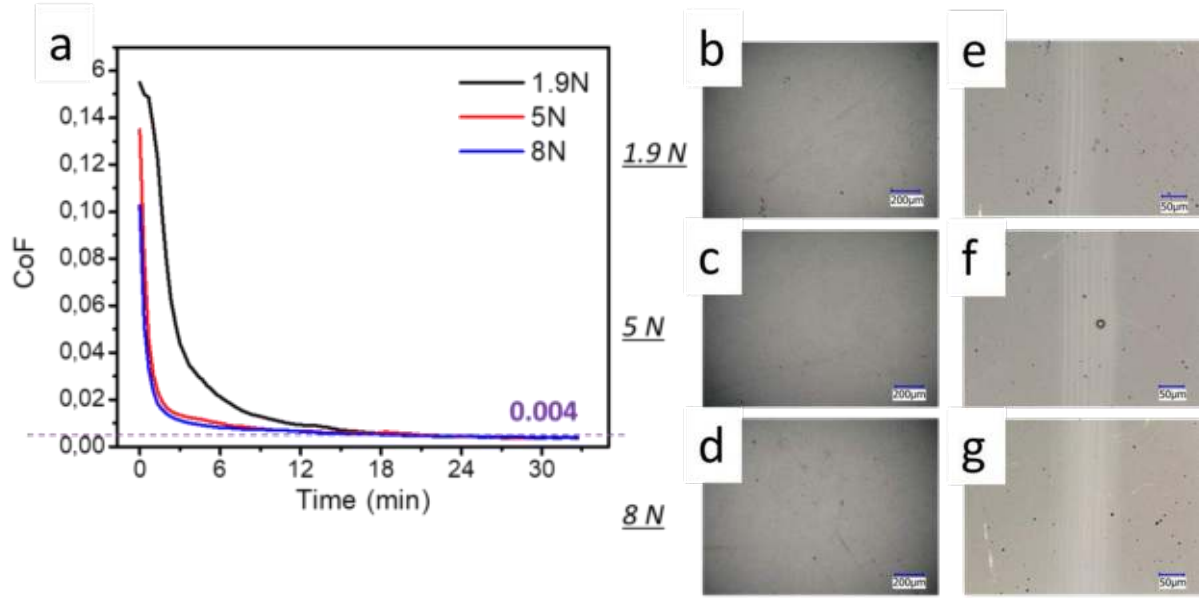

Fig. 2 a Friction behavior of Si_3N_4/aC:H under 3 normal loads: 1.9, 5, and 8N. **b-d** optical images of wear scar on the balls, which are arranged in the following sequence from upside to the downside: 1.9, 5, 8 N.

Carbon/hydrogen film transfer is a commonly encountered phenomenon when high hydrogen content aC:H slides against other materials in UHV[2]. However, carbon contamination hinders the way to trace if aC:H film is effectively present on Si_3N_4 surface after friction in UHV. To solve this issue, adventitious carbon is removed before the sliding test in a vacuum. As shown in Fig 3a, the removal of adventitious carbon sharply decreases the running-in time even though it doesn't impact the final CoF. Interestingly, after the removal of the carbon element on Si_3N_4, a sliding test brings carbon back to Si_3N_4. This corresponds to the newborn C_{1s} peaking at around 284 eV in Fig. 2b. It is also found that the surface of Si_3N_4 ball contains Ca, Al, Fe elements in small quantities, which are used as binders during hot-pressing. The content of them is less than 5% (table 3). The biggest change before and after friction of Si_3N_4 is the carbon content augmentation from 5% to 27%.

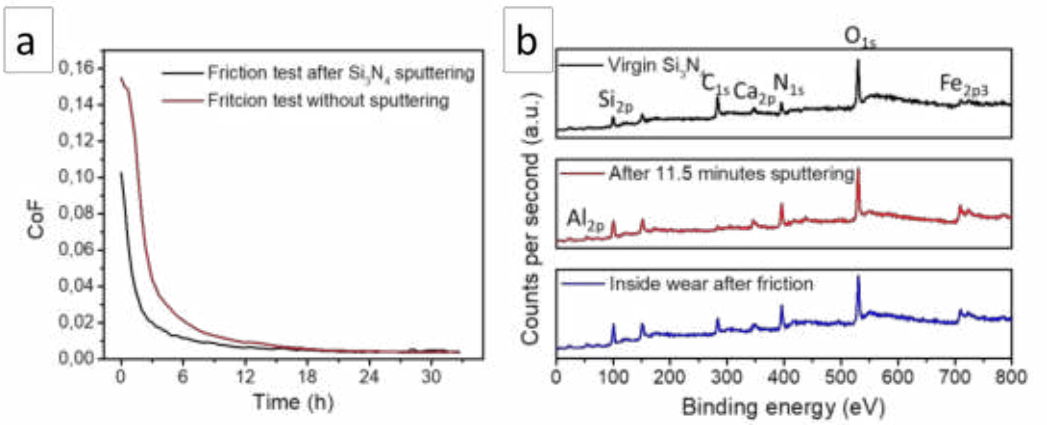

Fig. 3 a Different friction evolution trends with and without the presence of adventitious carbon on Si_3N_4 ball. Adventitious carbon is removed by ion sputtering **b** XPS survey spectra of virgin Si_3N_4, Si_3N_4 after ion sputtering, and Si_3N_4 after friction.

Table 3: Elemental distribution in percentage from survey spectra.

	Si_{2p}	C_{1s}	N_{1s}	O_{1s}	Al_{2p}	Ca_{2p}	Fe_{2p3}
Virgin Si_3N_4	7.2	39.0	10.0	42.4	0	0.9	0.5
Sputtering	19.9	5.7	24.0	38.8	3.7	3.0	4.9
Wear scar	17.9	26.5	17.9	32.3	2.0	1.6	1.8

To determine the chemical states of each element, all spectra are carefully calibrated by fixing the N1s peak of Si_3N_4 at 397.3 eV[3]. The reason to choose N1s peak instead of Si 2p for calibrating is to eliminate the influence of C-Si-O binding energy that locates at similar binding energy than Si 2p peak in Si_3N_4 [3,4]. High-resolution C_{1s} peak fitting reveals that a new C_{1s} peak grows after friction and is constituted by oxygenated functions O-C=O, C=O, C-O, C-C/C=C, Si-C-O (Fig. 4c). Among them, C-C/C=C and Si-C-O are the most pronounced and represent 12.9% and 9.2% of the signal coming from C-C/C=C and Si-C-O, respectively (Table 4). Furthermore, this Si-C-O peak doesn't exist in the C_{1s} peak performed on virgin Si_3N_4 indicating that the Si-C-O bond is formed under the shearing process. Taking Si_3N_4 as bulk material, 68% of C_{1s} signal comes from 1.6 nm depth and 68% of N1s signal comes from 1.8 nm depth. However, with similar information depth, the Si-C-O signal at 283.6 eV is significantly less than the peak ratio at 101.7 eV. This suggests that a part of the signal at 101.7 eV comes from the Si_3N_4 substrate. Due to the C-Si-O bond sharing similar peak energy as Si_3N_4, the merging of those two peaks results in an augmentation of the peak's FWHM from 1.9 eV to 2.2 eV (Table 4).

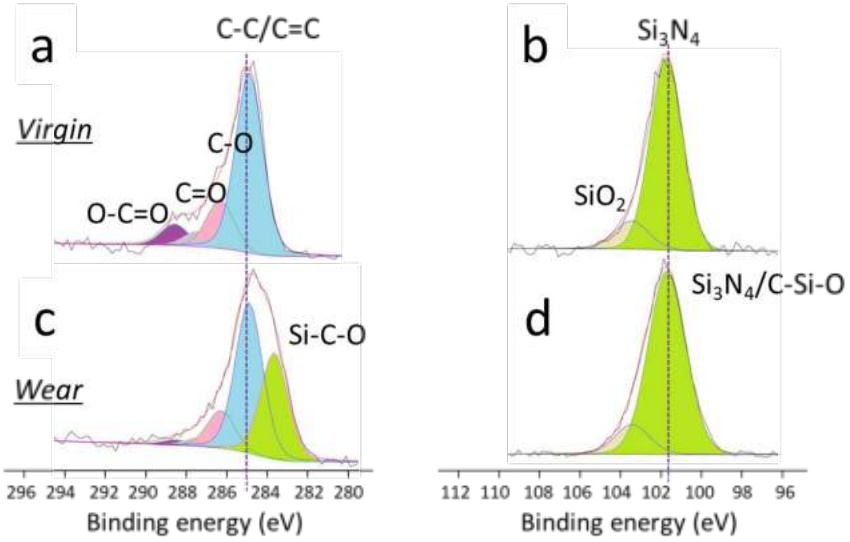

Fig. 4 C_{1s} peaks of **a** virgin Si_3N_4 **c** Si_3N_4 worn surface. Si_{2p} peaks of **b** virgin Si_3N_4 **d** Si_3N_4 worn surface.

Table 4: Fitting details of C_{1s} and Si 2p peaks.

Virgin Si_3N_4	C_{1s}					Si_{2p}	
Survey percentage -%	39.0					7.2	
Peaks	Si-C-O	C-C/C=C	C-O	C=O	O-C=O	Si_3N_4	SiO_2
Energy -eV	-	284.9	286.3	287.4	288.6	101.7	103.4
FHWM -eV	-	1.6	1.6	1.6	1.6	1.9	2.0
Percentage -%	-	26.4	7.1	2.3	3.2	6.2	1.0
Si_3N_4 worn surface	C_{1s}					Si_{2p}	
Survey percentage -%	26.5					17.9	
Peaks	Si-C-O	C-C/C=C	C-O	C=O	O-C=O	Si_3N_4 /C-Si-O	SiO_2
Position -eV	283.6	284.9	286.3	287.4	288.6	101.7	103.4
FHWM -eV	1.6	1.6	1.6	1.6	1.6	2.2	2.0
Percentage -%	9.2	12.9	3.2	0.7	0.5	15.5	2.4

3.1.3. Conclusions

In summary, the XPS analysis result shows the transfer of a carbon film from aC:H disk to Si_3N_4 ball during the first cycles. As a result of this carbon transfer, the C-C/C=C content greatly increases on Si_3N_4 ball after friction together with Si-C-O chemical bond showing on

Si_3N_4 ball. The oxidation layer on Si3N4 ball may serve as an active reaction site, taking out carbon from aC:H disk and forming the Si-C-O bond. Since aC:H used here is highly hydrogenated, the majority of carbon is expected to be transferred in form of C-C/C=C containing hydrogen termination. Along the transfer taking place, the contact among asperities changes from SiOx layer against aC:H to highly hydrogenated carbonaceous layer against aC:H. Profiting from the well-known low shear strength between hydrogen atoms, superlubricity is established between Si_3N_4 and aC:H and this for the first time. This hypothesis needs to be further confirmed by computer simulation and the impact of the oxidation layer of Si_3N_4 on friction and wear needs to be studied more deeply.

3.2. References

[1] Fontaine, J. (2008). Towards the use of diamond-like carbon solid lubricant coatings in vacuum and space environments. *Proceedings of the Institution of Mechanical Engineers, Part J: Journal of Engineering Tribology*, *222*(8), 1015-1029.

[2] Chen, X., Zhang, C., Kato, T., Yang, X. A., Wu, S., Wang, R., ... & Luo, J. (2017). Evolution of tribo-induced interfacial nanostructures governing superlubricity in aC: H and aC: H: Si films. *Nature communications*, *8*(1), 1-13.

[3] C.D. Wagner, A.V. Naumkin, A. Kraut-Vass, J.W. Allison, C.J. Powell, J.R.Jr. Rumble, NIST Standard Reference Database 20, Version 3.4 (web version) (http:/srdata.nist.gov/xps/) 2003.

[4] Kaur, A., Chahal, P., & Hogan, T. (2015). Selective fabrication of SiC/Si diodes by excimer laser under ambient conditions. *IEEE Electron Device Letters*, *37*(2), 142-145.

Chapter IV

4.Superlubricity in polyols

4.1. Superlubricity of glycerol by self-sustained chemical polishing: the case of steel/ta-C in glycerol

Sci.Rep. Doi:10.1038/s41598-019-42730-9

4.1.1. Experimental parts

Glycerol is first introduced as a liquid lubricant in this thesis because of its excellent and well -known lubricating properties. However, previous researches mainly focused on its properties in full EHL lubrication[1,2]. Its excellent lubricity at the EHL regime arises from its low but suitable viscosity-pressure coefficient[3] (5.9 1/GPa at 30°C), which is far from the ones of water (near zero) and engine oil (around 30 1/GPa). High viscosity-pressure coefficient like engine oil requires high energy input to shear the liquid under high sliding speed while low viscosity-pressure coefficient such as water requires not only high sliding speed[4] but also extremely low contact pressure[5] to establish liquid film. For glycerol, a sliding speed of 150 mm/s at 25°C is sufficient for reaching the superlubricity of steel in presence of glycerol[6]. Nevertheless, at low sliding speeds used in this research, shearing glycerol film usually provides a CoF higher than 0.01.

On the other hand, ta-C is used in this study instead of aC:H since the tribological performance of aC:H is sensitive to environment. For instance, in full lubrication of water, sliding alumina ball against aC:H results in a CoF of 0.7 while replacing aC:H with ta-C would keep CoF below 0.1[7]. ta-C also shows better lower CoF than aC:H in oleic acid[8]. Therefore, ta-C is chosen and several tribo-pairs beased on steel and ta-C are investigated in this chapter. The details about the materials are listed in table 1.

Table 1: Mechanical properties of materials.

	Suppliers	Production method	Diameter-mm	Elastic modulus-GPa	Initial roughness-nm	Hardness - GPa
Steel ball	PCS instruments	-	12.7	210	19.7	8
Steel disk	PCS instruments	-	-	210	2.2	8
ta-C ball	Onward	Filtered laser-	10	650	32.3	65

		arc PVD				
ta-C disk	Fraunhofer IWS	Filtered laser-arc PVD	-	650	2.7	55

As mentioned, the tribological performance of glycerol at low sliding and relatively high temperatures is the focus of this study. Thus, 3 mm/s and 50°C are chosen (Table 2).

Table 2: Experimental conditions

Tribometer type	Reciprocating
Lubricant	Glycerol
Temperature	50 °C
Sliding speed	3 mm/s
Maximum Hertzian contact pressure	577 MPa

4.1.2. Results

The AFM images (Fig. 1) show that the as-received steel ball has an initial Ra of 19.7 nm. The steel flat itself has a roughness of 4 nm and the ta-C-coated ball has a higher roughness of 40 nm. The ta-C flat surface is much smoother with a Ra equal to 2.7 nm and the black points correspond in AFM image are holes. Note that carbon droplets from the deposition process have been removed by polishing. These two materials are representative of practical use in industrial applications, especially in the automotive industry.

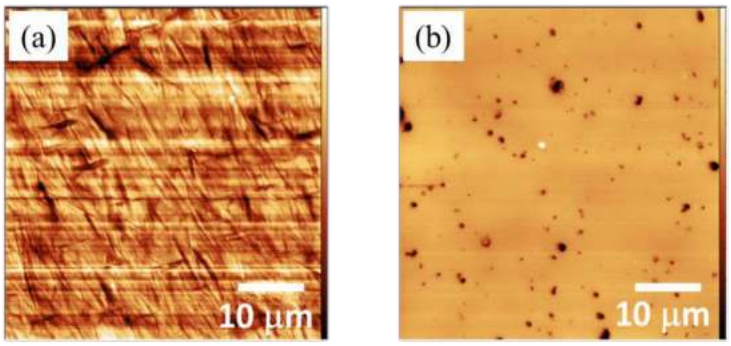

Fig. 1 AFM images of as-received surfaces of (a) steel ball and (b) ta-C-coated steel flat.

Figure 2 (a) shows the evolution of the CoF as a function of time between self-mated steel samples in glycerol at a sliding speed of 3 mm/s and a temperature of 50 °C. The evolution of

the friction can be divided into three parts: (i) starting with the running-in process (approximately 0.05 h), the CoF rapidly decreases from 0.06 to 0.016; (ii) low friction remains stable until approximately 0.25 h. The friction coefficient then slowly increases from 0.016 to 0.03 over 0.31 h. (iii) The CoF then drastically increases to 0.19 and maintains a high friction value afterward.

The optical images in Figure 2 (b) show the aspects of worn steel surfaces. After the friction test, the steel ball showed a wear scar diameter of approximately 150 μm and is covered with many scratches. The flat surface exhibited numerous scratches and shows clearly the wear track. This observation was confirmed by the roughness profiles of the tribo-pair measured by interferometry. As a result of these scratches emerging, the contacting surfaces became rough and the lubricity of the liquid film was destroyed, corresponding to high friction at the end of the test. However, during the first 0.56 h, the damage on surfaces was negligible.

During the low-friction period, no measurable wear was detected on the flat; however, the wear volume of the ball was 1069 μm^3. At the end of the test, wear volumes of 1281 μm^3 and 58 μm^3 were measured for the ball and flat, respectively. In a previous paper, the occurrence of low friction in steel/steel contact was attributed to a thin fluid film of glycerol easily shearing and an nm-thick water film forming due to the degradation of glycerol under severe conditions. Therefore, the steel/steel combination lubricated by glycerol cannot provide low friction and low wear over a long period.

The self-mated ta-C friction pair tested in glycerol at 50 °C and 3 mm/s shows a decreasing CoF from 0.07 to 0.06 during the first 0.4 h. Afterward, CoF then remains stable at 0.06 until the end of the test. No measurable wear is observed on the ta-C flat, whereas a wear diameter of 103 μm and colour change from initial yellow to green is observed (Fig. 2c). The color is due to the thickness change of the optically transparent ta-C coating modifying the refraction of visible light, although wear could not be detected by interferometry. In this case, the relatively high CoF limits further applications.

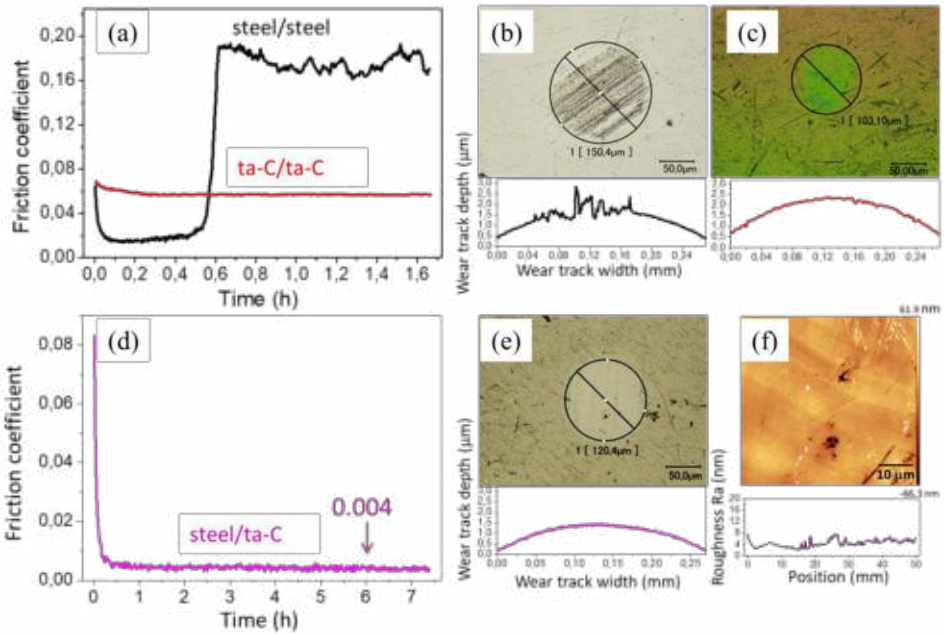

Fig. 2 Friction curve as a function of time for lubrication of (a) steel/steel, ta-C/ta-C and (d) steel/ta-C tribo-pairs by glycerol at 50 °C, a sliding speed of 3 mm/s, and a P_{max} of 577 MPa. Optical images and depth profiles of wear scars on steel balls for the combinations (b) steel/steel, (c) ta-C/ta-C, and (e) steel/ta-C at the final stage. (f) AFM images corresponding to the region inside the wear scar of the steel ball after the 7.4 h-duration test. Topographic line-scans across the wear scar diameter are shown in all cases.

Eventually, the steel flat was replaced with a ta-C-coated disk. Figure 2 (d) shows the CoF of the steel ball sliding against the ta-C-coated flat under the same conditions as the self-mated steel and ta-C pairs. During the first 0.5 h running-in period, the CoF decreased sharply from 0.084 to 0.004. Thereafter, the super low friction coefficient (0.004) persists until the end of the test (*i.e.* 7.5 h). This amazing and unexpected result leads to further investigation. After the long-duration test, no measurable wear was observed on the ta-C flat. On the steel ball, the wear track diameter was approximately 120 µm corresponding to a final contact pressure of 300 MPa (Fig. 2 e). The AFM image in Figure 2 (f) corresponds to inside the wear track on the steel ball and shows an extremely smooth surface with Ra of 4.30 nm. Polishing occurred within the contact zone.

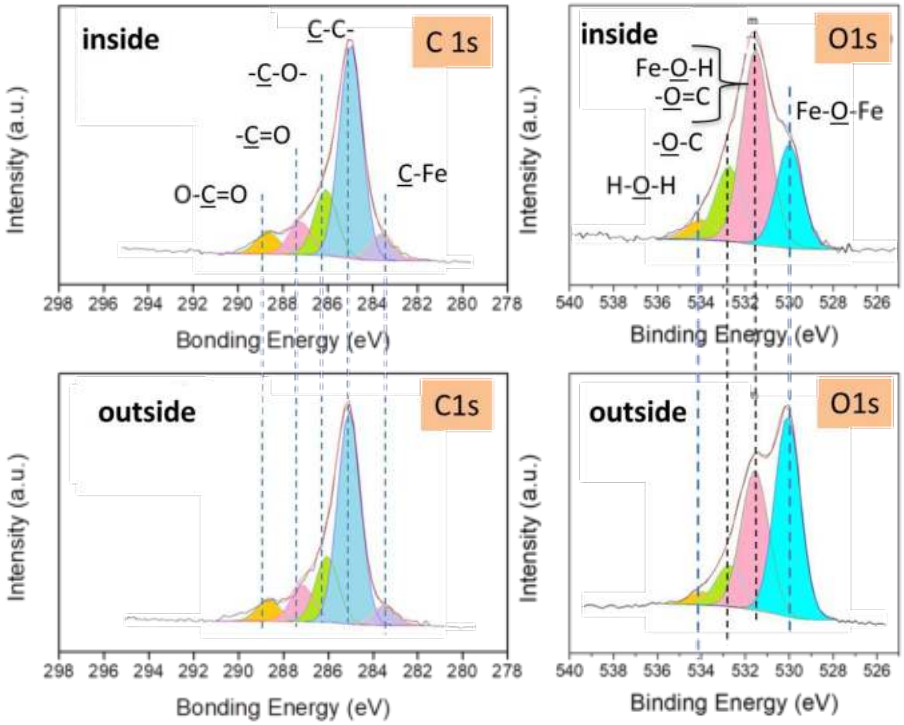

Fig. 3 High-resolution C_{1s} and O_{1s} XPS spectra recorded on the steel ball (steel/ta-C tribo-pair slid in glycerol at 50°C). Degradation species of glycerol (ketones, acids, etc.) are found on the steel surface, whereas more iron hydroxide is found inside the wear scar.

To study chemical reactions between the surfaces and glycerol, the regions inside and outside the wear track on the steel ball were analyzed by XPS (Fig. 3). More attention was paid to the C_{1s} and O_{1s} oxygen photopeaks in both cases. A characteristic peak corresponding to iron oxides is observed at binding energy (BE) of approximately 530.0 eV, in good agreement with data from the literature. Also, the peak at 531.4 eV BE is attributed to either iron hydroxides or carbonyl (O=C) bond [9]. The corresponding low intensity of the (C=O) contribution at the C_{1s} peak at 288 eV BE confirms the predominance of hydroxides in the wear scar. Because hydroxides usually cover the top of an oxide layer, its thickness is approximately 1 nm. The peak detected at 533.8 eV BE could correspond to water molecules adsorbed on hydroxides, water may originate from the degradation of glycerol or the absorption of molecular water from the humid air because iron hydroxide is hydrophilic. The peak at approximately 532.5 eV BE is attributed to (C-O-) bonds present in glycerol, with a higher contribution inside the wear track than outside. Carbonyl and carboxyl groups (C=O and O-C=O, respectively) are observed both inside and outside the steel wear scar. These chemical species originate from the chemical reaction of glycerol with the oxidized steel surface.[9]

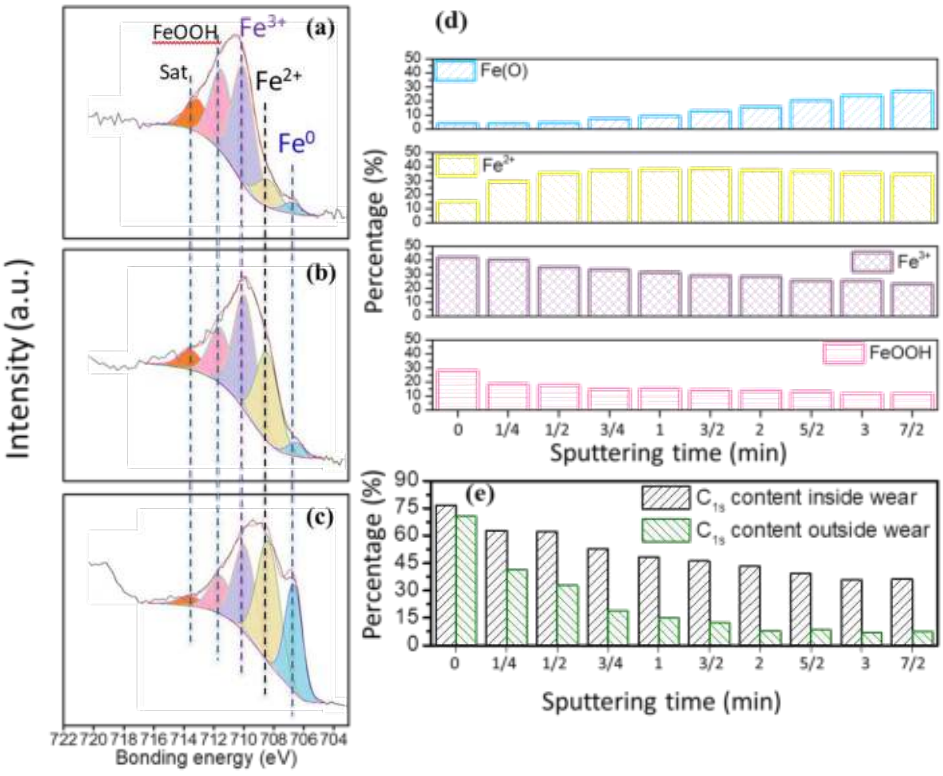

Fig. 4 High-resolution Fe_{2p} XPS spectra after different sputtering times (take-off angle 25°) in the case of a steel ball against a ta-C flat in glycerol at 50 °C, speed 3 mm/s: (a) before sputtering, (b) after 0.25 min sputtering, (c) after 3.5 min sputtering. (d) Evolutions of the peak intensities as a function of the sputtering time. (e) Carbon content has the intensity ratio $C_{1s}/(C_{1s}$ + O1 s + Fe 2p3/2) both inside and outside the wear track as a function of the sputtering time.

This interesting hydroxide layer is studied in more detail in the Fe 2p XPS spectrum recorded at a take-off angle of 25° (Fig. 4). The steel surface was sputtered with argon ions with sputtering times ranging from 0.25 min to 3.5 min to obtain depth concentration profiles of the chemical species. The iron oxide already detected based on its O_{1s} oxygen peak can now be separated into two contributions: FeO/Fe_3O_4 (at 712 eV BE as Fe^{2+}) and Fe_2O_3 (at 714 eV BE as Fe^{3+}) (see Fig. 5a). Meanwhile, metallic iron (Fe^0) is consistently observed at 710 eV BE indicating that the tribo-film thickness is no greater than 3.5 nm. The peak at 711.7 eV BE unambiguously confirms the presence of hydroxides on the surface.[10,11,12] The peak at 713.5 eV is a satellite peak of the Fe 2p core level and has no chemical meaning. After 0.25 min of etching, a sharp decrease of the hydroxide peak is observed correlated with an increase in the peak intensity of FeO and a decrease in the peak intensity of Fe_2O_3 (Fig. 4b-d). This result demonstrates that the hydroxide top layer is approximately 0.5 nm thick and is covering a layer of Fe_2O_3. The Fe_2O_3 itself is covering a layer of FeO/Fe_3O_4 near the metal surface and

the FeO/Fe_3O_4 layer is covering the steel substrate. After 3.5 min of etching, all characteristic iron XPS peaks remain in the spectrum, indicating that no clear sharp line separates each layer certainly because the layers have likely diffused into each other or have different thicknesses (Fig. 4c).

Apart from the evolution of the Fe 2p3/2 peaks with etching, the carbon content decreases continuously both inside and outside the wear scar (Fig. 4e). More interestingly in both cases, the carbon content is initially larger than 70% atomic percent decreases (37% inside, 8% outside). The high carbon content before sputtering is usually caused by adventitious carbon; in this case, however, the tribo-film contains a substantial amount of carbon because the high-resolution C_{1s} spectrum after 7/2 min sputtering shows only a small contribution content of oxidized species. Therefore, the C-C peak remains the major contribution along with the depth profile.

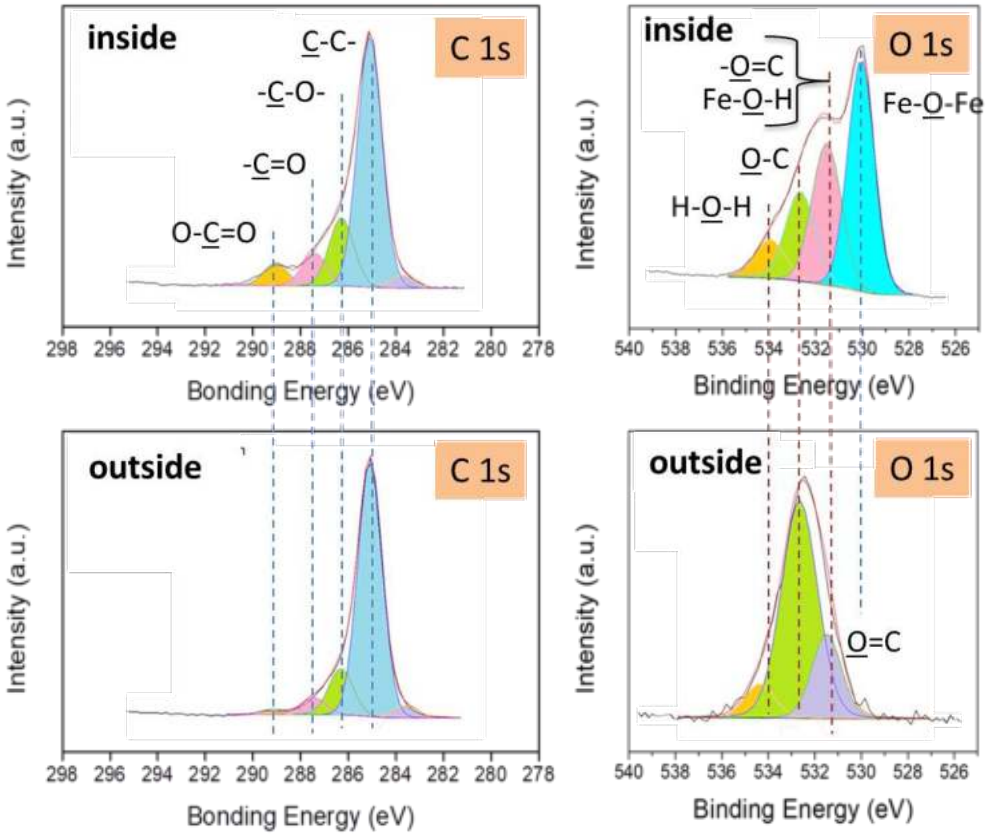

Fig. 5 XPS analysis of the ta-C flat (steel/DLC tribo-pair sliding in glycerol at 50°C, 3 mm/s. The regions inside and outside the wear scar are compared. Iron species were transferred from the steel substrate onto the ta-C surface during friction. The ta-C surface does not chemically react with glycerol.

In the case of the ta-C disk outside the wear track, the XPS spectrum shows two major contributions: O_{1s} and C_{1s}. However, the main difference between the spectra corresponding to inside and outside the wear track is the presence of the iron photopeaks Fe 3 s, Fe 3p, and Fe 2p inside the wear scar. Since no iron peaks can be detected outside the wear track and no iron exists in pure glycerol, the iron atoms inside the wear track originate from the counterpart, i.e. the steel ball. The core levels of oxygen inside and outside the wear scar on the ta-C flat are shown in Figure 5. The iron oxides bond (Fe-O-Fe at 530.0 eV BE) and iron hydroxide bond (Fe-O-H at 531.5 eV BE) are only detected inside the ta-C wear track. The C_{1s} carbon peaks comprise C-O and C=O peaks, and these peaks are more intense in the spectrum corresponding to inside the wear scar. The ketone moiety is not present in the glycerol molecule, it is certainly formed by oxidation and/or degradation during the wear process. The carboxylic group O-C=O is not present in the region outside the contact (Fig. 5); it was therefore formed by the tribochemical reaction on the steel side. These results give clear evidence that friction is responsible for the molecular degradation and oxidation of glycerol.

4.1.3. Discussions

This study compares the behavior of three different tribo-pairs: steel/steel, ta-C/ta-C, and steel/ta-C lubricated by glycerol at 50°C under the boundary regime (lambda ratio < 1 in all cases). Superlubricity (CoF less than 0.01) is achieved only with the steel/ta-C material combination.

Lubrication Mechanism. The initial steel/ta-C tribo-pair has a composite roughness of 19.9 nm, and the calculated EHL film thickness is 4.7 nm. The calculated initial maximum Hertzian contact pressure is 577 MPa, and the corresponding mean pressure is 382 MPa. Therefore, lubrication is dominated by interactions between asperities (the so-called boundary regime) so that initially, the role of the viscous fluid should be practically negligible. However, the steel surface becomes progressively more polished in the presence of glycerol and, because of chemical wear, the wear scar diameter increases to approximately 120 μm at the end of the test, compared with a theoretical Hertzian diameter of 100 μm under the initial static conditions. The increase of the surface conformity in the contact reduces the mean contact pressure from 382 MPa to 300 MPa and the surface roughness decreases to 4.3 nm, as

measured by AFM. The effect is a sharp decrease in the CoF to 0.004 within 0.03 h. Moreover, the polishing effect results in a lambda value slightly greater than 1.0, and the thin glycerol film will start carrying a substantial part of the load in the EHL regime.

If the average pressure is assumed to act over the entire contact disc, then the average viscosity according to Barus is 4.2 × 0.142 = 0.59 Pa.s. If a constant gap of 4.7 nm and a velocity difference of 3 mm/s is assumed, the shear rate is 6.4 e5 s^{-1}. Computing the shear force only inside the Hertzian contact (a = 52 μm) reveals that Ff = 3.2 mN; thus, a friction coefficient of 0.0011 is found. This low value does not account for shear forces outside the contact or for solid-solid interaction; hence, a slightly higher friction coefficient is to be expected. The experimental value of 0.004 is therefore in good agreement with the very thin film EHL regime at work. Interestingly, nearly the same superlow friction values were calculated for the two other cases (steel/steel and ta-C/ta-C pairs), polishing did not occur and the friction data in Figure 2 show that low friction is not sustained in these cases.

Such superlow values have already been obtained for highly polished steel/steel contact under rolling/sliding conditions, which are much less severe than pure sliding conditions. The film thickness was of the same order as ours[10]; in our case, however, the EHL regime was self-sustained in pure sliding. Notably, the literature includes several examples in which an increase in the wear scar diameter resulting from huge chemical wear at high speeds correlates with a drastic collapse of the contact pressure to a few tens of MPa. This situation effectively leads to friction values smaller than 0.01, which are classically explained by hydrodynamic lubrication; see, for example, ceramics in water.[13,14] Our results are different because the pressure does not collapse and the contact remains in the EHL and/or mixed regime at low speeds so that sample wear is very moderate and lubrication is suitable for practical use.

To investigate whether a fluid film plays a substantial role in achieving superlubricity, we used two different sliding speeds. The combination of 50°C and 3 mm/s gave a fluid film thickness of 4.7 nm and a theoretical CoF of 0.0011. The decrease of sliding speed (1 mm/s at 50 °C) results in a decrease in film thickness to 2.3 nm, which is substantially less than the composite roughness (19.9 nm); thus, severe boundary conditions occur and EHL conditions are not operating. The friction coefficient was measured as 0.01 on the Stribeck curve, which is a very low value for these conditions. This value can be compared with a theoretical CoF of approximately 0.001. This result shows that a suitable fluid film thickness is necessary to achieve superlubricity in this particular case. The CoF of approximately 0.01 under severe boundary conditions being not explained by EHL, another mechanism is at work.

Polishing mechanism. Because self-polishing represents one of the key roles in the low-friction process, we performed additional experiments by varying the test duration (by changing the friction pair with a new one for each test).

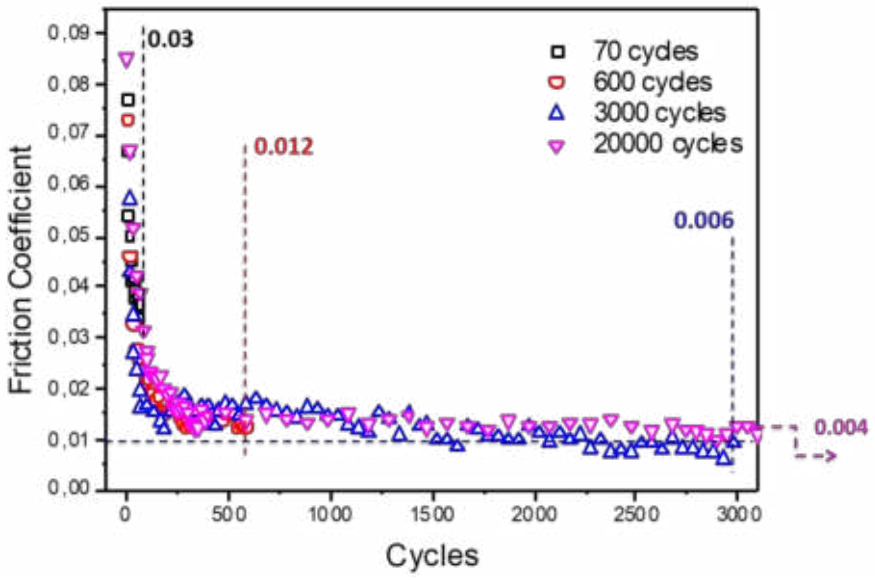

Fig. 6 Evolution of the friction coefficient against time for a steel/ta-C contact lubricated by glycerol at 50°C, speed 3 mm/s. Several tests were performed with various numbers of cycles (70, 600, 3000 and 20,000). Each test was run with new samples. All of the friction curves are practically superposed. Note that the 20,000 cycles test is not shown till the end for clarity.

Friction results are shown in Figure 6 for 70, 600, 3000 and 20,000 cycles, respectively. Note that the results of the 20,000 cycles test are not shown to the completion of the test to emphasize the beginning of the polishing mechanism. First, the different friction curves are well aligned with each other in a master curve, showing that the polishing mechanism is reproducible. The process shows three steps: From zero to 70 cycles, the CoF decreases from approximately 0.1 to 0.03. From 70 to 600 cycles, the CoF decreases until reaching a plateau at 0.015. Finally, from 1000 cycles to 20,000 cycles, the CoF decreases progressively to values less than 0.01.

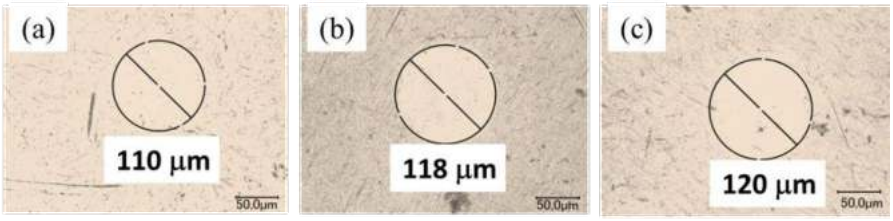

Nb cycles	70	600	3000	20000
Ra (nm)	19.7	12.1	8.05	4.30
CoF	0.03	0.012	0.006	0.004
Average pressure (MPa)	382	315	274	265

Fig. 7 Optical images of wear scars on steel balls corresponding to different numbers of cycles: (a) 600, (b) 3000, and (c) 20,000 cycles are demonstrated. The wear scar at 70 cycles was not visible; therefore, the mean pressure was that calculated based on Hertz theory. The polishing level is represented by the average roughness (Ra) determined by AFM as well as by the apparent contact pressure calculated from the scar diameter for each case.

The effect of polishing is hardly visible in the SEM image of the wear scar on the steel ball but it is visible on the optical image and roughness profiles measured by interferometry (Fig. 7). At fewer than 600 cycles, there is no wear of the ball and wear occurs between 600 and 3000 cycles although the wear volume remains very small. At the end of each test, the roughness was quantitatively measured inside the wear scar by AFM and the Ra values were compared with the average CoF values (see the table in Figure 7). At 70 cycles, the wear scar on the ball was not visible and we reported the Ra of the virgin steel surface outside the wear scar. The correlation between the Ra and the CoF is clear and the data show that friction diminishes with decreasing roughness. Figure 7 also shows the evolution of the mean contact pressure as a function of polishing. The pressure stabilizes at approximately 300 MPa not consistent with a hydrodynamic lubrication mechanism (often claimed by authors in similar papers on liquid superlubricity). These experiments demonstrate that polishing is closely linked to low roughness and therefore to low friction.

We subsequently investigated the mechanism of polishing in greater detail. An experiment was first performed to generate a rough surface with large wear scratches on the contact surfaces by sliding a self-mated steel tribo-pair in glycerol under 50°C at 3 mm/s. Afterward, a new friction test was carried out under the same conditions but with the steel flat replaced with a ta-C flat to investigate whether wear marks could be eliminated by polishing. In this

test, the steel ball was not changed to ensure that the contact area was located at the same location on the ball.

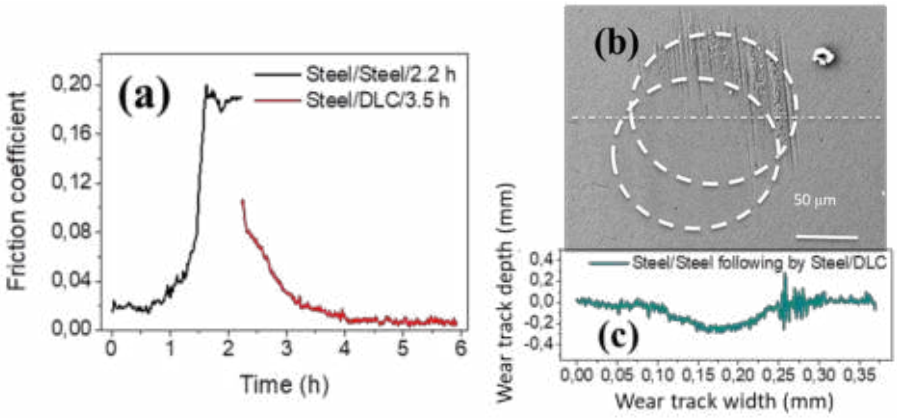

Fig. 8 (a) Friction coefficient as a function of test duration, as determined by first sliding steel against steel in glycerol for the first 2.2 h followed by sliding the same part of the steel ball on a ta-C disc in glycerol at 50°C and 3 mm/s. (b) SEM image of the wear track on the steel ball after the test; the images show the polishing mechanism and the two wear scars superimposed. (c) Corresponding depth profile in the wear track. Since wear is limited, the ball shape depth profile as Figure 2 (e) is not sufficiently clear to demonstrate the depth change after friction. The depth profile was standardized from ball to plane. Negative wear track depth values indicate missing material.

The results are shown in Figure 8. When a self-mated steel disk and ball are slid against each other, the friction coefficient increases from 0.02 to greater than 0.16, accompanied by the appearance of a large number of scratches on the surface (Fig. 2 a). When the steel disk is exchanged by a ta-C one, the friction coefficient first suddenly decreases to 0.11 and begins continuously to decrease until 0.004 after 4 h of testing, then remains stable thereafter. The SEM image in Figure 8 (b) shows the wear scars on the ball at the end. The 172 µm diameter wear track is partially covered with large scratches. A 115 µm diameter scar with very smooth surface is superimposed onto the previous one when the ta-C flat is used. Fortunately, the two wear scars are not exactly at the same place and they can be observed together. This clearly shows the occurrence of a polishing mechanism that increases the lambda ratio by decreasing the roughness.

Iron hydroxide formation. Our XPS results corresponding to the friction process show that iron oxides interact chemically with the glycerol molecules and that the reaction produces iron hydroxide on both the ball and the flat. A possible reaction is as follows (not equilibrated):

$$Fe_xO_y + C_3H_8O_3 \rightarrow Fe(OH)_z + Cs + H_2O$$

We propose here that this reaction produces iron oxyhydroxide like FeOOH (lepidocrocite), which is preferred to the hydrated form $Fe(OH)_3$ because of its 2-D lamellar structure in the contact configuration. The tribochemical reaction also generates carbon and water. Solid carbon and liquid water are preferentially formed rather than gases (carbon monoxide (CO) and hydrogen gases, for example) because of the antagonist effect of the high contact pressure which prevents gas formation in the tribochemical reaction (according to Le Châtelier's principle). This effect could explain why relatively high carbon content is found by XPS even after depth profiling inside the wear track. Moreover, the low friction generated by the OH-terminated groups was highlighted in the last decade. Recently, metal hydroxides have been reported to be the key factor to achieve the superlubricity of Nitinol/steel contact lubricated by castor oil. [15]

Accounting for all the necessary conditions to achieve superlubricity, a schematic representation of the interface is proposed (Fig. 9).

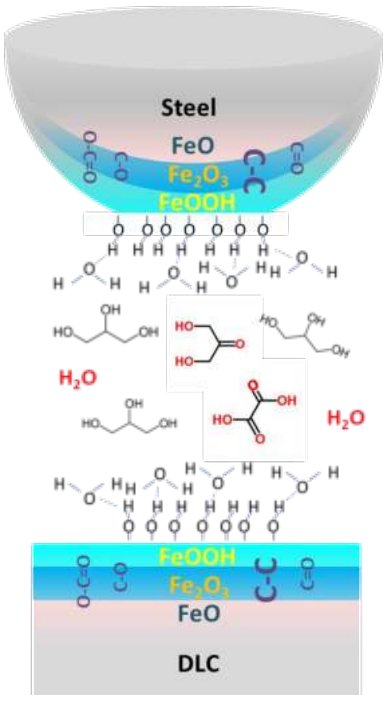

Fig. 9 Schematic of the superlubricity mechanism of a steel/ta-C tribo-pair in glycerol. The oxide surface is covered with iron hydroxide, giving OH termination, and a nanometre-thick fluid film ensures the EHL regime.

The steel ball achieves an extremely smooth polished surface inside the contact zone. On top of this polished surface, a FeOOH layer with a thickness of approximately 0.5 nm is generated by tribochemical reactions. Because of the hydrophilicity of FeOOH, water is absorbed onto the surfaces and forms a double-hydroxyl-terminated surface.[16] Between these double-water-terminated surfaces, a fluid layer composed of glycerol and possibly some of its main degradation products (e.g., water, dihydroxy-acetone, and hydroxyl-pyruvic acid) separates the contacting surfaces in the thin-film EHL regime.[17] The carbonyl and alcohol groups exist in all of the layers (FeOOH layer and iron oxides).

Carbon is also formed in the process and is found mixed with the surface species. This scheme emphasizes the three necessary conditions to achieve superlubricity: (i)gentle chemical polishing of the steel surface in the contact area, (ii) presence of a FeOOH layer and (iii) the presence of a thin and easily sheared EHL film. The fluid film provides superlubricity, and the hydroxide layer reduces friction during solid contact and also participates in chemical polishing, possibly resulting in slip at the wall. Once the superlow regime is reached, chemical wear stops, typically corresponding to a self-sustained process. During this step, the mean contact pressure has been reduced from 386 MPa to 300 MPa and remains stable for the whole test duration. Moreover, as shown by the MD simulations (Detailed in attached publication), the unique low-shear property of lamellar FeOOH can also take over, promoting lower friction (CoF of 0.01) when occasional solid contact occurs at very low speeds.

4.1.4. Conclusions

Through comparing the tribological performance of steel/steel, steel/ta-C, ta-C/ta-C in glycerol, chemical polishing of surfaces can be only observed for steel/ta-C, leading to superlubricity. Such surface polishing converts tribo-test from boundary lubrication to mixed lubrication (in our case, lambda is around 1). For this reason, the thin liquid film could partially support ch[illegible] and avoid massive contacts between asperities. Other than surface polishing, the formation of tribolayer containing both FeOOH and carbon species is certainly beneficial for mitigating friction between asperities. Combining surface polishing, surface functionalization, and thin liquid film lubrication, superlubricity is realized in this case.

4.2. In situ synthesis of graphene-nitride nanolayers on glycerol-lubricated Si_3N_4 surfaces leads to superlubricity

Accepted by ACS Appl. Nano Mater.

4.2.1. Experimental parts

Other than enabling the formation of metal hydroxide species on tribo-pair (see the previous chapter), the lubrication performance of glycerol strongly depends on the nature of tribo-pair. In this chapter, the tribo-chemical reaction between Si_3N_4 and glycerol is carefully investigated. The properties of the raw materials used are listed in table 1.

Table 1: Mechanical properties of materials.

	Suppliers	Production method	Diameter-mm	Elastic modulus-GPa	Poisson ratio
Si_3N_4 ball	CIMAP	Hot pressing	12.7	310	0.27
Si_3N_4 disk	LianYunGang HighBorn Technology	Hot pressing	-	310	0.27

This work highlights the impact of both temperature and sliding speed on tribological performances. More details are shown in table 2.

Table 2: Experimental conditions

Tribometer type	Reciprocating
Lubricant	Glycerol
Temperature	30 °C-150°C
Sliding speed	1.5-3 mm/s
Maximum Hertzian contact pressure	750 MPa

4.2.2. Results

Friction curves for Si_3N_4 balls sliding against Si_3N_4 disks show similar time evolutions for temperatures ranging from T = 30 to 120 °C (Fig. 1a). For all temperatures, the friction

coefficient is initially in the range 0.03 - 0.08 and converges towards $\mu \approx 0.01$ after a 1-hour running-in. Most strikingly, when T increases to 150 °C, μ decreases more rapidly and ends down at a significantly lower value of $\mu = 0.006 \pm 0.002$ characteristics of superlubricious sliding contacts, which is close to the detection limit of the friction force sensor.

Table 3: Properties of glycerol and elastohydrodynamic lubrication (EHL) film thickness calculations at different temperatures. The pressure-viscosity coefficient of glycerol at T = 120 and 150 °C is estimated by using that at T = 100 °C[3].

	Temperature T (°C)				
	30	50	80	120	150
Viscosity (10^{-3} Pa s)	645.8[18]	147.4[18]	31.8[18]	8.3[18]	3.8[18]
Pressure-viscosity coefficient (10^{-9} m² N^{-1})	5.9[3]	5.5[3]	5.4[3]	3.6	3.6
Ball wear scar diameter (μm)	101	98	115	165	222
Average Hertzian contact pressure after sliding (MPa)	387	411	299	145	80
Ball radius inside the wear scar (μm)	6.9	6.5	10.0	12.3	104
Surface roughness S_a of the ball after sliding (nm)	5.4	5.5	4.8	5.3	3.5
Surface roughness S_a of the disk after sliding (nm)	8.0	8.0	8.0	5.8	5.8
Composite surface roughness after sliding (nm)	9.7	9.7	9.3	7.9	6.8
EHL film thickness (nm)	12.5	4.3	1.9	0.8	1.8
Lambda ratio before sliding	1.19	0.43	0.15	0.06	0.03
Lambda ratio after sliding	1.28	0.44	0.20	0.10	0.26

For all temperatures, wear tracks on Si_3N_4 ball and disk are hardly visible by optical microscopy due to the poor contrast between inside and outside of the wear track. The wear depth on the Si_3N_4 disk is less than 30 nm for all temperatures (the case at 150 °C is shown in the inset of Fig. 1a). This correlates with a wear volume on the order of 10^4 μm^3 (Fig. 1b). For Si_3N_4 balls, the maximum wear loss detected at 150°C is 1.4×10^4 μm^3. Even though worn surfaces are polished after friction, and the ball wear scar diameter has enlarged compared to the initial Hertzian contact diameter, the lambda ratio (*i.e.*, the ratio of film thickness[4] to composite surface roughness) stays clearly below unity at T = 150 °C (Table 3). According to general rules in the lubrication regimes, this suggests that the observed superlubricity is not driven by bulk hydrodynamic or EHL fluid films and that tribochemical processes triggered by boundary lubrication are crucial.

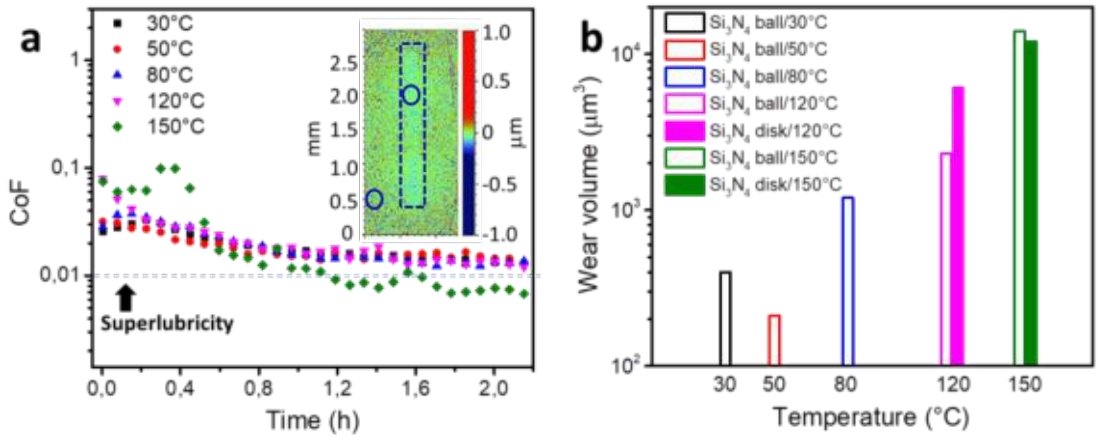

Fig. 1 Friction tests of self-mated Si_3N_4 boundary-lubricated with glycerol. (a) Friction curves and (b) wear volumes for the temperature range T = 30 - 150 °C. The inset in Panel a represents an interferometric image of the wear track (marked by a dashed rectangle) showing practically no wear. Ellipses indicate the probed areas for XPS analyses inside and outside the wear track.

A series of surface chemical analyses of the worn surfaces shed light on the reactions underlying the observed super-low boundary friction. Figures 2a and 2b show spectra obtained by X-ray photoelectron spectroscopy (XPS) carried out inside and outside the wear track on the Si_3N_4 disk at T = 150 °C. All spectra are calibrated by fixing the Si 2p photopeak of Si_3N_4 at a binding energy of 101.7 eV BE[19]. The C_{1s} XPS spectrum outside the wear track has one major peak at 285.2 eV BE and a broad shoulder at higher binding energies (Fig. 2b). The former is attributed to C−C or C−H bonds (accounting for 88% intensity), while the latter results from C−O, C=O and O−C=O bonds (small amounts of C−N and C=N bonds are also expected though). Inside the wear track, the main peak shifts from 285.2 to 284.8 eV BE and its width significantly increases (Fig. 2a). An additional peak at 284.5 eV BE is therefore needed, corresponding to C=C double bonds, providing evidence of the shear-induced formation of sp^2-hybridized carbon atoms (the carbon sp^2/sp^3 ratio is about 0.82). Intensities of other peaks for C−O/C−N, C=O/C=N and O−C=O/N−C=N bonds are nearly twice as high as those outside the wear track.

A comparison of the N 1s XPS spectra[20] performed inside (Fig. 2a) and outside (Fig. 2b) the wear track reveals the tribochemically-induced formation of N−C bonds as evidenced by the peak at 399.6 eV BE after sliding[21]. This peak is 10 times less intense than the Si_3N_4 surface peak (at 397.3 eV BE) and therefore the ratio of nitrogen-carbon to nitrogen-silicon bonds is

about 0.1. The nitrogen-carbon signal comes either from a carbon nitride surface layer or from carbon embedded in the Si_3N_4 matrix. However, in the second case, the N−C bonds should be accompanied by the presence of Si−C bonds, which are not detected by the XPS analysis. Therefore, most likely, a carbon nitride layer forms at the upmost surface of the wear scar. Since the Si_3N_4 substrate is visible in the XPS spectra, the thickness of the carbon nitride layer should be less than 4.4 nm.

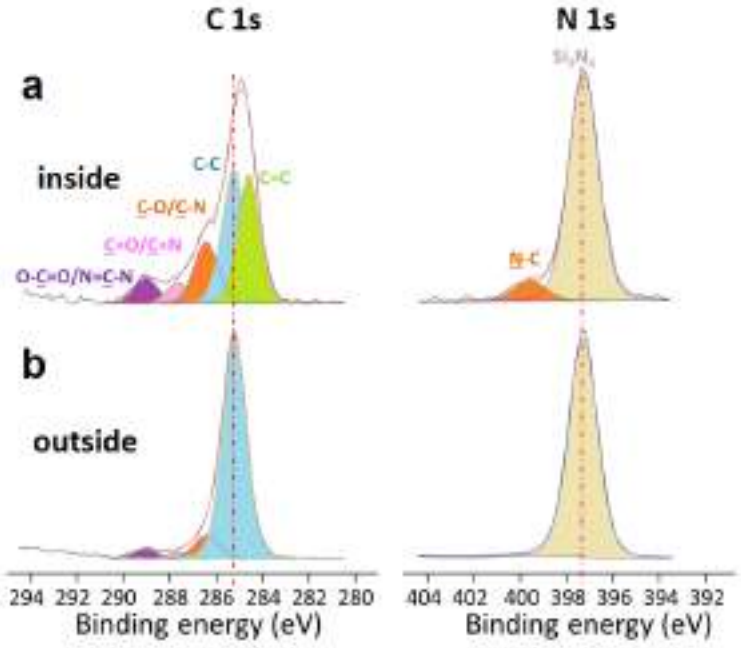

Fig. 2 C_{1s} and N_{1s} XPS spectra recorded inside (a) and outside (b) the wear track on the Si_3N_4 disk at T = 150 °C and friction coefficient μ = 0.004.

To better understand the chemical structure of this tribolayer and to quantify its thickness, high-resolution time-of-flight secondary ion mass spectrometry (ToF-SIMS) with a depth resolution of less than 1 nm is performed at the exactly same surface locations as in the XPS analyses. Figure 3a shows that the wear track emits mainly $Si_xO_yH_z$, C_xN_y and C_x negative ion clusters. C_xN_y and C_x ions are more abundant in smoother areas (visible in the optical image) while the $Si_xO_yH_z$ signal is more localised in scratches, near the edges and even outside the track. Figure 3b displays the intensities of various C_xN_y species present in the spectrum, where CN, C_3N and C_2N_3 signals are the most intense. These C_xN_y fragments are emitted rather evenly from the wear track, while SiN, SiCN and OH are most intense at the turning point of the ball (Fig. 3b).

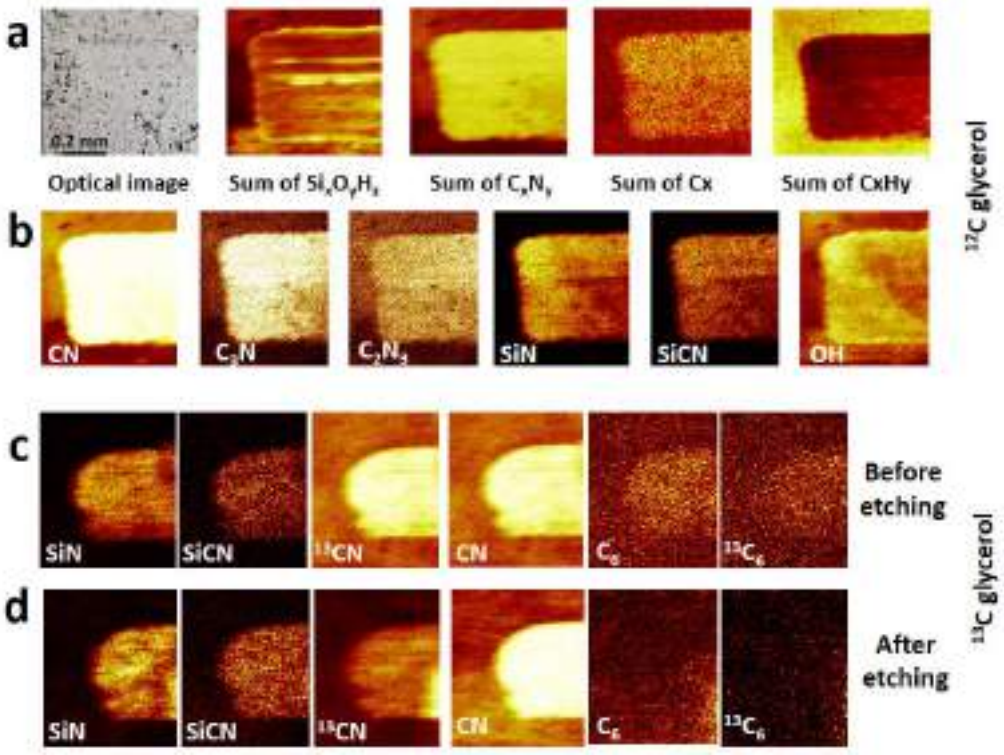

Fig. 3 ToF-SIMS chemical maps obtained at the turning point of the Si_3N_4 disk wear track. (a) Selected ToF-SIMS chemical maps for ^{12}C-glycerol lubrication. The corresponding optical image is shown for comparison. (b) ToF-SIMS chemical maps of C_xN_y, Si species and OH in detail. (c,d) ToF-SIMS chemical maps of Si_3N_4 disk wear track with ^{13}C-glycerol lubrication (wear track was generated with the same parameters, tribological behaviour is consistent with that shown in Fig. 1) before (c) and after etching (d).

The origin of the C_xN_y fragments is identified by an additional sliding experiment at T=150 °C using ^{13}C-labeled glycerol. The experiment with ^{13}C glycerol yields comparable friction behaviour and ToF-SIMS intensities as for ^{12}C glycerol. ToF-SIMS chemical analyses are performed before and after ion-etching of the topmost layer of the worn surface. A comparison of the ToF-SIMS maps before (Fig. 3c) and after ion etching (Fig. 3d) reveals that the intensities of the CN, SiN and SiCN maps remain essentially the same whereas the intensity of the ^{13}CN map significantly decreases after etching. The ^{13}CN, $^{13}C_6$ and C_6 intensities almost vanish after etching. Because the estimated etching depth varies between 0.1 and 1 nm, depending on the material, this suggests that the carbon nitride layers have probably a planar and possibly disordered 2D structure.

The nature of the chemical bonding of C_xN_y is further elucidated by high-resolution Orbitrap mass spectroscopy of used ^{13}C glycerol collected after sliding. In the used lubricant, the ion $^{13}C_4H_7N_2^+$ (containing an aromatic C_3N_2 ring) at m/z 87.0737 is detected (Fig. 4a), while virgin ^{13}C glycerol shows no peak at this m/z. Another peak at m/z 132.0752 indicates the presence of C_4N rings (Fig. 4b). Since such heterocyclic C_xN_y species were not detected in brass-glycerol-steel sliding contacts[22], we conclude that tribochemical reactions of glycerol with Si_3N_4 surfaces are likely to produce these cyclic carbon nitrides. In summary, the combination of our XPS, ToF-SIMS, and Orbitrap MS analyses strongly suggest that sub-nanometer-thick carbon nitride layers are made of graphenoid structures form at the very top of Si_3N_4 surfaces during sliding under glycerol lubrication.

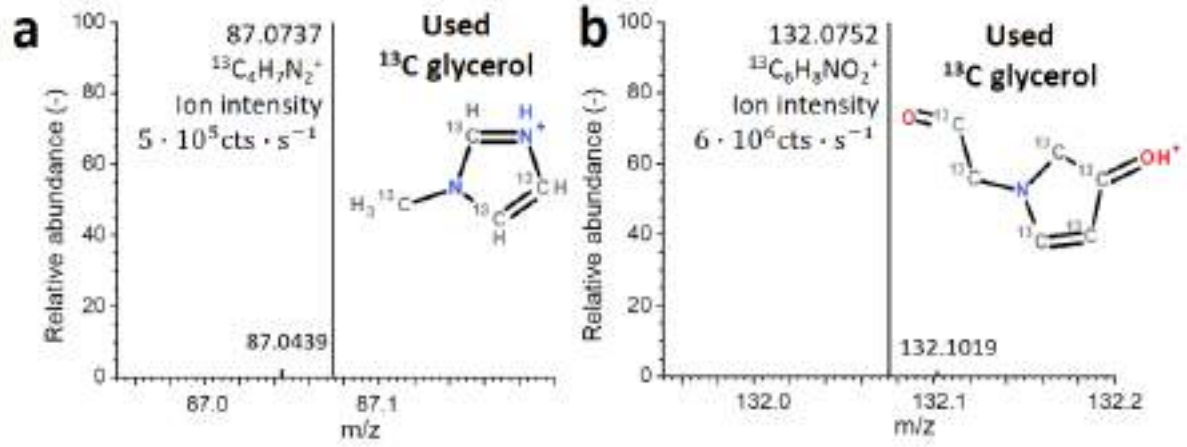

Fig. 4 High-resolution mass spectra of used ^{13}C glycerol in positive ion mode obtained by Orbitrap MS. The inset in Panel a and b displays the ions $^{13}C_4H_7N_2^+$ and $^{13}C_6H_8NO_2^+$ with measured mass/charge (m/z) ratios of m/z 87.0737 and m/z 132.0752, which deviate by 7.4 ppm and 3.3 ppm from calculated m/z 87.0743 and m/z 132.0756, respectively. The intensities 5×10^5 and 6×10^6 (counts s^{-1}) of m/z 87.0737 and m/z 132.0752, respectively, indicate a high abundance of these ions in the used ^{13}C glycerol lubricant.

Influence of sliding speed change The same friction test has been conducted at 150°C except sliding speed fixed at 1.5 mm/s. This speed drop induces a sudden rise of CoF. In 2.2 h, CoF fluctuates at around 0.225 (Fig.5a). Such CoF variation tendency is completely different from the one at 3 mm/s where superlubricity can be easily achieved (Fig.1a). Furthermore, unlike

the test of 3 mm/s, low sliding speed generates a homogenous and ultra-smooth wear scar on the Si_3N_4 ball. Dark particles are now visible on Si_3N_4 ball wear scar (Fig. 5b) that sharply increases local roughness to 30.2 nm (Fig. 5c) and deep grooves are also detected by the interferometer. It's noteworthy that the test performed at 1.5 mm/s leaves a smaller wear diameter (155 μm) than the test conducted at 3 mm/s and its wear volume is less. However, considering the difference between sliding distance at 1.5 mm/s and 3 mm/s, wear rate per meter is more suitable to evaluate wear. So at 1.5 mm/s, the wear rate is 416.3 $\mu m^3/m$ while the wear rate of 3 mm/s test is 590.4 $\mu m^3/m$.

In fact, at 1.5 mm/s, the calculated film thickness at the end of the test is 0.5 nm which has no physical meaning because this value is lower than the molecular size of glycerol – 0.6 nm [23]. It is questionable if glycerol molecules can still enter into a contact to lubricate surfaces under these circumstances. Even if some glycerol molecules are inside of contact, their quantities may not be sufficient to avoid the adhesive wear between Si_3N_4 tribo-pair and to provide enough CN species to protect lubricating surfaces.

In brief, the speed at 3 mm/s is more preferable than 1.5 mm/s and the occurrence of low friction is accompanied with the generation of ultra-smooth Si_3N_4 wear.

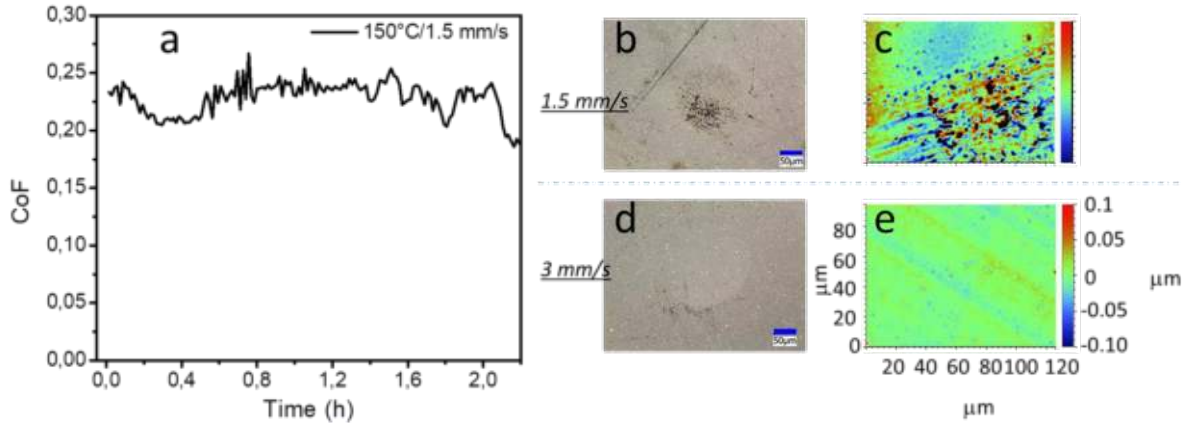

Fig. 5 a Friction curve of self-mated Si_3N_4 sliding in glycerol at 150°C and 1.5 mm/s. The optical image and 3D depth information of wear on Si_3N_4 ball are demonstrated in **b** and **c**, respectively. For comparison, optical image and 3D depth information of wear on Si_3N_4 ball at 150 °C and 3 mm/s are exhibited in **d** and **e**. In these figures, the scale bars of optical images are 50 μm and 3D depth images share the same scale.

Durability tests

To probe lubrication performance of glycerol in long duration tests and check if carbon nitride layers are also formed in other temperature, a sliding test at 120°C was prolonged till 7h. Interestingly, superlubricity was reached under 120°C but once sliding test is prolonged to 7 h. At the end of test, CoF is recorded as 0.009 (Fig. 6a). However, this long term sliding increases wear scar diameter on Si_3N_4 from 150 μm to 200 μm (Fig. 6b,c). This results in a drop of average Hertzian contact pressure from 176 to 99 MPa (Table 4). Moreover, the roughness of wear scar is further polished to 3.1 nm. Considering all those changes, lambda ratio increases up to 0.4, again in the boundary regime (film thickness 2.6 nm).

Table 4: Wear comparison of tests lasting 2.2h and 7h at 120°C.

	Duration (h)	
	2.2	7
CoF	0.011	0.009
Wear diameter (μm)	150	200
Average Hertzian contact pressure after sliding (MPa)	176	99
Ball roughness S_a (nm)	5.3	3.1
Ball radius inside the wear scar (mm)	11.0	43.5
EHL film thickness (nm)	1.1	2.6
Lambda ratio after sliding	0.1	0.4

We obtained similar XPS results in Si_3N_4 wear scar at 150°C compared with 2.2h sliding at 120°C. the major C_{1s} peak of Si_3N_4 wear at 120°C shifts to lower binding energy and its width is broadened inside wear scar (Fig. 6e,f,g). We needed to add a C=C bond contribution to fit these spectra correctly. Moreover, after sliding the N-C bond, the N 1s peak becomes visible. Most interestingly, both C=C and N-C bonds are more pronounced after 7h sliding comparing with test stopping at 2.2h.

This long-duration test reveals that the CN_x species present in Si_3N_4 cannot prevent wear scar from growing larger at 120°C as sliding time goes on. The reason is that at temperatures of 120°C or 150°C, the viscosity of glycerol is too small to establish a complete EHL film and separate contacts between asperities. Facilitated by glycerol, local contacts of Si_3N_4 asperities lead to the generating of CN_x species. Simulation results show that the aromatic CN ring is generated along with sliding and it owns excellent lubricity. When Si_3N_4 serves as raw

material to produce CN_x species, its anti-wear property is questionable since shearing may lead to detachment of CN species from Si_3N_4 and to compensate for the loss of CN species, more Si_3N_4 is worn. A similar case has been observed when silica is added to the solution to limit wear[24] but when sliding Si_3N_4 in water to generate silica layer, low friction can only be observed when average contact pressure drops down to 10 MPa or less, which corresponds to a wear diameter around 1000 μm[25,5].

Besides the formation of CN_x species on wear scar, surface polishing and average contact pressure drop should also be highlighted for reaching superlubricity. After a 7h sliding test at 120°C, sliding leads to an increase of lambda, which results in a relatively less severe condition. Simultaneously, from XPS, both C=C and N-C signal increase when the test is stopped at 2.2h. It is strongly possible that surface polishing and average contact pressure drop influence friction by impacting the content of CN_x species on Si_3N_4.

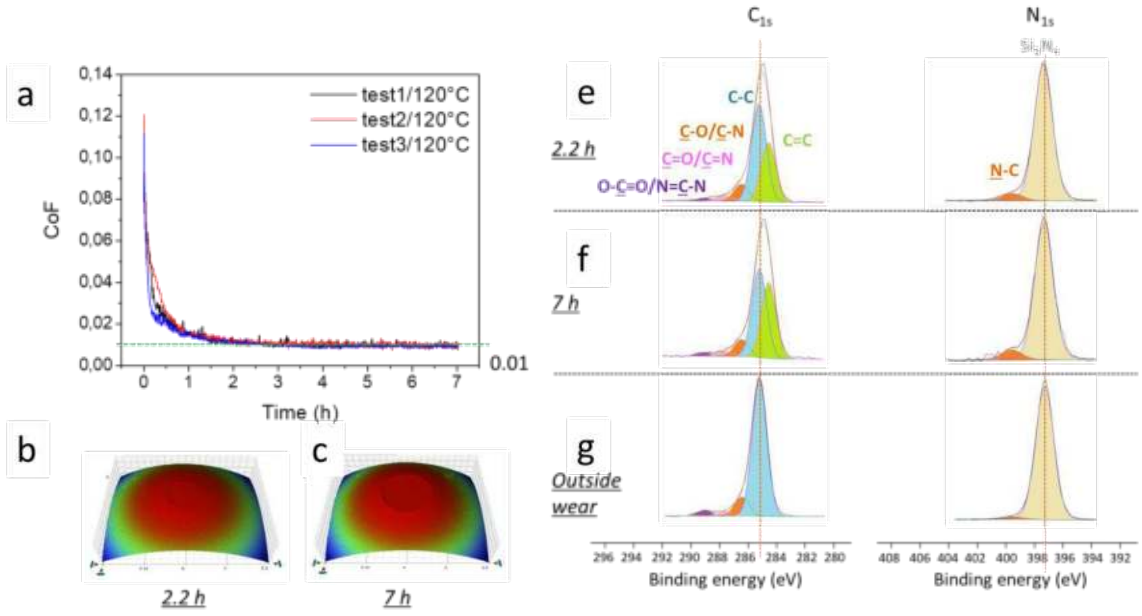

Fig. 6 a Friction curve of sliding test lasting 7h at 120°C. Topographical images around Si_3N_4 ball wear scars whose test last: **b** 2.2 h, **c** 7h. XPS of Si_3N_4 disk whose test stops at: **e** 2.2 h, **f** 7h. **g** XPS from parts outside Si_3N_4 disk wear scar.

4.2.3. Discussions

So far, superlubricity of Si_3N_4 in water has been associated with the formation of easy sheared hydrodynamic film or nanoscopic water layers between hydrophilic colloidal silica. Silica gel tribofilms was formed during tribochemical reactions of water with Si_3N_4. Conversely, the

superlubricity phenomenon presented here is not thought to rely on silica formation and water film lubrication but instead is achieved through the *in situ* synthesis of self-lubricating 2D graphene-nitrides nanolayers. Under 150°C, glycerol isn't able to adsorb water from the environment and 17% percent mass loss has been recorded for used glycerol comparing with its original mass. This means that not only water but also glycerol evaporates at this temperature.

The actual superlubricity mechanism can be obtained through a suitable choice of lubricant and loading conditions. For instance, using water solutions with low pH mixed with glycerol results in superlubricity by silica-water layers, while the use of pure glycerol reduces the formation of surface silicon oxide and has the potential to trigger superlubricity by graphene-nitrides. Interestingly, the graphene-superlubricity reported in this work has been achieved under much more severe boundary lubrication conditions (i.e. $v_{\max} = 3$ mm/s and $\lambda \ll 1$, see Table 3) than in previous studies[26,27] on silica-water-layer superlubricity. Under these conditions, bulk hydrodynamic lubrication by glycerol is not favoured and the tribochemical synthesis of graphene-nitrides is promoted by large contact pressure and shear stress at the asperity contacts. However, under more moderate lubrication conditions, glycerol can form a hydrodynamic film between two sliding surfaces[27]. In the absence of asperities (atomically flat surfaces) the glycerol nano-film in the contact would be almost iso-viscous because of the increase of the contact radius inside the wear scar (corresponding to a significant decrease in the contact pressure) and the low viscosity pressure coefficient of glycerol. In these conditions, the CoF is always below 10^{-4} (Fig. 7) for film thickness not below 4 nm, however. This demonstrates that contacts between asperities are mainly responsible for the experimental friction value of 0.006. Low friction is accompanied by a generation of ultra-smooth Si_3N_4 surface with roughness as low as 3.5 nm. Therefore, the graphene-superlubricity and polishing effect between glycerol and Si_3N_4 reported in this article are certainly beneficial for engineering applications that operate under extreme lubrication conditions including mechanical seals, roller bearings, and piston rings.

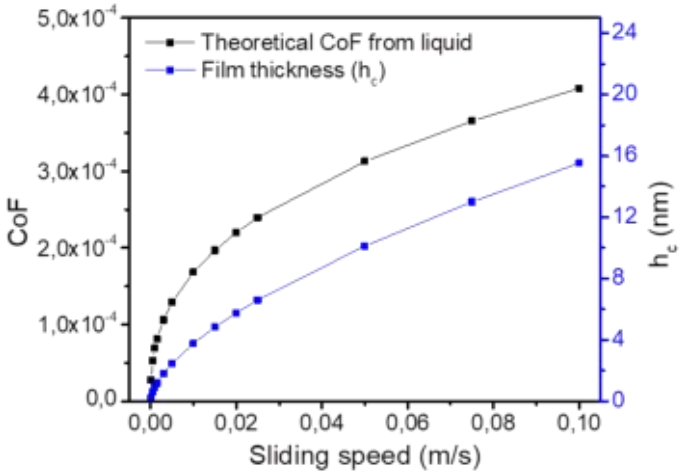

Fig. 7 Theoretical CoF originated from shearing glycerol at T = 150 °C on the function of speed. The corresponded film thickness is marked in blue. Theoretical CoF of liquid is calculated by the ratio of tangential force and normal force (Couette film flow). Here, tangential force is written as $\eta_0 e^{\alpha P} Au/h_c$. P and A are apparent pressure and area in contact, which are 80 MPa and 3.8×10^4 μm^2 at T = 150 °C. Below the film thickness of about 4 nm, the theory is not valid because the viscosity cannot be defined any longer.

4.2.4. Conclusions

This study unveils that in situ synthesis of sub-nanometer-thick graphene-nitride layers establishes a superlubricity regime for Si_3N_4 under boundary lubrication with glycerol. To achieve this, in addition to the tribochemical decomposition of the lubricant to form carbon-rich tribolayers, the involvement of surface N atoms is essential for promoting aromatization, and thus passivation, of the topmost surface layer. The aromatic graphene compound alone can support high contact pressures and helps to form a superlubricious interface under severe boundary lubrication conditions. This study paves the way for the utilization of in situ tribochemical synthesis of graphenoid compounds on silicon-based ceramics to achieve green superlubricity. Moreover, it stimulates further research that considers the use of other bio-lubricants and investigates the lubrication conditions that make the structure of the aromatic tribolayers controllable and their formation on other ceramic interfaces (e.g., dry Si_3N_4/a-CN_x) possible. This work is further confirmed by computer simulations. For more details, please check the publication attached.

4.3. Superlubricity induced by long-term sliding of steel/SiC in glycerol

4.3.1. Experimental parts

The universality is always important to scrutinize for a lubricant since lubricant sometimes has its application limitation. For instance, under high sliding speed, pure water can help Si_3N_4 tribopairs to reach superlubricity due to high corrosive wear and the drastic collapse of contact pressure but when it lubricates Al_2O_3, ZrO_2, CoF is generally above 0.2[28]. Here, the steel ball is used to slide against polycrystalline SiC in glycerol at low sliding speed to reach superlubricity under boundary conditions

Table 1: Mechanical properties of materials.

	Suppliers	Production method	Diameter-mm	Elastic modulus-GPa	Poisson ratio	Hardness - GPa
Steel ball	Total	-	200	210	0.3	8.3
SiC disk	LianYunGang HighBorn Technology	Hot pressing	-	410	0.18	24.5

Before starting the description of experimental conditions, it is important to highlight that SiC disk is manufactured by hot pressing, contains some impurities and has certain porosity. Diameters of these holes vary from 30 nm to 200 nm while most of the voids have diameters around 50 nm (Fig. 1c). Optically, those holes turn to be black (Fig. 1b) and they show strong signals of D, D' and G peaks by Raman spectroscopy, which are located at 1346 cm^{-1}, 1590 $cm^{-1,}$ and 1612 cm^{-1}, respectively. D, G peaks represent the disordered structure and sp^2 carbon networks in graphitic materials while D' peak arises from the interaction between graphitic material's extended phonon modes and impurities' vibrational modes. D+G peak around 2900 cm^{-1} also stands for defects in graphitic material. Furthermore, a 2D peak can be observed around 2664 cm^{-1}, which is known as the overtone of the D band[29]. As for those grey and flat parts in Fig. 1b, their Raman spectra are shown in the next section.

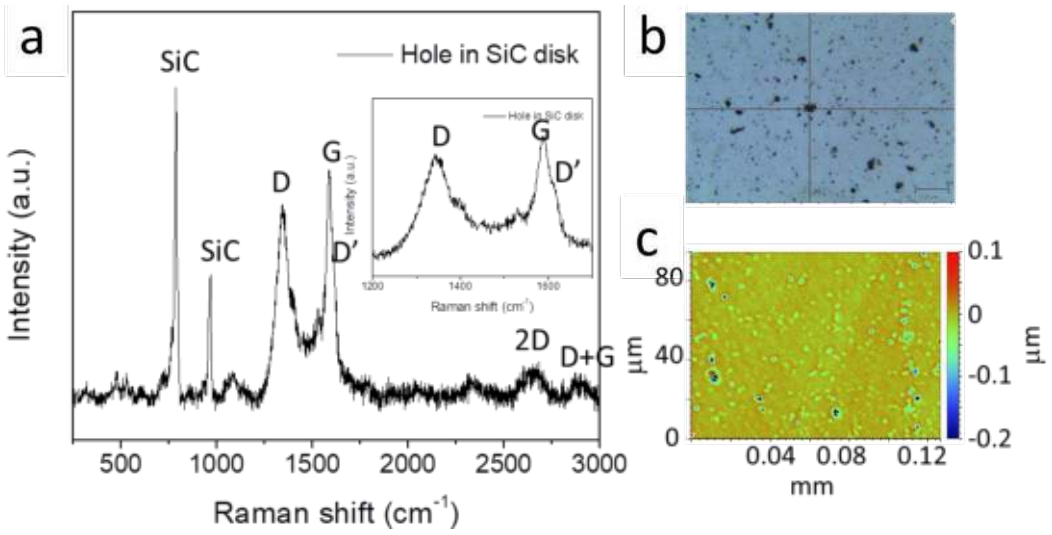

Fig. 1 a Raman spectrum of a hole in SiC disk surface, the inset image is enlarged image from 1200-1700 cm^{-1} **b** optical image of SiC disk by Raman with an objective of 50x, the cross point of two lines is the point analyzed in Fig. 1a **c** 3D depth information of SiC surface.

Experimental conditions are presented in Table 2:

Table 2: Experimental conditions

Tribometer type	Reciprocating
Lubricant	Glycerol
Temperature	50, 80, 120 °C
Sliding speed	3 mm/s
Maximum Hertzian contact pressure	598 MPa

4.3.2. Results

The tribological performance of steel/SiC in glycerol is highly dependent on the ambient temperature. The test at 50°C exhibits the lowest initial CoF of 0.05 while CoF of 0.14 and 0.07 are recorded for tests carried out at 120°C and 80°C, respectively (Fig. 2a). After sliding for 1.9 h, only tests performed at 50°C and 80°C are capable to finish with CoF less than 0.02. Concerning the test at 120°C after a transient CoF decrease during the first 0.15 h, it experiences a continuous CoF increase up to 0.12. At 1.9 h, CoF terminates at around 0.11 which is 5 times higher than for the two other temperatures. Unfortunately, after 1.9 h sliding, none of them can finish in the superlubricity regime. With respect to the wear scars, wear diameter on steel balls follow a monotone increase with temperature. For instance, the

wear diameter at 50°C is 132 µm while wear diameters at 80°C and 120°C are 162 and 210 µm, (Fig. 2c-e), respectively. Consequently, the test at 50°C has the highest average contact pressure around 146 MPa. On the other side, even though wear scar on SiC disk is observed for tests at 80°C, 120°C (Fig. 2f-g) thanks to the wear debris accumulating on the stroke edges, no material gaining or missing is detected at 50°C or 80°C by interferometry while around 10 nm of SiC is removed from the surface at 120°C (Fig. 2b).

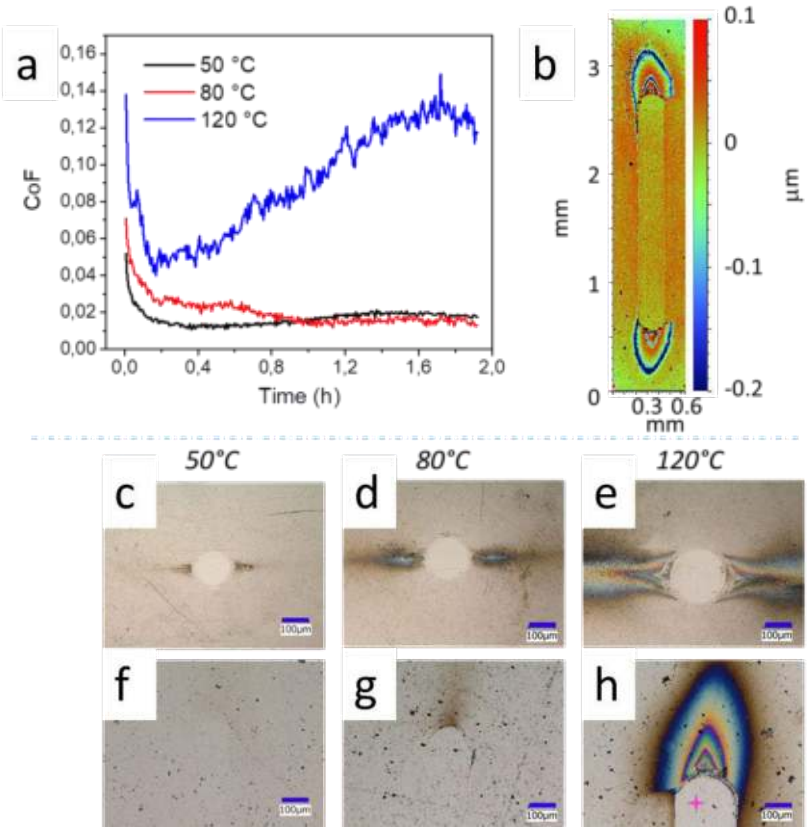

Fig. 2 a Friction curve of steel/SiC friction pairs sliding in glycerol under different temperatures, all tests stop at 1.9 h **b** 3D profile of SiC disk after friction under 120°C. Optical images of steel ball and SiC disk after sliding at **c**,**f** 50°C **d**,**g** 80°C **e**,**h** 120°C. Pink star is where the Raman spectrum has been performed.

We ran a long duration test at 50°C up to 7.4 h and superlubricity occurred after 4.3 h sliding. (Fig. 3a). Afterward, CoF continuously decreased after setting foot in superlubricity. At 7.4 h, the final CoF is 0.007. Regarding the wear scar on a steel ball and comparing to the test stopped at 1.9 h, wear scar diameter slightly increases from 132 µm to 151 µm (Table 3). This means that average contact pressure decreases from 146 MPa to 112 MPa. More surprisingly, the radius of curvature inside the wear scar also augments from 12.7 mm (ball radius of wear

when the test stopped at 1.9 h) to 16.4 mm. Consequently, the calculated liquid film thickness also rises from 5.0 nm to 5.9 nm. Cooperating continuous polishing of wear scar, final lambda is recorded as 0.4 at the end of the test. Bearing in fact that the test stops at 1.9 h, the lambda ratio is 0.29. Lubrication conditions become less severe with long-term sliding but still stay in the boundary regime. On the other side, long term sliding leads to some accumulation of wear debris at the edges of the stroke (Fig. 3c). Thanks to that, wear scar is easier to locate for performing Raman and XPS inside the track.

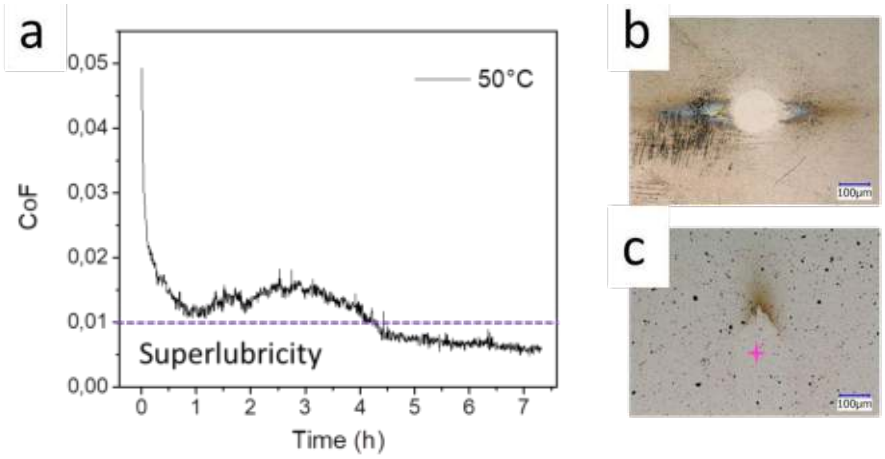

Fig. 3 a Long term friction curve @ 50°C up to 7.3 h. Optical images of wear scars on **b** steel **c** SiC. The pink cross is where the Raman spectrum has been taken.

Table 3: Comparison of lubrication state and wear scars dimensions at 1.9 h and 7.3 h @50 °C.

Time -h	1.9		7.3	
CoF	0.018		0.007	
	Ball	Disk	Ball	Disk
Wear diameter -mm	132		151	
Average contact pressure -MPa	146		112	
Radius of curvature in the wear scar -mm	12.7		16.4	
Roughness (Sa) –nm	15.9	7.0	12.7	7.3
EHL film thickness (nm)	5.0		5.9	
Lambda ratio	0.29		0.40	

First of all, the Raman spectra of flat parts on the SiC surface were obtained at 50°C and 120°C. In both cases, typical peaks of SiC are observed at 787 and 968 cm^{-1}corresponding to

transverse optical (TO) and longitudinal optical (LO) mode of SiC (Fig. 4). At 120°C, LO mode is more pronounced with a comparison with outside wear scar while test at 50°C exhibits similar TO, LO ratio to Raman taken from outside the wear scar. The biggest difference between tests done at 50°C and others is the presence of D, D', G peaks. They share the same position as Raman spectra taken in holes of SiC (Fig. 1a). This strongly suggests that graphitic materials are extracted from SiC holes that are smeared on SiC wear scar. It is worthy to mention here that superlubricity is only detected for the test done at 50°C. The CoF of the test performed at 120°C is 0.11, much higher. No difference has been recorded on the steel side by Raman between inside wear scar and outside.

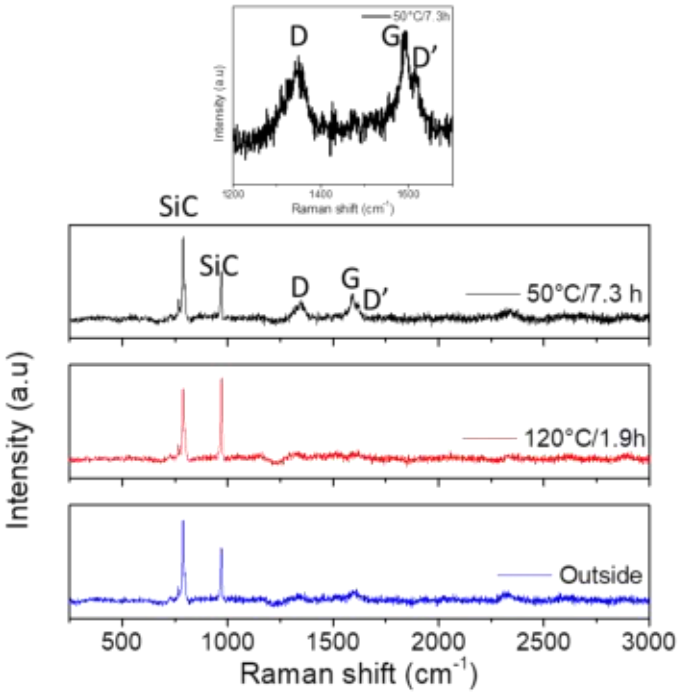

Fig. 4 Raman spectrum of SiC disk on flat parts after 7.3 h of sliding @ 50°C, after 1.9 h sliding at 120°C and outside of wear track. The inset image shows details from 1200-1700 cm^{-1} in the spectrum for the case @50°C.

Because Raman is not surface sensitive, XPS is preferred here to confirm the components of the outmost layer on the SiC disk. XPS spectra are calibrated by fixing the Si2p in SiC at 100.3 eV BE[19]. After sliding and for both tests performed at 50°C and 120°C, iron was detected on SiC but the element content is less than 1% atomic. All spectra are dominated by C_{1s} peak but regarding test performed at 50°C, the C_{1s} signal is mainly composed of C-C and C-Si bonds are detected for the test performed at 120°C (Fig. 5). The binding energy of C_{1s}

peak @ 50°C case is located at 284.7 eV however it is shifted to 285.1 eV at 120°C case. Such a shift of bonding energy corresponds to an increase of the C=C bond on the top surface. Combining Raman and XPS analyses, the origin of C=C is likely to originate from the presence of graphitic material on virgin SiC top surface. Other than the C=C bond, other oxygenated species of C are more pronounced for the test at 50°C.

The XPS Si 2p peak obtained on virgin SiC before sliding shows that more than half of its intensity comes from oxidized species, namely SiO_2 and O-Si-C[30] located at 103.1 and 100.7 eV respectively. Nevertheless, their contents significantly decrease after sliding the SiC disk at 120°C so that more than 90% of the signal comes from SiC. On the contrary, the quantities of SiO_2 and O-Si-C augment after sliding the SiC disk at 50°C. These findings indicate that sliding SiC disk in glycerol at low temperature favours silicon oxidation but if the same test is conducted at a higher temperature, the silicon oxidation layer will be removed.

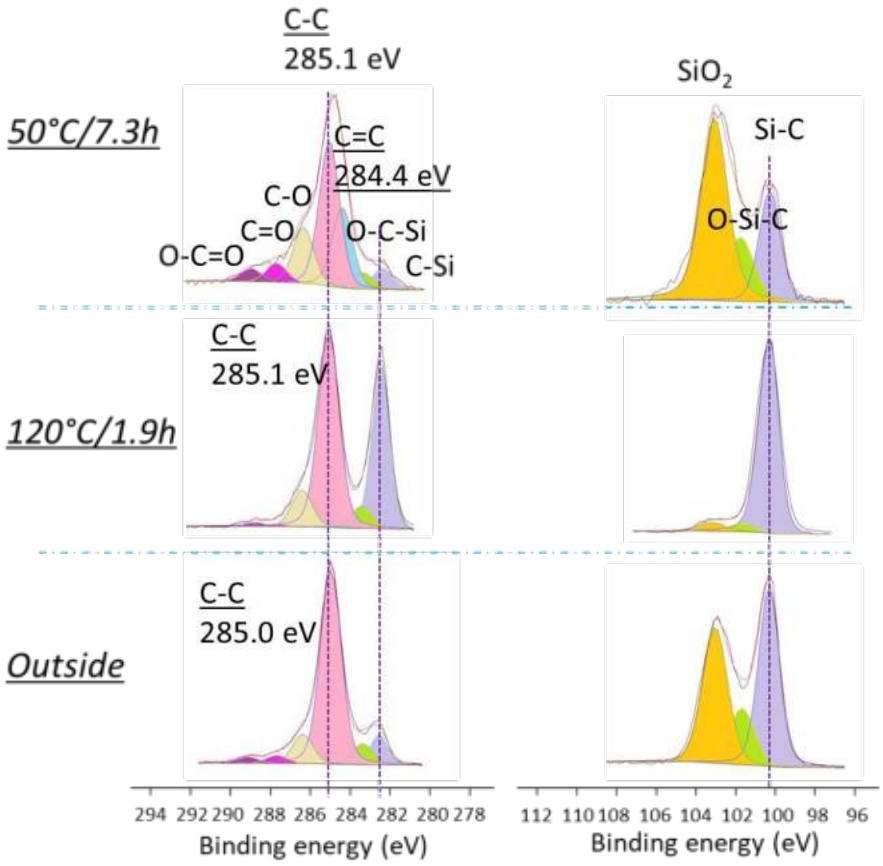

Fig. 5 XPS of SiC disk from upside to the bottom: after 7.3h of sliding at 50°C, after 1.9h sliding at 120°C and outside of wear track. C_{1s} peaks are listed on the left side while Si_{2p} peaks are presented on the right side.

Table 4: Fitting details of XPS on SiC disk.

50°C/7.3 h	C_{1s}							Si_{2p}		
Percentage-%	50.2							14.4		
Peaks	C-Si	O-C-Si	C=C	C-C	C-O	C=O	O=C-O	Si-C	O-Si-C	SiO_2
Positions-eV	282.4	283.3	284.4	285.1	286.4	287.7	289.0	100.3	101.8	103.1
FWHM-eV	1.2	1.2	1.2	1.2	1.2	1.2	1.2	1.3	1.6	1.6
Percentage-%	3.0	2.4	11.6	20.6	7.9	2.8	1.9	3.7	2.7	8.0
120°C/1.9 h	C_{1s}							Si_{2p}		
Percentage-%	60.0							25.5		
Peaks	C-Si	O-C-Si	C=C	C-C	C-O	C=O	O=C-O	Si-C	O-Si-C	SiO_2
Positions-eV	282.4	283.4	-	285.1	286.4	287.7	288.8	100.3	101.7	103.1
FWHM-eV	1.05	1.2	-	1.2	1.2	1.2	1.2	1.3	1.5	1.5
Percentage-%	21.0	3.2	-	29.5	5.3	0.4	0.6	23.2	1.1	1.2
Outside	C_{1s}							Si_{2p}		
Percentage-%	53.8							14.9		
Peaks	C-Si	O-C-Si	C=C	C-C	C-O	C=O	O=C-O	Si-C	O-Si-C	SiO_2
Positions-eV	282.5	283.4	-	285.0	286.4	287.7	289.1	100.3	101.7	103.1
FWHM-eV	1.05	1.2	-	1.2	1.2	1.2	1.2	1.3	1.5	1.5
Percentage-%	4.8	3.8	-	37.2	5.3	1.5	1.2	6.7	2.3	5.9

On the steel ball side, the XPS spectrum is calibrated by fixing the FeO_x O_{1s} peak to 530.0 eV. Sliding steel ball in glycerol always results in a slight increase of C_{1s} and a small decrease of the O_{1s} peak. Element content changes and depends on the temperature but change remains within 10% (Table 5). Comparing outside and inside of wear, the increase of C_{1s} signal is mainly due to contributions of C-O, C=O, O-C=O bonds (Fig. 6). It indicates that glycerol reacts with steel surfaces during shear and glycerol or its fragments are absorbed on steel. On the other side, the decrease of O_{1s} signal mainly comes from FeO_x. At the same time, the FeOH signal at 531.4 eV increases by 1.6 or 2.1% after friction, this depending on temperature. We can conclude that FeO_x reacts with glycerol and produces FeOH on the top surface[31].

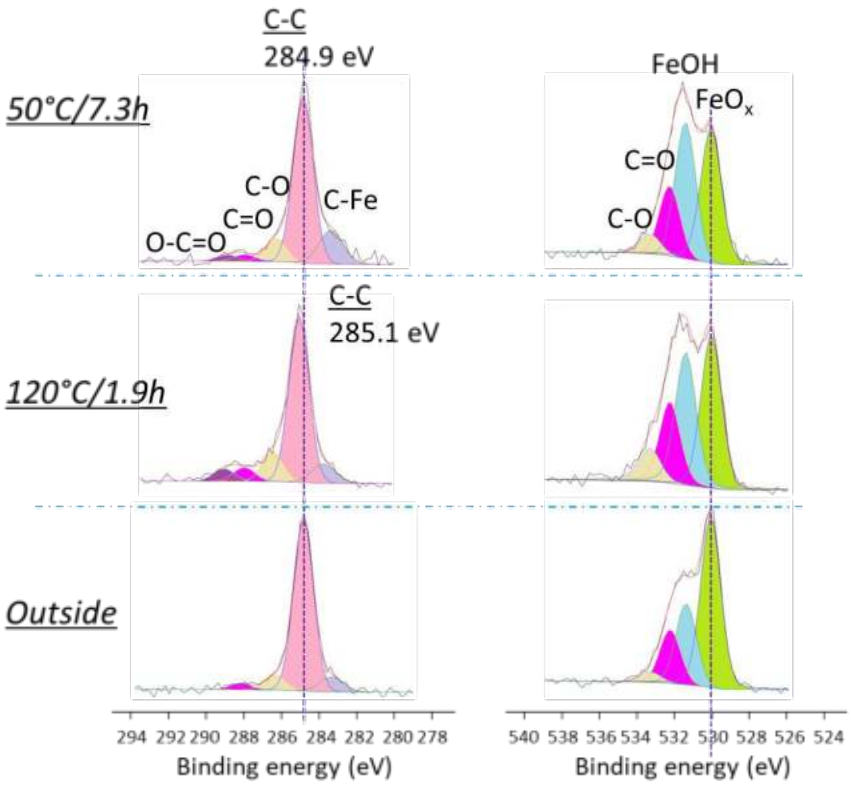

Fig. 6 XPS of steel ball from upside to the bottom: after 7.3h of sliding at 50°C, after 1.9h sliding at 120°C and outside of wear track. C_{1s} peaks are listed on the left side while Si_{2p} peaks are presented on the right side.

Table 5: Fitting details of XPS on steel ball.

Steel/50°C/7.3 h	C_{1s}					O_{1s}			
Percentage-%	65.5					29.3			
Peaks	C-Fe	C-C	C-O	C=O	O=C-O	FeO_x	FeOH	O=C	O-C
Positions-eV	283.4	284.9	286.4	288.0	288.9	530.0	531.4	532.2	533.3
FWHM-eV	1.5	1.3	1.3	1.3	1.3	1.3	1.3	1.3	1.3
Percentage-%	10.9	44.5	6.5	1.9	1.7	11.6	10.7	5.5	1.5
Steel/120°C/1.9 h	C_{1s}					O_{1s}			
Percentage-%	60.5					33.2			
Peaks	C-Fe	C-C	C-O	C=O	O=C-O	FeO_x	FeOH	O=C	O-C
Positions-eV	283.8	285.1	286.5	288.0	289.1	530.0	531.4	532.2	533.3
FWHM-eV	1.5	1.3	1.3	1.3	1.3	1.3	1.3	1.3	1.3
Percentage-%	5.6	40.7	7.5	3.5	3.2	12.3	11.2	6.9	2.8
Steel outside	C_{1s}					O_{1s}			
Percentage-%	56.1					36.2			

Peaks	C-Fe	C-C	C-O	C=O	O=C-O	FeO_x	FeOH	O=C	O-C
Positions-eV	283.4	284.9	286.4	288.0	-	530.0	531.4	532.2	533.3
FWHM-eV	1.5	1.3	1.3	1.3	-	1.3	1.3	1.3	1.3
Percentage-%	4.8	45.8	3.9	1.6		20.0	9.1	6.0	1.1

4.3.3. Discussions

To understand the origin of superlubricity in this case, it is important to confirm if some asperities are in real contact (without liquid). At 50°C after 7.3 h of sliding, the lambda ratio is calculated as 0.4. It is noteworthy that the steel ball is not truncated to a flat surface by friction but a curved one (Fig.7). As for the test carried out at 120°C, even though CoF is above 0.1, the steel surface is also polished down to Ra= 13.6 nm. Taking into account the corresponding changes of curvature radius inside the contact zone and film thickness as 41.6 mm and 2.0 nm, respectively, the final lambda ratio is 0.13. Additionally, the theoretical calculation of the Couette friction coefficient of glycerol liquid film at 50°C after 7.3 h of sliding is 0.0012 and its value at 120°C is 0.0002. Combining the fact that (i) lambda value is always below unity and (i) the huge difference between theoretical CoF of the liquid film and measured CoF, it can be concluded that many asperities are in contact and they serve as the cause of friction rise at both temperatures 50°C and 120°C.

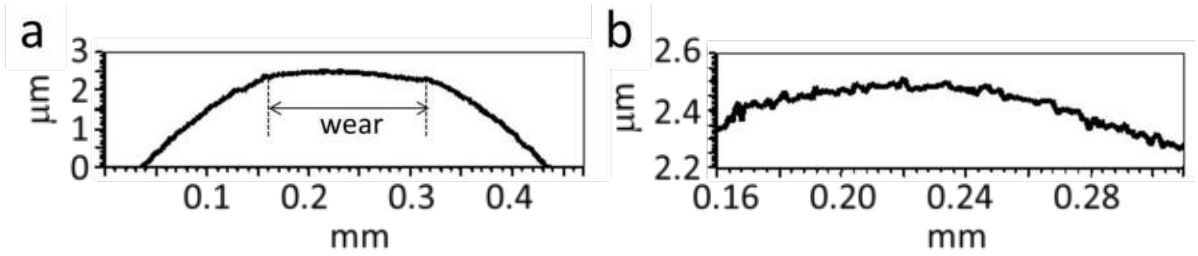

Fig. 7 a Topography of steel ball after 7.3 h sliding at 50°C, where curvature radius outside wear scar is 6.35 mm **b** wear scar topography corresponding wear part in Fig. 7a. Here, the curvature radius is 16.4 mm.

Even though asperities are in contact in both tests done at 50°C and 120°C, the surface chemistry varies with temperature. From Raman and XPS analyses, the major difference is detected on the SiC disk. At 50°C, both graphitic materials and silica layers are detected but at 120°C, no graphitic material is observed by Raman, and no C=C bond is observed by XPS in wear scar. Moreover, the signal from silica becomes extremely weak. The presence of the

silica layer is crucial to decrease friction since the silica layer boosts the hydrophilicity of SiC[32] and helps to grow a hydrogen-bonded network of glycerol and water layer on SiC[27].

In pure water, a low friction state for Si_3N_4 and SiC is always reached when average contact pressure is reduced to around 10 MPa[25,33] even though a silica layer is presented on the surface. In our case, a hydrogen-bonded network of glycerol is expected to form on silica layer and could bear the load. Nevertheless, a full hydrogen-bonded network gives a CoF of 0.03[34] by simulation and it requires cooperation with acid or to grow an easy shearwater layer [6] on it to reach superlubricity. Our tests are conducted under RH 25% which is lower than critical humidity for glycerol to absorb enough water.

Other than the water layer, graphitic materials exhibit excellent lubricity thanks to its incommensurate structure[35]. Moreover, under boundary lubrication, the hydrogen-bonded network is probably not able to completely block asperities in contact[36]. The presence of graphitic materials could ease this concern[37,38]. Moreover, those graphitic materials are more expected to be present on asperities than covering the whole SiC surface because a surface fully covered by graphitic material is supposed to have dominant C=C content over C-C by XPS.

Briefly, the superlubricity of steel/SiC in glycerol is believed to be established by the cooperation of both the hydrogen-bonded network and graphitic materials to bear the load and provide low friction (Fig. 8). Surface polishing of steel also helps to decrease the severity of lubrication.

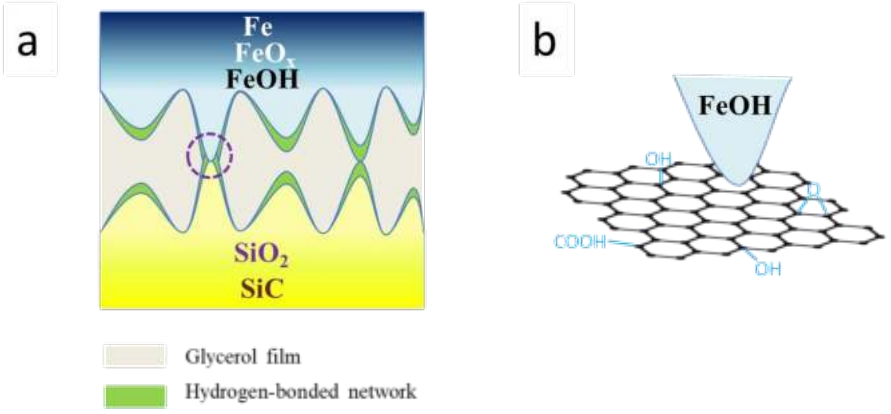

Fig. 8 a Schematic picture of the superlubricity mechanism of steel/SiC in glycerol. It's worthy to mention that glycerol film contains also a hydrogen-bonded network, the green parts correspond to the

hydrogen-bonded network directly linked to the surface. **b** contacts between asperities at the nanoscale for those penetrating the hydrogen-bonded network.

4.3.4. Conclusions

Superlubricity has been demonstrated by sliding steel/SiC in glycerol at 50°C but long-term sliding is necessary to reach the regime. This superlubricity is enabled by the formation of a silica layer and graphitic materials on the SiC surface. An increase of temperature up to 120°C removes both silica layer and graphitic materials so that the superlubricity regime is lost and friction increases. This work provides guidance to develop new superlubricity systems by glycerol with ceramics containing some graphitic materials.

4.4. Superlubricity enabled by antiviral – hypericin

4.4.1. Experimental parts

Materials Hypericin is bought from MedChem Express with a purity > 98%. It derives from an herb named St. John's wort[39] and is used as an active constituent of medicine to treat anti-depressants[40], deficit hyperactivity disorder[41], and even cancer[42]. Structurally, it is constituted by 6 carbon folded rings with CH_3, OH, O bonding on molecular edge (Fig. 1b).

Interests Since it contains only C, H, O, no additional disposal process is required compared with conventional oil additive- MoDTC, ZnDTP. Moreover, because hypericin can be extracted from plants of hypericum, the low cost of preparation opens the possibility to widely apply in industry. In the end, its fancy structure offers a high content of sp^2 carbon, which could passivate the surface in contact[43].

Friction tests Paralleled experiments are conducted under the same experimental conditions as sliding steel ball against SiC disk in glycerol (see the previous chapter). The only difference is that 0.3 wt% hypericin (h) is added to glycerol and well mixed at 0°C. After mixing, glycerol turns from transparent into black color (Fig 1a). However, when the mixture is taken by pipette, it appears to be dark violet.

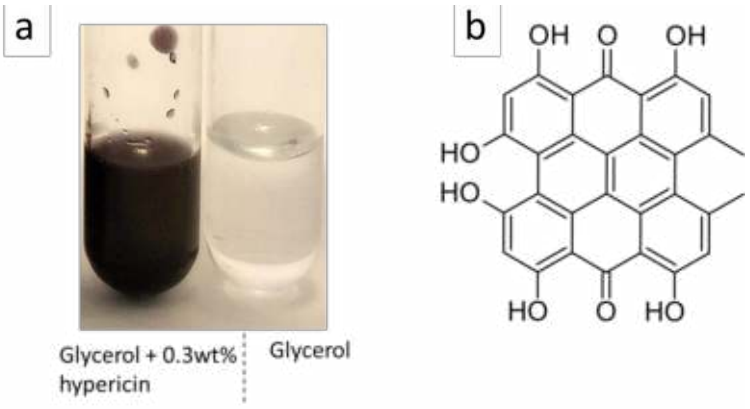

Fig.1 a Optical image of glycerol and glycerol-hypericin mixture b molecular structure of hypericin.

4.4.2. Friction results

For steel/SiC lubricated by glycerol, adding hypericin in glycerol doesn't change the initial CoF (Fig. 2 a,b). But after 1.9h of sliding, the final CoF is reduced at the 3 temperatures.

Concerning the scar diameter and wear volume, the impact of hypericin in glycerol is negligible. Strikingly, at 50°C with the help of hypericin, long-term sliding (as mentioned in the last chapter) is no longer necessary for steel/SiC to reach superlubricity. After sliding for 1.6 h, a test with hypericin shows the superlubricity regime (Fig. 2b). With hypericin in glycerol, steel surfaces turn rough and black that is different from the case of pure glycerol where steel surfaces are polished. As shown in Fig. 4a, Sa is measured as 32.3 nm. Moreover, wear scar on SiC disk becomes optically visible thanks to the wear debris accumulation on stroke edges, thus helping the location of following surface analyses. At 80°C, the final CoF is further reduced to 0.007 comparing with 50°C case in the glycerol-hypericin mixture. However, a further rise of temperature to 120°C leads to an increase of CoF to 0.04 together with an increase of wear on steel (Fig. 3 d-f) and the absence of black substance.

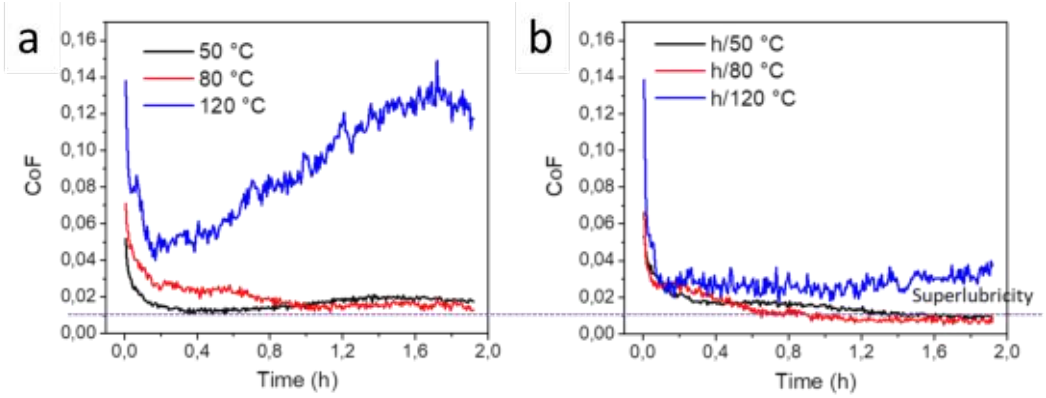

Fig. 2 Friction curves at different temperatures by sliding steel/SiC in **a** pure glycerol **b** glycerol-hypericin mixture. It is worthy to mention that the experiments shown here are conducted under the light in the room.

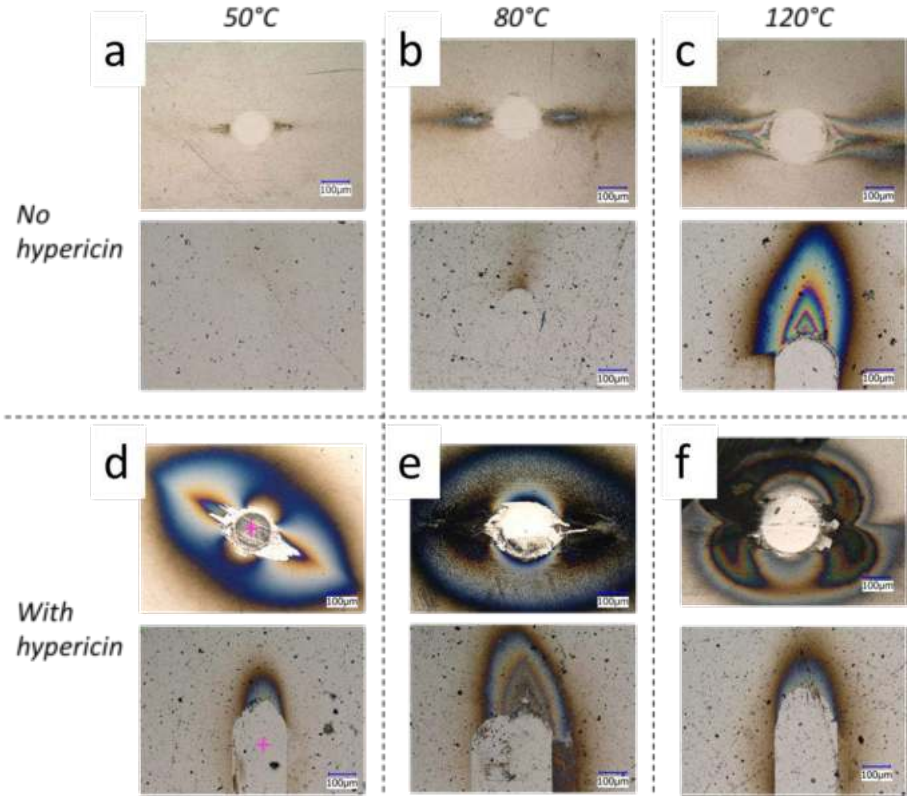

Fig. 3 Optical images of steel (upside) and SiC (bottom) wear scars after glycerol lubrication at: **a** 50°C, **b** 80°C, **c** 120°C. Optical images of steel (upside) and SiC (bottom) wear scars after glycerol-hypericin mixture lubrication at: **d** 50°C, **e** 80°C **f** 120°C.

In the following, we focus on characterizing steel wear scar in the test at 50°C. As shown in Fig. 4a, steel wear is abundant of bumps with heights up to 100 nm, and most of the bulges own heights around 50 nm. EDS analyses show that this wear scar is covered by carbon (Fig. 4b,c) and the same finding is observed for the colorful film outside of wear. The carbon content inside wear is measured as about 30 wt%, while virgin steel shows a carbon content around 3 wt%. A Raman spectrum was taken inside the steel, wear scar exhibits similar features like the spectrum of pure hypericin sample. Typically, peaks at around 440 and 490 cm^{-1} stand for skeletal deformation of hypericin, peaks at 1245, 1310, 1366 cm^{-1} represent C-C in-plane stretching mode, and peaks between 1545 and 1589 cm^{-1} correspond to ring stretching with C=O. The peak at around 1613 cm^{-1} originates from C=O stretching[44]. Furthermore, a 2D peak known as an overtone of D peak[29] is observed at 2627 cm^{-1}. Despite their qualitative similarity, the components ratio of C-C in-plane stretching has been modified after friction, the ratios between peaks at 440 cm^{-1} and 1310 cm^{-1} show a decrease inside wear compared with virgin hypericin. All those changes indicate that the hypericin molecule structure has been slightly altered after the friction test.

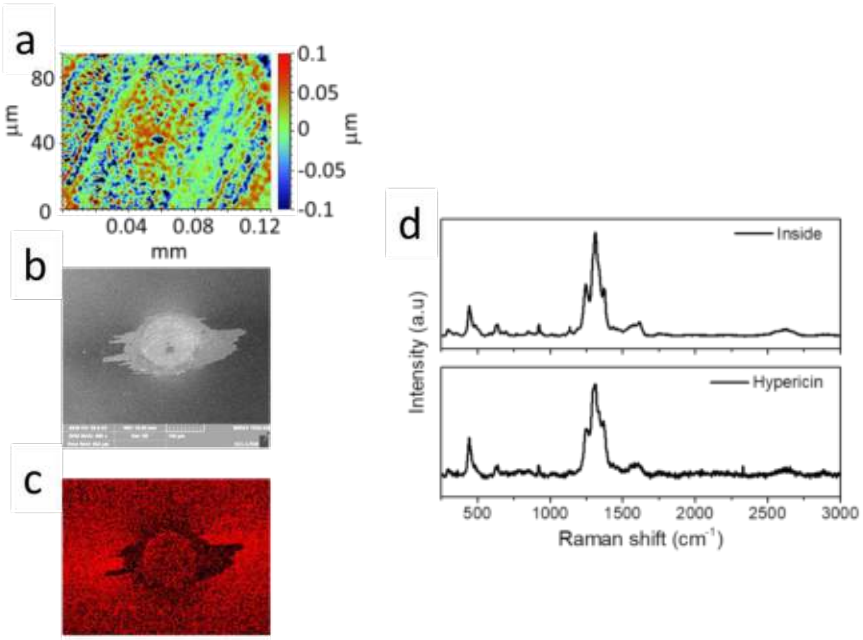

Fig. 4 a 3D profile **b** SEM image **c** C element EDS map of steel wear scar at 50°C. **d** Raman spectrum taken inside of steel wear at 50°C. The original hypericin spectrum is listed below for comparison.

To check whether hypericin or its derivatives adsorb on steel surface, XPS was performed. All spectra are calibrated by shifting C_{1s} main peak to 284.8 eV BE, as usual. Inside of steel wear scar at 50°C only C_{1s} and O_{1s} peaks are detected (not iron) (Table 1). This confirms that the steel worn surface is fully covered by hypericin or its derivatives. Comparing with virgin hypericin, the steel wear surface shows an increase of 5.4% carbon content, and C-C/C=C bond is more pronounced after friction. Correspondingly, O_{1s} content decreases with respect to virgin hypericin, mainly due to the decrease of C-O species (Fig. 5). Additionally, pi to pi* transition is detected at 290.5 eV BE in both spectra (hypericin and wear scar). This peak is commonly detected for structures containing carbon folded rings[45,46]. On the other hand, the position of O=C bond in the O_{1s} spectrum is detected at 531.5 eV BE, suggesting that oxygen is directly bonded to the carbon ring since aliphatic O=C is located at around 532.2 eV BE[10]. In general, after friction, the carbon ring is present in the steel wear scar and this hypericin derivative has less oxygen than the additive molecule.

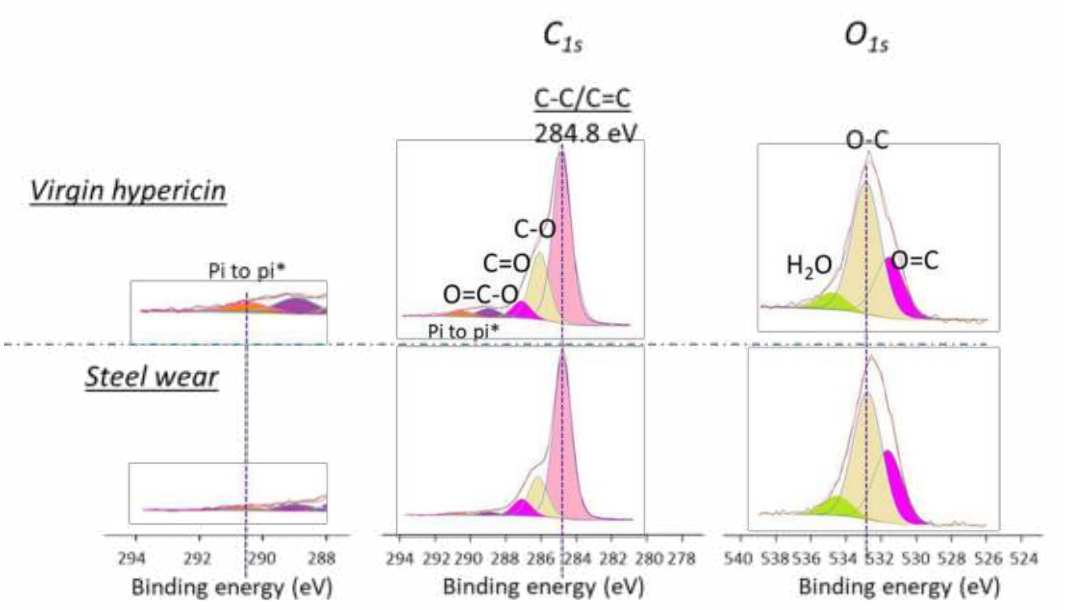

Fig. 5 C_{1s} and O_{1s} peak of virgin hypericin (upside), steel wear at 50°C (bottom) obtained by XPS. The image on the left side is the amplification image of C_{1s} from 288 to 294 eV.

Table 1: Fitting detail of C_{1s} and O_{1s} peak of Fig.5.

Virgin hypericin	C_{1s}					O_{1s}		
Percentage-%	78.9					21.1		
Peak	C-C/C=C	C-O	C=O	O=C-O	pi to pi*	O=C	O-C	H_2O
Position-eV	284.8	286.1	287.1	289.0	290.5	531.5	532.8	534.8
FWHM-eV	1.2	1.3	1.3	1.5	1.5	1.9	1.9	1.9
Percentage-%	49.0	19.6	5.1	3.1	2.1	6.1	13.3	1.7
Steel wear at 50°C	C_{1s}					O_{1s}		
Percentage-%	84.3					15.7		
Peak	C-C	C-O	C=O	O=C-O	pi to pi*	O=C	O-C	H_2O
Position-eV	284.8	286.1	287.1	289.0	290.5	531.5	532.8	534.8
FWHM-eV	1.2	1.3	1.3	1.5	1.5	1.9	1.9	1.9
Percentage-%	57.6	14.6	8.3	2.5	1.3	5.2	9.1	1.4

At the opposite of steel, no hypericin signal is detected by Raman in SiC wear scar, only transverse optical and longitudinal optical mode of SiC are detected at 787 and 968 cm^{-1}

respectively (Fig. 6a). Because the depth resolution of Raman is around 1 μm and can not determine if hypericin or its derivative is on the topmost 10 nm surface, XPS is employed. All spectra are calibrated by shifting the Si 2p peak of SiC at 100.3 eV BE[47]. XPS results show that inside the wear scar, the carbon content is 67 %, which is much larger than its content outside the wear scar (18%) (Table 2). This significant increase stems majorly from the contribution of a new carbon peak C=C located at 284.4 eV BE on the left of the C-C peak peaking at 285.3 eV BE (Fig. 6b). Meanwhile, the oxidized species of carbon (C-O, C=O, O-C=O) also become more pronounced compared with outside wear. For instance, the C-O content of inside SiC wear is 10% while its content outside SiC wear is only 5.3%. Most importantly, after friction, the pi-pi* transition is present in the wear scar at 291.0 eV BE. Combining the fact that C=C and pi-pi* are both detected inside SiC wear, it can be concluded that species with carbon folded rings have been tribochemically formed. On the other hand, SiO_2 and O-Si-C bonds are still observed after friction at 103.1 eV and 101.7 eV BE but their content is low.

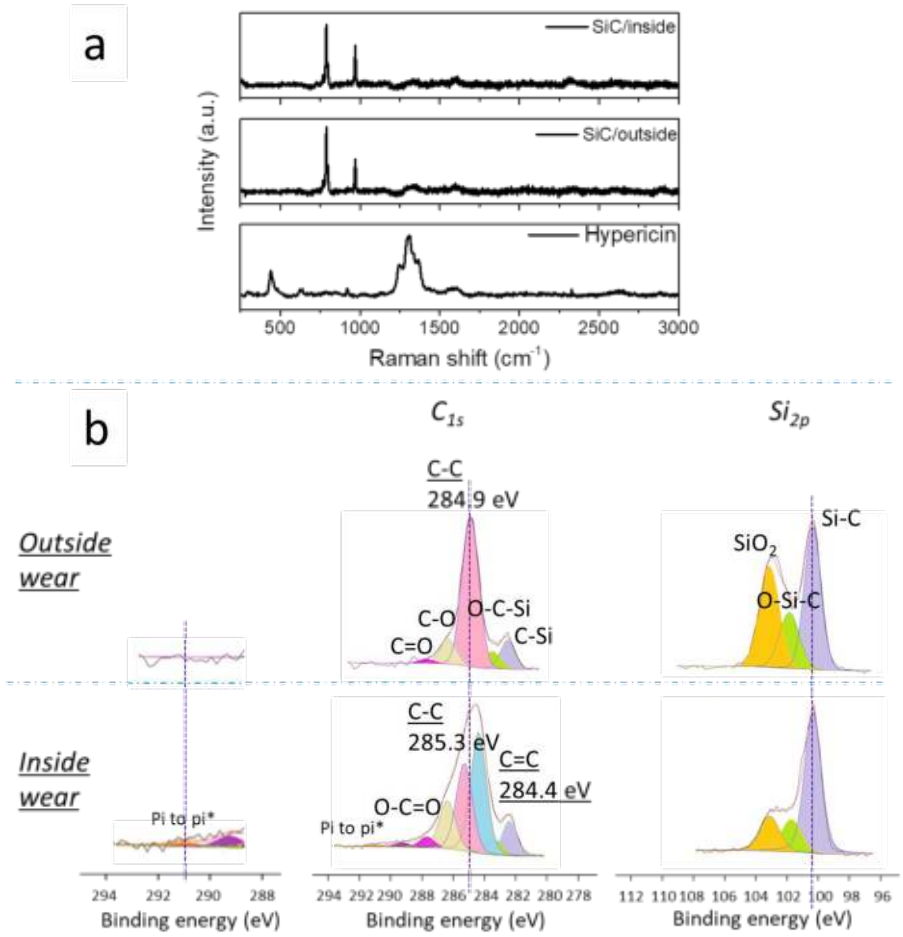

Fig. 6 a Raman spectra taken inside and outside of SiC wear at 50°C. **b** XPS C_{1s} and Si 2p photopeaks taken from outside SiC wear scar (upside) and inside SiC wear at 50°C (bottom). Spectrum on the left side shows C_{1s} from 288 eV to 294 eV BE.

Table 2: Fitting details of C_{1s} and Si_{2p} peak of Fig. 6b.

SiC 50°C outside	C_{1s}								Si_{2p}		
Percentage-%	48.8								16.8		
Peak	C-Si	O-C-Si	C=C	C-C	C-O	C=O	O-C=O	pi-pi*	Si-C	O-Si-C	SiO_2
Position-eV	282.5	283.5	-	284.9	286.3	287.7	-	-	100.3	100.8	103.1
FWHM-eV	1.1	1.2	-	1.2	1.2	1.2	-	-	1.3	1.5	1.5
Percentage-%	5.7	3.6	-	33.3	5.3	0.9	-	-	7.3	3.4	6.1
SiC 50°C inside	C_{1s}								Si_{2p}		
Percentage-%	66.6								10.6		
Peak	C-Si	O-C-Si	C=C	C-C	C-O	C=O	O-C=O	pi-pi*	Si-C	O-Si-C	SiO_2
Position-eV	282.4	283.4	284.4	285.3	286.4	287.7	289.2	291.0	100.3	101.7	103.1
FWHM-eV	1.1	1.2	1.2	1.2	1.2	1.2	1.2	1.2	1.3	1.5	1.5
Percentage-%	6.7	3.2	24.8	18.0	10.0	2.4	1.1	0.4	6.9	1.7	2.0

4.4.3. Discussions

Lambda ratio is calculated first to confirm if asperities are in contact at 50°C. Considering a curvature radius inside wear scar measured to 11.7 mm and Sa of steel wear of 32.3 nm, the lambda value is 0.14. The change of viscosity due to adding 0.3 wt% hypericin into glycerol is negligible because hypericin is a small molecule. Since lambda is well below unity, contact between asperities should be taken into account.

Based on analyses, both steel and SiC topmost surfaces are enriched in carbon species with folded rings. Hypericin itself being constituted of 6 carbon rings, the species present on wear surfaces are hypericin, polymeric structures, or degradation products. When contacting surfaces are rich in sp^2 carbon or carbon folded rings, friction is expected to be low since they push surfaces away thanks to Van des Waals repulsion forces and this avoids cold welding[48,43].

Hypericin is very sensitive to light and under photons activation and in the presence of dioxygen molecules, singlet oxygen[49] can be produced which presents the lowest excited state of diatomic oxygen molecule with all electrons paired. Singlet oxygen is very reactive and easily oxidizes other components[50]. Interestingly, under an oxygen atmosphere, shearing enables the formation of silica and graphite species on SiC[51] keeping CoF under 0.1. In air, depending on the humidity, the CoF of SiC varies from 0.2 to 0.7[52,53] without an obvious trace of graphite. This indicates that dioxygen from the air is not sufficient to generate graphite species on SiC. However, we propose that singlet oxygen released by hypericin could complete the following reaction:

$$SiC + O_{2(singlet)} \xrightarrow{hypericin} SiO_2 + C\ (g)$$

To check if light has an impact on hypericin performance, the same test at 50°C has been conducted in the dark. The result shows that the final CoF at 1.9h is 0.016 instead of 0.009 under the light (Fig. 7a). Moreover, when no light is applied, the steel wear scar turns to white (Fig. 7b). Even though black particles are still present in wear scar, its coverage rate over steel wear, sharply decreases compared with the case with light (Fig. 3d). As for SiC, no big difference has been observed with or without light (Fig. 7b). This test indicates that light can influence the hypericin accumulation on a steel ball and hypericin is at the origin of friction decrease to reach the superlubricity regime after 1.9 h sliding. In summary, light has certainly an impact on friction reduction and wear performance of hypericin and it can effectively influence the carbon species accumulating on the steel surface. However, in the represent state, we can't distinguish it is hypericin or graphite species in the contact that has the main role.

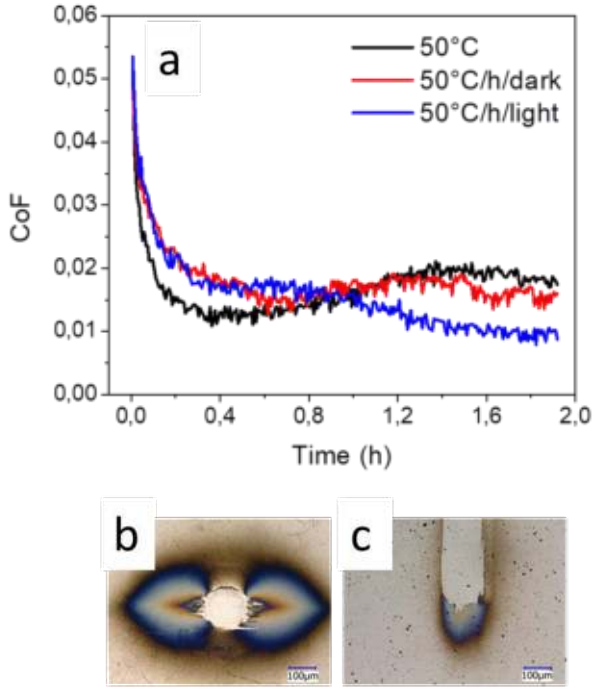

Fig.7 a Friction curve of steel/SiC lubricated with a glycerol-hypericin mixture in dark. Here, the same test performed under the light and steel/SiC lubricated just by glycerol is added for comparison. Optical images of **b** steel wear scar **c** SiC wear scar in dark.

4.4.4. Conclusions

In this research, the application of hypericin has been extended from medicine to friction modifiers in lubricants. It can boost the lubricity of glycerol by penetrating the contact. Moreover, with the help of hypericin, the steel/SiC tribosystem can achieve superlubricity up to 80°C in glycerol. Even at 120°C, it still improves friction by limiting CoF below 0.04. Last but not least, its performance can be controlled by a light supplement. However, the lubricating mechanisms of hypericin require to be further studied.

4.5. References

[1] Björling, M., & Shi, Y. (2019). DLC and glycerol: Superlubricity in rolling/sliding elastohydrodynamic lubrication. *Tribology Letters*, *67*(1), 23.

[2] Habchi, W., Matta, C., Joly-Pottuz, L., De Barros, M. I., Martin, J. M., & Vergne, P. (2011). Full film, boundary lubrication and tribochemistry in steel circular contacts lubricated with glycerol. *Tribology Letters*, *42*(3), 351.

[3] Stachowiak, G., & Batchelor, A. W. (2013). *Engineering tribology*. Butterworth-Heinemann.

[4] Nijenbanning, G. C. H. H., Venner, C. H., & Moes, H. (1994). Film thickness in elastohydrodynamically lubricated elliptic contacts. *Wear*, *176*(2), 217-229.

[5] Ferreira, V., Yoshimura, H. N., & Sinatora, A. (2012). Ultra-low friction coefficient in alumina–silicon nitride pair lubricated with water. *Wear*, *296*(1-2), 656-659.

[6] Chen, Z., Liu, Y., Zhang, S., & Luo, J. (2013). Controllable superlubricity of glycerol solution via environment humidity. *Langmuir*, *29*(38), 11924-11930.

[7] Ronkainen, H., Varjus, S., & Holmberg, K. (2001). Tribological performance of different DLC coatings in water-lubricated conditions. *Wear*, *249*(3-4), 267-271.

[8] Kano, M., Martin, J. M., Yoshida, K., & Bouchet, M. I. D. B. (2014). Super-low friction of ta-C coating in presence of oleic acid. Friction, 2(2), 156-163.

[9] Matta, C., Joly-Pottuz, L., Bouchet, M. D. B., Martin, J. M., Kano, M., Zhang, Q., & Goddard III, W. A. Superlubricity and tribochemistry of polyhydric alcohols. *Phys. Rev. B* **78**, 085436 (2008).

[10] Pireaux, J. J. High resolution XPS of organic polymers: the scienta ESCA300 database: by G. Beamson and D. Briggs, Wiley, Chichester, 1992, 295+ IX pages,£ 65.00 (1993).

[11] Doren, A., Genet, M. J., & Rouxhet, P. G. Analysis of poly (ethylene terephthalate)(PET) by XPS. *Surf. Sci. Spectra* **3**, 337-341 (1994).

[12] Cheng, X., Feng, Z., Li, C., Dong, C., & Li, X. Investigation of oxide film formation on 316L stainless steel in high-temperature aqueous environments. *Electrochimica Acta* **56**, 5860-5865 (2011).

[13] Jordi, L., Iliev, C., & Fischer, T. E. Lubrication of silicon nitride and silicon carbide by water: running in, wear and operation of sliding bearings. *Tribol. Lett*. **17**, 367-376 (2004).

[14] Tomizawa, H., & Fischer, T. E. Friction and wear of silicon nitride and silicon carbide in water: hydrodynamic lubrication at low sliding speed obtained by tribochemical wear. *ASLE transactions* **30**, 41-46 (1987).

[15] Zeng, Q., Dong, G., & Martin, J. M. Green superlubricity of Nitinol 60 alloy against steel in presence of castor oil. *Sci. Rep*. **6**, 29992 (2016).

[16] Ghose, S. K., Waychunas, G. A., Trainor, T. P., & Eng, P. J. Hydrated goethite (α-FeOOH)(1 0 0) interface structure: Ordered water and surface functional groups. *Geochimica et Cosmochimica Acta* **74**, 1943-1953 (2010).

[17] Hu, W., Lowry, B., & Varma, A. Catalytic Oxidation of glycerol to dihydroxyacetone. *In 21st International Symposium on Chemical Reaction Engineering* ISCRE (Vol. 21) (2016).

[18] Ferreira, A. G. M.; Egas, A. P. V; Fonseca, I. M. A.; Costa, A. C.; Abreu, D. C.; Lobo, L. Q. The Viscosity of Glycerol. *J. Chem. Thermodyn.* **2017**, *113*, 162–182.

[19] Wagner, C. D.; Naumkin, A. V; Kraut-Vass, A.; Allison, J. W.; Powell, C. J.; Rumble Jr., J. R. NIST standard reference database 20, Version 3.4 (Web Version), (2003).

[20] Guo, X.; Rao, L.; Wang, P.; Zhang, L.; Wang, Y. Synthesis of Porous Boron-Doped Carbon Nitride: Adsorption Capacity and Photo-Regeneration Properties. *Int. J. Environ. Res. Public Health* **2019**, *16*, 581.

[21] Bogdanowicz, R.; Sawczak, M.; Niedzialkowski, P.; Zieba, P.; Finke, B.; Ryl, J.; Karczewski, J.; Ossowski, T. Novel Functionalization of Boron-Doped Diamond by Microwave Pulsed-Plasma Polymerized Allylamine Film. *J. Phys. Chem. C* **2014**, *118*, 8014–8025.

[22] Kuzharov, A. A.; Lukyanov, B. S.; Kuzharov, A. S. Tribochemical Transformations of Glycerol. *J. Frict. Wear* **2016**, *37*, 337–345.

[23] Baudry, J., Charlaix, E., Tonck, A., & Mazuyer, D. (2001). Experimental evidence for a large slip effect at a nonwetting fluid− solid interface. *Langmuir*, *17*(17), 5232-5236.

[24] Lin, B., Ding, M., Sui, T., Cui, Y., Yan, S., & Liu, X. (2019). Excellent water lubrication additives for silicon nitride to achieve superlubricity under extreme conditions. *Langmuir*, *35*(46), 14861-14869.

[25] Chen, M., Kato, K., & Adachi, K. (2001). Friction and wear of self-mated SiC and Si3N4 sliding in water. *Wear*, *250*(1-12), 246-255.

[26] Chen, M.; Kato, K.; Adachi, K. The Comparisons of Sliding Speed and Normal Load Effect on Friction Coefficients of Self-Mated Si_3N_4 and SiC under Water Lubrication. *Tribol. Int.* **2002**, *35*, 129–135.

[27] Li, J.; Zhang, C.; Ma, L.; Liu, Y.; Luo, J. Superlubricity Achieved with Mixtures of Acids and Glycerol. *Langmuir* **2013**, *29*, 271–275.

[28] Sasaki, S. (1989). The effects of the surrounding atmosphere on the friction and wear of alumina, zirconia, silicon carbide and silicon nitride. *Wear*, *134*(1), 185-200.

[29] Pimenta, M. A., Dresselhaus, G., Dresselhaus, M. S., Cancado, L. G., Jorio, A., & Saito, R. (2007). Studying disorder in graphite-based systems by Raman spectroscopy. *Physical chemistry chemical physics*, *9*(11), 1276-1290.

[30] Dietrich, P. M., Glamsch, S., Ehlert, C., Lippitz, A., Kulak, N., & Unger, W. E. (2016). Synchrotron-radiation XPS analysis of ultra-thin silane films: Specifying the organic silicon. *Applied Surface Science*, *363*, 406-411.

[31] Joly-Pottuz, L., Martin, J. M., Bouchet, M. D. B., & Belin, M. (2009). Anomalous low friction under boundary lubrication of steel surfaces by polyols. *Tribology letters*, *34*(1), 21-29.

[32] Han, T., Zhang, C., Chen, X., Li, J., Wang, W., & Luo, J. (2019). Contribution of a Tribo-Induced Silica Layer to Macroscale Superlubricity of Hydrated Ions. *The Journal of Physical Chemistry C*, *123*(33), 20270-20277.

[33] Ferreira, V., Yoshimura, H. N., & Sinatora, A. (2012). Ultra-low friction coefficient in alumina–silicon nitride pair lubricated with water. *Wear*, *296*(1-2), 656-659.

[34] Bouchet, M. I. D. B., & Kano, M. (2007). Superlubricity of Diamond/Glycerol Technology Applied to Automotive Gasoline Engines. In *Superlubricity* (pp. 471-492). Elsevier Science BV.

[35] Dienwiebel, M., Verhoeven, G. S., Pradeep, N., Frenken, J. W., Heimberg, J. A., & Zandbergen, H. W. (2004). Superlubricity of graphite. *Physical review letters*, *92*(12), 126101.

[36] Ge, X., Li, J., Zhang, C., & Luo, J. (2018). Liquid superlubricity of polyethylene glycol aqueous solution achieved with boric acid additive. *Langmuir*, *34*(12), 3578-3587.

[37] Li, J., Ge, X., & Luo, J. (2018). Random occurrence of macroscale superlubricity of graphite enabled by tribo-transfer of multilayer graphene nanoflakes. *Carbon*, *138*, 154-160.

[38] Ge, X., Li, J., Luo, R., Zhang, C., & Luo, J. (2018). Macroscale superlubricity enabled by the synergy effect of graphene-oxide nanoflakes and ethanediol. *ACS applied materials & interfaces*, *10*(47), 40863-40870.

[39] Oubre, A. (1991). Hypericin: The Active Ingredient in Saint John's Wort. *Archived from the original on September*, *28*, 2007.

[40] Tahara, Y., Sakamoto, T., Oshima, Y., Ishibashi, T., Inomata, H., Murata, T., ... & Ryan, S. J. (1999). The antidepressant hypericin inhibits progression of experimental proliferative vitreoretinopathy. *Current eye research*, *19*(4), 323-329.

[41] Weber, W., Vander Stoep, A., McCarty, R. L., Weiss, N. S., Biederman, J., & McClellan, J. (2008). Hypericum perforatum (St John's wort) for attention-deficit/hyperactivity disorder in children and adolescents: a randomized controlled trial. *Jama*, *299*(22), 2633-2641.

[42] Agostinis, P., Vantieghem, A., Merlevede, W., & de Witte, P. A. (2002). Hypericin in cancer treatment: more light on the way. *The international journal of biochemistry & cell biology*, *34*(3), 221-241.

[43] Bouchet, M. I. D. B., Martin, J. M., Avila, J., Kano, M., Yoshida, K., Tsuruda, T., ... & Asensio, M. C. (2017). Diamond-like carbon coating under oleic acid lubrication: Evidence for graphene oxide formation in superlow friction. *Scientific reports*, *7*(1), 1-13.

[44] Raser, L. N., Kolaczkowski, S. V., & Cotton, T. M. (1992). Resonance Raman and surface-enhanced resonance Raman spectroscopy of hypericin. *Photochemistry and photobiology*, *56*(2), 157-162.

[45] Cooper, A. J., Wilson, N. R., Kinloch, I. A., & Dryfe, R. A. (2014). Single stage electrochemical exfoliation method for the production of few-layer graphene via intercalation of tetraalkylammonium cations. *Carbon*, *66*, 340-350.

[46] Wegewitz, L., Prowald, A., Meuthen, J., Dahle, S., Höfft, O., Endres, F., & Maus-Friedrichs, W. (2014). Plasma chemical and chemical functionalization of polystyrene colloidal crystals. *Physical Chemistry Chemical Physics*, *16*(34), 18261-18267.

[47] C.D. Wagner, A.V. Naumkin, A. Kraut-Vass, J.W. Allison, C.J. Powell, J.R.Jr. Rumble, NIST Standard Reference Database 20, Version 3.4 (web version) (http:/srdata.nist.gov/xps/) 2003.

[48] Kuwahara, T., Romero, P. A., Makowski, S., Weihnacht, V., Moras, G., & Moseler, M. (2019). Mechano-chemical decomposition of organic friction modifiers with multiple reactive centres induces superlubricity of ta-C. *Nature communications*, *10*(1), 1-11.

[49] Ehrenberg, B., Anderson, J. L., & Foote, C. S. (1998). Kinetics and yield of singlet oxygen photosensitized by hypericin in organic and biological media. *Photochemistry and photobiology*, *68*(2), 135-140.

[50] Hardwick, J. P. (2015). *Cytochrome P450 function and pharmacological roles in inflammation and cancer*. Academic Press.

[51] Martin, J. M., & MOGNE, L. (1989). Tribochemistry of alpha silicon carbide under oxygen partial pressure. In *International Congress on Tribology, 5 th, Espoo, Finland* (pp. 132-137).

[52] Wäsche, R., Klaffke, D., & Troczynski, T. (2004). Tribological performance of SiC and TiB2 against SiC and Al2O3 at low sliding speeds. *Wear*, *256*(7-8), 695-704.

[53] Wang, Y., Wang, L., & Xue, Q. (2011). Improvement in the tribological performances of Si3N4, SiC and WC by graphite-like carbon films under dry and water-lubricated sliding conditions. *Surface and Coatings Technology*, *205*(8-9), 2770-2777.

Chapter V

5.Superlubricity in vegetable oils

5.1. Controllable green superlubricity of amorphous carbon/Si_3N_4 tribopair assisted by castor oil

Under review of Carbon

Castor oil is obtained by compressing castor beans and the production process keeps its price low (it was sold 0.9 dollars/kg in India in 2007). Moreover, since it is eco-friendly and bio-compatible, castor oil can be applied to the food industry as additives[1], in the medical field as a laxative[2], and cosmetic products as a moisturizer [3]. More interestingly for lubrication, castor oil outperforms other vegetable oils regarding oxidative stability[4] and lubricity[5]. Thus, cheap, green, and tribological performant castor oil deserves to be further studied to find new applications, particularly when using DLC and ceramics substrates.

5.1.1. Experimental parts

In this work, our main idea is to probe how sp^2 content in castor influences the tribological performance of amorphous carbon coatings. Therefore, two different amorphous carbon coatings with 30% and 65% sp^3 content are used (see properties in table 1). In these tests, the counterpart chosen is a Si_3N_4 disk. Additionally, the performance of castor oil is compared with oleic acid, PAO4 and glycerol.

Table 1: Chemical and mechanical properties of selected tribopairs. The sp^3-hybridized carbon contents of a-C and ta-C (55) are deduced from Young's moduli. Here (55) represents the measured hardness. Young's moduli and hardnesses of the coating are measured by nano-indentation.

	Supplier	Production method	Coating thickness -µm	Roughness Sa -nm	Indentation modulus -GPa	$sp^3/(sp^2+sp^3)$ -%	Indentation hardness -GPa
Si_3N_4 disk	LianYunGang HighBorn Technology	Hot pressing sintering	-	6.7	310	-	15.7
a-C	Fraunhofer IWS	Filtered laser-arc PVD	3.2	8.5	237	30%	30
ta-C(55)	Fraunhofer IWS	Filtered laser-arc	4.0	8.1	521	65%	55

PVD

To ensure boundary conditions, sliding speed was fixed equal or below 3 mm/s and temperature at 100°C. More details about experimental conditions are shown in table 2.

Table 2: Experimental conditions associated with tests in castor oil

Tribometer type	Reciprocating
Lubricant	Castor oil, oleic acid, glycerol, PAO4
Temperature	100 °C
Sliding speed	0.5-3 mm/s
Maximum Hertzian contact pressure	Around 262 MPa

5.1.2. Results

Systematic sliding tests are conducted with a-C/Si_3N_4 friction pair to explore the lubrication ability of castor oil under different sliding speeds. All tests display a short running-in period and CoF stabilizes within 5 to 15 minutes (Fig. 1a). However, sliding speed influences the initial and steady-state CoFs; the initial CoF under 0.5 mm/s speed is 0.03, i.e. more than twice the initial CoF for the other two sliding speeds. As for steady-state CoF, it decreases from 0.02 to 0.005 in a superlubricious regime (CoF<1% by definition), and superlubricity is achieved once the sliding speed is above or equal to 1.5 mm/s. Amazingly, no wear track can be detected on Si_3N_4 flat by optical microscopy, this is rather unexpected because of the lower hardness of Si_3N_4 compared to a-C (Fig. 1b-d). On the a-C pin, a homogenous bright wear scar is formed after friction (Fig. 1e-g). At 0.5 mm/s sliding speed, the wear scar diameter nearly corresponds to the Hertzian contact diameter meaning that only elastic deformation occurred. At 1.5 and 3 mm/s speeds, the wear diameter on the pin slightly increases up to 650 µm. This is very different from ceramic pairs lubricated by the water[6] where huge wear usually occurs and pressure completely collapses. In our cases, only a small reduction of apparent contact pressure from 176 MPa to 150 MPa has been observed. Local height distributions of asperities in 126 x 95 μm^2 areas inside wear track are shown (Fig. 1h-k). Comparing with virgin a-C (Fig. 1h), the majority of heights are near zero for these samples after friction, corresponding to a color change from orange to light blue on the 3D profiles. As

a consequence, surface roughness Sa slightly decreases from 8.5 nm (outside wear scar) to a value around 6 nm inside (Table 2).

Similar results were obtained with the harder ta-C(55) coating. However, replacement of a-C by ta-C(55) leads to a higher initial and steady-state CoF in the same conditions (Fig. 1l). The threshold sliding speed to enter the superlubricious regime increases from 1.5 mm/s for a-C to 3 mm/s for ta-C(55). Optically, no visible difference has been observed for the two cases after friction on Si_3N_4 flats: wear diameter and homogeneity of color except wear on a-C displays to be white while ta-C (55) is light blue (Fig. 1p-r). The 3D profiles of ta-C (55) wear scars (Fig. 1s-v) show a significant polishing is only shown at 3 mm/s. Instead of polishing ta-C (55) surfaces, many scratches are generated under 0.5 mm/s and 1.5 mm/s. Therefore, sliding speed is one of the key factors to reach superlubricity, having not only an impact on film thickness calculated values but also on the final surface topography (Table 3). The higher steady CoF of ta-C (55) compared to a-C under 0.5 mm/s and 1.5 mm/s could be due to its lambda ratio (ratio between the liquid film thickness and the composite roughness of the surfaces). However, this does not explain why the CoF of a-C stabilizes at 0.005 under 3 mm/s while the steady CoF of ta-C (55) is significantly higher at 0.008 although similar final surface roughnesses are observed in both cases (same sliding speed ensures similar castor oil film thickness and lambda ratio).

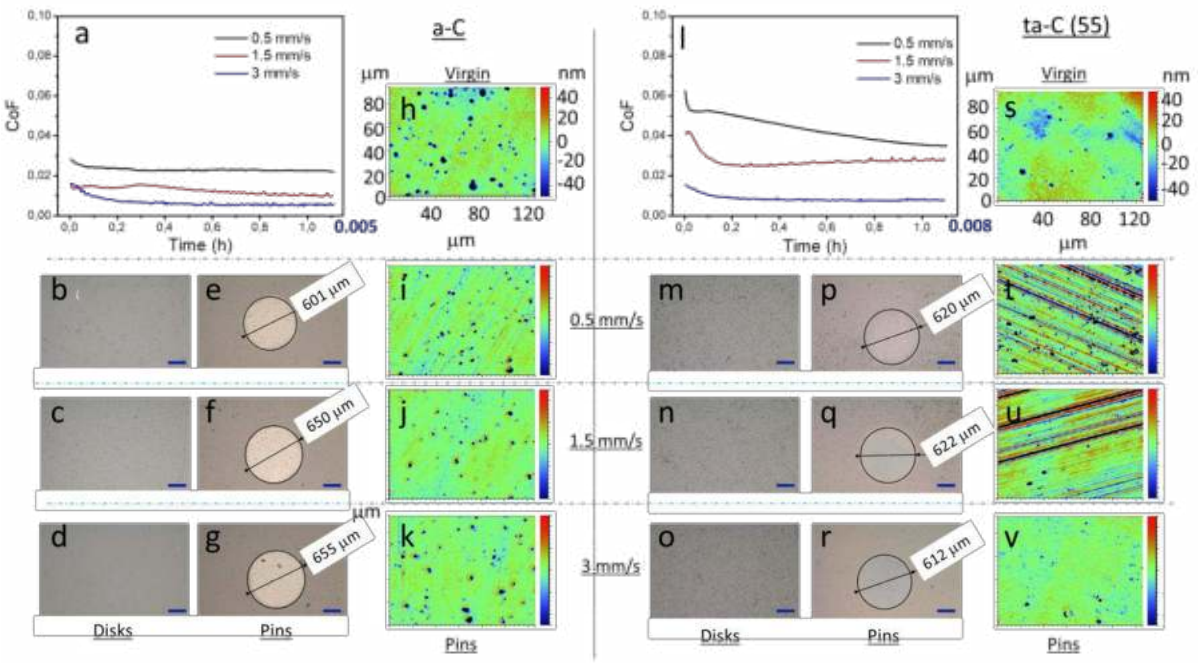

Fig. 1 Friction experiments of ta-C/Si_3N_4 and a-C/Si_3N_4 tribopairs lubricated by castor oil in boundary regime: **a** friction curves under different sliding speed with a-C. Optical images of wear scar on Si_3N_4

flat lubricated by **b-d** castor oil where the scale bars in blue are always 200 µm **e-g** optical images of a-C pins lubricated by castor oil at different sliding speeds of **b**,**e** 0.5 mm/s; **c**,**f** 1.5 mm/s; **d**,**g** 3 mm/s **h** 3D profile of virgin a-C, **i-k** 3D profiles of a-C wear scars lubricated by castor oil at **i** 0.5 mm/s, **j** 1.5 mm/s, **k** 3 mm/s. **l-v** same nomenclatures are used for the case of ta-C(55).

Table 2: Comparison of ta-C and a-C parameters after friction. Apparent pressure is taken as the ratio between normal force and wear area.

Sliding speed (mm/s)	0.5		1.5		3	
Counterpart/Si_3N_4	a-C	ta-C (55)	a-C	ta-C (55)	a-C	ta-C (55)
CoF at 1.1 h	0.021	0.035	0.010	0.027	0.005	0.008
Roughness Sa of virgin pin (nm)	8.5	8.1	8.5	8.1	8.5	8.1
Roughness Sa of pin after friction (nm)	6.7	16.3	6.5	15.9	5.4	5.4
Apparent pressure (MPa)	176	166	151	165	148	170
Radius of wear scar curvature after friction (mm)	105.8	100.1	116.1	129.1	124.7	105.4

To reveal the underlying mechanism, XPS/AES analysis is used to investigate surface chemistry changes inside and outside of wear scars for pins obtained at a sliding speed of 3 mm/s. Unfortunately, Si_3N_4 flats could not be analyzed because the wear scar is not visible by optical microscopy so only ta-C and a-C pins are analyzed after friction. Due to a lack of characteristic peaks other than C_{1s}, spectra are calibrated for all samples by fixing the C_{1s} photopeak at 284.8 eV corresponding to both C-C and C=C chemical bonds. However, the FWHM of C-C/C=C peak inside wear scar is found to be significantly larger than outside (Figure 2, Table 3), regardless of the amorphous carbon type. This may be explained by a change of C-C/C=C ratio and more probably an increase of C=C bonds. Moreover, comparing outside and inside of wear scars, stronger contributions of C-O, C=O, and O-C=O (peaking at 286.3, 287.5, 289.0 eV, respectively) are found inside of wear scar. In particular, the increase of C-O content inside wear scar is remarkable compared with outside: a-C shows an increase of nearly 30% of C-O compared to outside while ta-C(55) exhibits only 21%. This result could originate from the chemical reaction of castor oil (or its degradation products) on amorphous carbon.

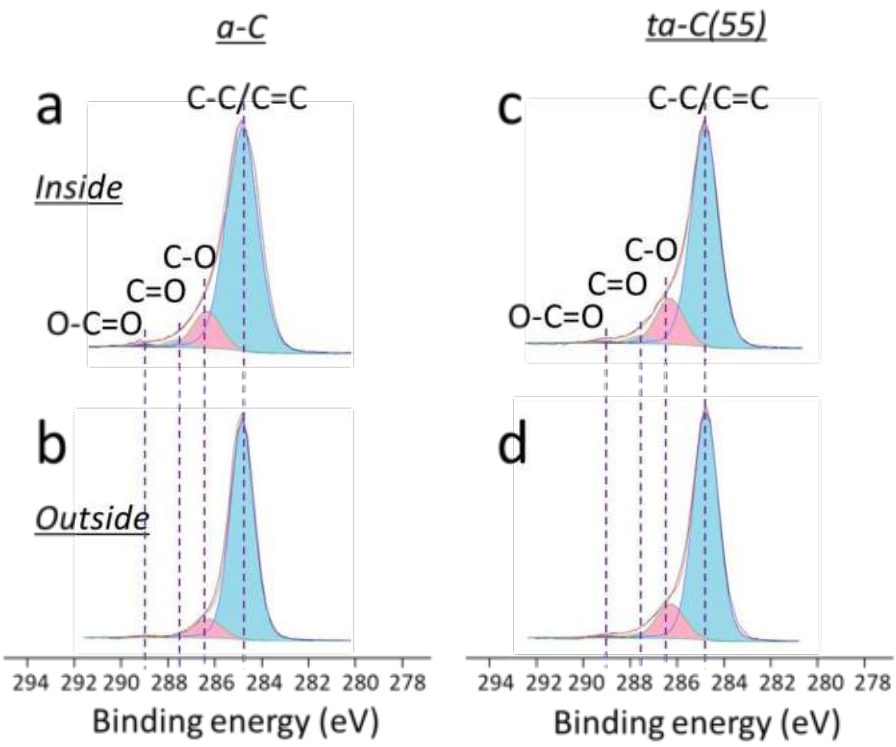

Fig. 2 C_{1s} XPS spectra of ta-C and a-C pins at 3 mm/s, where **a**,**c** recorded inside of wear scar for **a** a-C, **c** ta-C(55) while **b**,**d** recorded outside of wear scar for **b** a-C and **d** ta-C(55).

Table 3: Fitting details of Figure 2.

	C-C/C=C	C-O	C=O	O-C=O
Binding energy (eV)	284.8	286.3	287.5	290.0
a-C inside wear scar				
FWHM (eV)	1.6	1.4	1.4	1.2
Content (%)	84.3	12.0	2.6	1.1
a-C outside wear scar				
FWHM (eV)	1.2	1.4	1.4	1.2
Content (%)	90.0	9.4	-	0.6
ta-C(55) inside wear scar				
FWHM (eV)	1.4	1.4	1.4	1.4
Content (%)	79.2	16.7	3.1	1.0
ta-C(55) outside wear scar				
FWHM (eV)	1.2	1.4	1.4	1.4
Content (%)	83.0	13.8	2.1	1.1

Since the change in sp^2 carbon content before and after friction cannot be deduced accurately from the fitting of the XPS C_{1s} peak, we investigated the Auger C *KLL* first-derivative signal in the XPS spectra (so-called XAES) to identify more accurately the hybridization state of carbon at the extreme surface. In Figure 3, distances between the highest and lowest energy (known as the D value) are shown and compared with pure graphite and diamond from the literature (Figure 3c). Larger D values mean higher content of sp^2 carbon[7]. Our results show that larger D values are always observed inside wear scar compared to outside for both types of amorphous carbon. Interestingly, an additional shoulder appears between the highest and lowest energies inside a-C wear scar. Such an extra peak often shows up while analyzing pure graphite (Figure 3c). The AES data strongly supports the tribo-induced re-hybridization of carbon from sp^3 towards sp^2 in good agreement with our previous XPS analysis. This enrichment in graphitic-like carbon is located at the extreme surface of the wear scar since the Auger C *KLL* signal comes from a depth of only about 1 nm compared with the C_{1s} signal coming from 3 nm. It is important to highlight that this sp^2 content increase in the first 1 nm can't associate with the absorption of castor oil and its derivatives. Because taking one castor oil molecule into account, the ratio between C-C/C=C is 50/3. The absorption of castor oil on DLC coating will inevitably cause a rise of C-C content and a decrease of D value, which disagrees with XAES results. As for its derivatives, the formation of a carbonaceous surface rich in sp^2 carbon requires the help of catalysts like magnesium silicon hydroxide[8] or MoN_x-Cu[9], which aren't used in this study. Thus, this sp^2 content increase is certainly from a-C or ta-C sp^2 hybridization under friction.

Summarizing our analytical data, the top surface of a-C is found to be smoother, enriched in both graphitic/graphenic-like carbon nanolayers and C-O species. This situation is typically favorable for giving a very low shear strength offering an efficient pathway to limit the energy dissipation at the top of asperities[10].

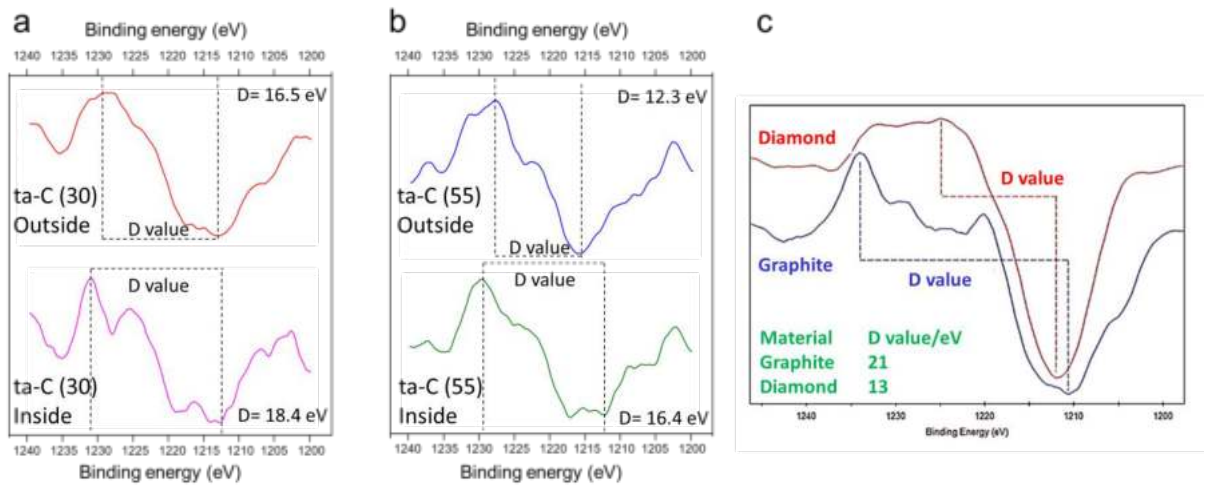

Fig. 3 First derivation of C *KLL* Auger peak: **a** a-C, **b** ta-C(55). Upper spectra correspond to outside of the wear scar; the bottom side corresponds to the inside of wear scar. **c** First derivation of graphite and diamond C *KLL* Auger peaks[11].

To confirm that the occurrence of low friction is essentially linked with graphitic/graphenic-like carbon nanolayer on the surfaces, graphitic layers are deposited on the Si_3N_4 disk and ta-C (55) pin by 6B pencil-drawing. Then the Raman spectrum of the drawn surface leaves strong Raman signals of D, G and 2D peaks at 1325, 1579, 2671 cm^{-1}, respectively (Fig. 4b). G' peak corresponding with impurities in graphitic materials[12] is also detected at 1612 cm^{-1}. This observation is consistent with the fact that the pencil contains not only graphitic materials but also clays.

Intriguingly, with this graphitic layer deposited on ta-C (55) and Si_3N_4, friction test conducted at 3 mm/s and 100°C shows a completely different running-in process. Here, the experimental conditions are the same as in Fig.1l. Instead of starting CoF at 0.016 and slowly decreasing to 0.008 (Fig. 1l), the addition of graphitic coating enables CoF to begin as low as 0.006 (Fig.4a). Unfortunately, this fascinating superlubricity state rapidly vanishes in 0.05 h. After that, CoF follows the same tendency as the case without pencil drawing and stabilizes at around 0.008. Furthermore, after friction, no characteristic signals of graphitic materials are detected by Raman in wear track on ta-C (55), which is similar to Raman signal of virgin ta-C(55) (Fig.4b). These results indicate that graphitic materials deposited by 6B pencil are excluded from the contact area along sliding, which could be the reason that the low friction state of running-in cannot last a long time.

With these penciling experiments, the benefit of having a graphitic layer on the surface is demonstrated. Nevertheless, graphitic layers deposited by pencil are easily removed from the contact area, which results in the rise of friction. Thus, increase sp^2 content in ta-C (such as using a-C) would be more appealing for practical use.

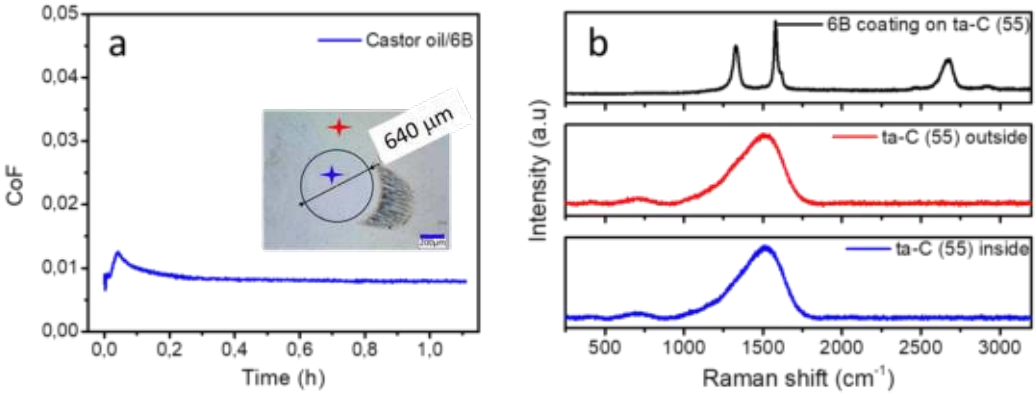

Fig. 4 a Friction curve of ta-C (55) pin sliding against Si_3N_4 disk in castor oil at 3 mm/s, 100°C and 262 MPa. Inset graph corresponds to the wear track of ta-C (55) and blue, red marks indicate where the Raman spectrum is taken **b** Raman spectrum taken inside and outside of ta-C (55) wear track. The graphitic coating deposited by pencil-drawing is presented, too.

Role of lubricants Other than highlighting the importance of sp^2 content in ta-C coating, the advantage of using castor oil is investigated by comparing with other lubricants: GMO, Glycerol, oleic acid, and PAO 4. Analyzed by an infrared spectrometer, GMO, glycerol, and castor oil show wide OH stretching vibration between 3000-3650 cm^{-1} while oleic acid shows broadband in the region 2500-3300 cm^{-1} which features OH stretching of carboxylic acid[13]. At the opposite, no OH stretch has been observed for PAO 4, as expected (Fig. 5b). Interestingly, under identical experimental conditions, superlubricity is only observed for GMO, glycerol, and castor oil which contain OH groups in the carboxylic chains (Fig. 5a). For oleic acid, OH functions only exist in carboxylic acid and final CoF is recorded as 0.012 at 1.1h test duration. Moreover, the use of oleic acid also leaves a larger wear scar on a-C pin than other lubricants (Fig. 5d-h). Highest CoF is correlated with no OH group present in lubricants (such as PAO 4). This observation is consistent with the fact that OH groups are necessary for efficient friction reduction as already reported elsewhere [14].

Raman analyses carried out on amorphous carbon coatings inside and outside the wear track show different structural features after sliding ta-C(55) and a-C (Fig. 5c). No D peak is found for ta-C(55) that is typically a superhard coating, indicating a fully amorphous sp^3-rich carbon

amorphous structure but after sliding, the amorphous structure is retained as no D peak evolved. A very small shift of G peak to lower wavenumbers could be attributed to intrinsic stress relaxation[15] or minor sp^3 to sp^2 rehybridization.

In contrast, a-C shows a distinct D peak in the initial state, indicating nano-clustered sp^2 sites in an overall sp^2-rich amorphous structure. After sliding, the D peak has increased and the G peak has shifted to higher wavenumbers, increasing structured sp^2 sites. It can be seen that all lubricants lead to such ordering of a-C regardless of the friction level achieved.

Raman spectroscopy is probing a much higher depth below the surface compared with XPS and AES. The sp^2 ordering process resulting from sliding is likely a mechanical, shear-induced process and is not the only factor to reach superlubricity. This finding is consistent with similar experiments[14] where shear-induced rehybridization in the subsurface volume was studied with Raman and did not correlate with the superlubricity phenomenon as well.

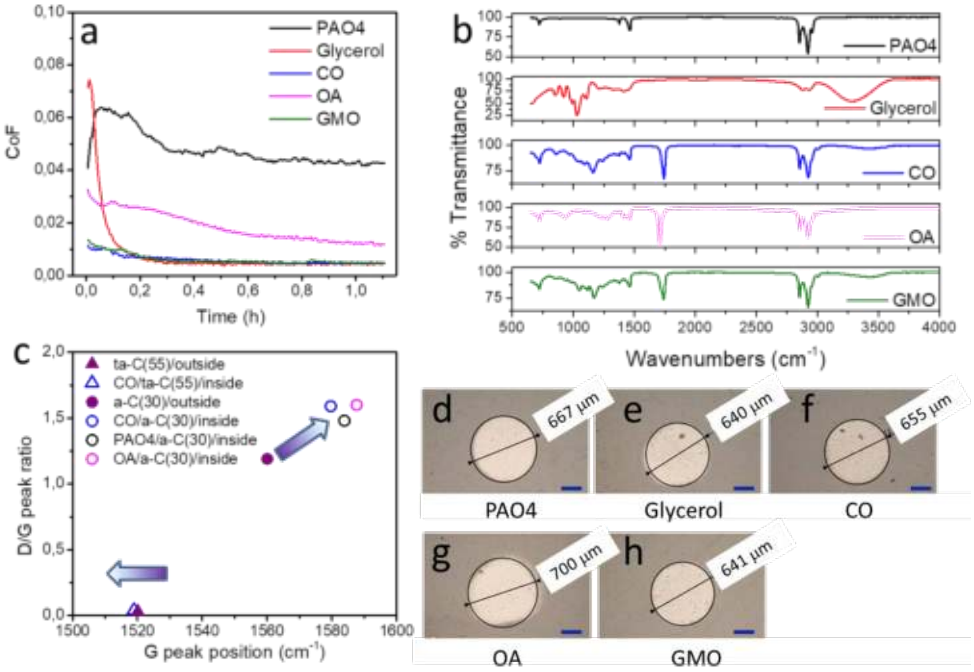

Fig. 5 a Friction evolution with time of a-C/Si_3N_4 tribopairs lubricated by different lubricants at 100 °C, 3 mm/s. **b** FTIR spectrums of different lubricants **c** D and G peaks information acquired from Raman spectra, where arrows indicate change from initial surface (outside) to wear scar (inside) **d-h** optical images of wear scar on the a-C side in PAO 4, glycerol, castor oil, oleic acid, GMO respectively.

5.1.3. Discussions

Superlubricity experiments with castor oil under different sliding speeds highlight the importance of re-hybridization and passivation of carbon atoms at the extreme surface (say two or three atomic layers). As shown in table 4, the calculated lambda values are always well below unity (severe boundary lubrication regime), even after in situ polishing. This indicates that many contacts between asperities take place and support a significant part of the contact pressure all the time, while the residual film thickness is certainly reduced at the nano-scale. The occurrence of solid contacts between asperities through the interfacial zone certainly increases locally the friction compared to a pure hydrodynamic fluid film. This is supported by the increase in CoF with the decrease of sliding speed that is generally observed for the two amorphous carbon coatings. At 1.5 and 3 mm/s sliding speeds, the oil film thickness is calculated to be around 3 and 4.5 nm respectively, meaning that solid contacts contribute to increasing the friction force. Therefore, to maintain the superlubricious regime in action, CoF arises from contacts among asperities that should be relatively low. This need has been met by forming OH terminations on surfaces in our case, which are most likely provided by castor oil and/or its decomposition products.

Table 4: Lubrication regime with castor oil as function of amorhous carbon coating type and sliding speed. Central liquid film thickness (h_c) is calculated by Moes Venner equations[16]: $h_c = R_x \times U^{0.5} [\{(1.70 \times t \times M_2^{-1/9} L^{3/4})^r + (1.96 \times M_2^{-1/9})^r\}^{s/r} + (47.3 \times M_2^{-2})^s]^{1/s}$. Here $G = \alpha E'$, $W_2 = w/E'R_x^2$, $U = \eta_0 u/E'R_x$, $M_2 = W_2/U^{3/4}$, $L = GU^{1/4}$, $r = \exp\{1-6/(L+8)\}$, $s = 12-10\exp(-M_2^{-2})$, $t = 1-\exp(-0.9\ M_2^{1/6}/L^{1/6})$. u, w, R_x are sliding speed, normal force, ball radius in x direction respectively. E' represents reduced elastic modulus ($2/E' = (1-v_1^2)/E_1 + (1-v_2^2)/E_2$), where E and v are the elastic modulus and Poisson ratio of steel and Si_3N_4 since the substrate of ta-C is steel. α and η_0 stand for the visco-pressure coefficient and dynamic viscosity of castor oil. At 100°C, α =12.3 1/GPa, η_0 = 18 mPa·s[17]. Furthermore, lambda is calculated as the ratio between h_c and composite roughness. Because no clear wear scar is observed on the Si_3N_4 disk, the S_a after friction is taken as initial S_a (6.7 nm). Before the test, the film thickness is calculated by taking pin radius of curvature (100 mm). After the test, the film thickness is calculated by taking the final wear scar curvature listed in Table 2.

Sliding speed (mm/s)	0.5		1.5		3	
x/Si_3N_4	a-C	ta-C(55)	a-C	ta-C(55)	a-C	ta-C(55)
Film thickness before test (nm)	1.7	1.7	3.3	3.3	5.2	5.2
Lambda before test	0.16	0.16	0.31	0.31	0.48	0.49
Film thickness after	1.7	1.7	3.6	3.8	5.8	5.3

test (nm)						
Lambda after test	0.18	0.10	0.39	0.22	0.67	0.62

Additionally, contact between asperities can also be reduced by polishing since a lower surface roughness means less chance for asperities to come into contact. The amorphous carbon surfaces are indeed polished which could be attributed either to local high pressure smashing larger asperities into fine wear debris[18] or a chemical polishing[19]. It should be noticed that friction also triggers the re-hybridization of the amorphous carbon surface from sp^3 to sp^2, thus re-orienting the graphitic/graphenic layers to align parallelly to the sliding direction[20]. Therefore, the generation of sp^2-rich tribolayer also contributes to a resulting ultra-smooth surface[21].

In this work, we have observed that graphitic/graphenic-like top monolayers are generated by tribochemical reactions and the surface is partially enriched in hydroxyl groups. The origin of the sp^2-carbon is still unclear. It may come from the re-hybridization process of the amorphous carbon surface even under ultralow friction[22] or from the decomposition of castor oil molecules that contains carbon double bonds. Furthermore, the importance of a sp^2-rich layer on amorphous carbon to limit friction is further confirmed by varying content and structure of the initial sp^2 phase in the ta-C coating.

5.1.4. Conclusions

This study enlarges the potential application range of castor oil as a superlubricant (previously evidenced for nickel alloys) to Si_3N_4 ceramics and H-free DLC (ta-C), a highly wear-resistant tribopair, and this under severe boundary lubrication conditions (low speed and lambda ratio <1). This green superlubricity mechanism is enabled by mitigating the shear strength at the level of asperities by the tribo-induced formation of graphitic/graphenic monolayers. Such mechanism preferentially occurs on sp^2-rich amorphous carbon coatings, initially containing some nanoclusters graphite sites. The importance of carbon re-hybridization process from sp^3 to sp^2 on the chemical adsorption and reaction of the castor oil molecular fragments is highlighted using atomistic calculation (shown in attached publication at the end of this thesis) and additional action on the flattening top surface of asperities at a nano-scale could be expected. Through tailoring initial sp^2-hybridized carbon content at the amorphous carbon surface, the adsorption of reactive species on the asperities can control not only friction and wear but also the speed threshold of the superlubricity regime.

5.2. Role of tribo-pair for reaching superlubricity in castor oil

5.2.1. Experimental parts

For a-C/Si_3N_4, castor oil has been proved to be an excellent lubricant. It is intriguing to probe if castor oil shows good lubricity towards other tribo-pairs. Thus, 5 other tribo-pairs: steel/steel, steel/Si_3N_4, steel/SiC, steel/aC:H, steel/a-C are tested in castor oil under boundary lubrication. Their related properties are listed in Table 1.

Table 1: Mechanical properties of materials. Here, the hydrogen content of aC:H disk is 20%.

	Suppliers	Production method	Diameter-mm	Elastic modulus - GPa	Poisson ratio	Hardness - GPa
Steel pin	Rocholl GmbH	-	200	210	0.3	8.3
Steel disk	PCS Instruments	-	-	210	0.3	7.8
SiC disk	LianYunGang HighBorn Technology	Hot pressing	-	410	0.18	24.5
Si_3N_4 disk	LianYunGang HighBorn Technology	Hot pressing	-	310	0.27	15.7
aC:H disk	HEF	Plasma enhanced CVD	-	260	-	29
a-C	Fraunhofer IWS	Filtered laser-arc PVD	-	237	-	30

As for the experimental conditions, they are presented in Table 2:

Table 2: Experimental conditions associated with tests in castor oil

Tribometer type	Reciprocating
Lubricant	Castor oil
Temperature	100 °C

Sliding speed	3 mm/s
Maximum Hertzian contact pressure	Around 295 MPa

5.2.2. Results

As demonstrated in Fig. 1a, friction behavior in castor oil strongly depends on the tribo-pair type. Superlubricity can only be achieved by sliding steel against a-C among 5 tribo-pair tested, for steel/a-C, CoF starts around 0.015 and decreases to 0.004 in 0.2 h then stabilizes at this value. Even though steel/steel, steel/Si3N4 starts with a similar CoF- 0.015 as steel/a-C, they undergo a continuous increase of friction with time, which differs greatly from how friction evolves with time for steel/a-C. Steel/SiC shares the same tendency as steel/steel and steel/Si_3N_4. The difference majorly lies at steel/SiC begin with higher initial CoF and finishes with higher CoF at 1.1h. The highest initial CoF – 0.11 has been recorded for steel/aC:H. Despite it displays a continuous decrease of CoF as time goes on, the final CoF is 0.04, which is far from the superlubricity regime.

Optically, except steel/a-C, all other 4 tribo-pairs show clear wear scars on steel balls (Fig. 1 b-k). For steel/steel, steel/SiC, and steel/aC:H, evident scratches have been observed on steel balls. For steel/SiC, steel/steel, scratches are also presented on disks. The wear diameters also show significant differences. There are two causes for that:

- Since different tribo-pairs are taken, under the Hertzian pressure of 295 MPa, the contact area varies with tribo-pair.
- Plastic deformation occurs on the steel side.

To eliminate the influence of the first factor, the ratio between wear diameter and Hertzian contact area is used. Except for this ratio of steel/aC:H equals to 1.58, this ratio of the other 4 tribo-pair is below 1.1. This indicates that strong plastic deformation occurs while steel slides against aC:H. As a result of it, the apparent pressure of it drops from 194 MPa to 79 MPa.

Analyzing those wear scars by the interferometer, 3D profiles convert the topographic change by the change of color. The topographical change of virgin steel is majorly within 10 nm (Fig. 1 l). Therefore, its surface presents to be light green. Only the ball of steel/a-C shows a similar color as virgin steel without obvious scratches. Even optically, no scratch has been detected

for the ball of steel/Si_3N_4, its 3D profiles showed that scratches are still presented in its wear scar. Steel/steel and steel/aC:H showed the strongest color contrast in wear. Parts of their wear scar exceed the scale bar and present to be black. For this reason, Steel/steel and steel/aC:H have the greatest Sa – 91.8, 125 nm respectively and Sa of steel ball wear scars follow this sequence: steel/aC:H > steel/steel > steel/SiC > steel/Si3N4 > virgin steel > steel/a-C. In short, except the ball of steel/a-C is polished, other steel balls become rougher after friction.

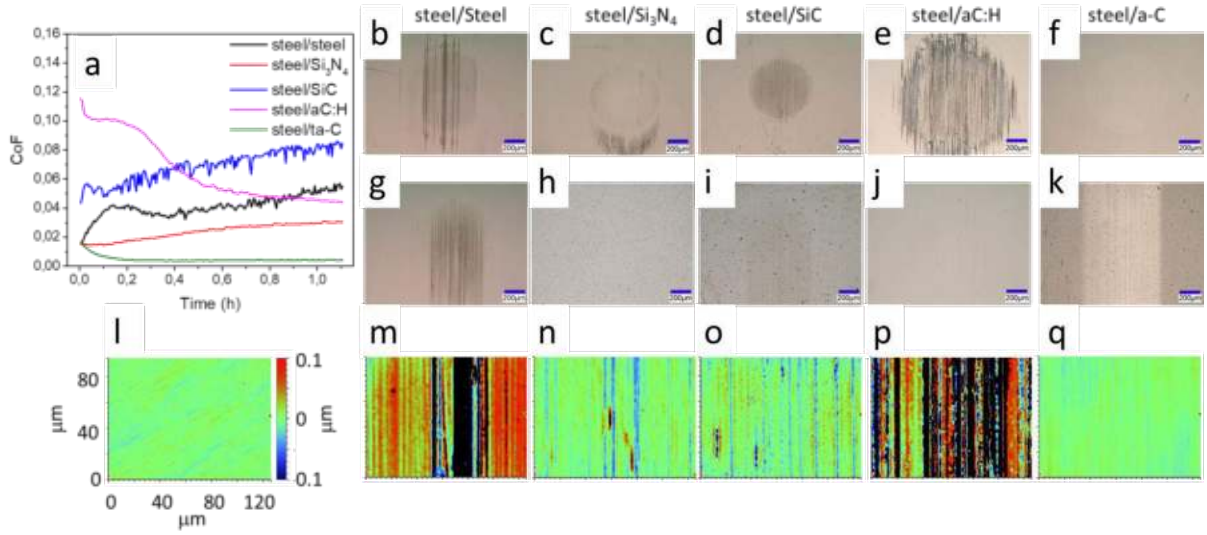

Fig. 1 a Friction evolution on the function of time for all 5 tribo-pairs in castor oil **b-f** optical images of steel ball worn scars, which are arranged in the following sequence from left to right: steel/steel, steel/Si_3N_4, steel/SiC, steel/aC:H, steel/a-C. Here, the scale bar is 200 µm **g-k** optical images of counterpart to a steel ball and they follow the same arrangement as b-f. **m-n** 3D profiles of steel ball worn scars in an area of 126×96 µm. Their arrangement complies with the arrangement from b-f. To facilitate the comparison with virgin steel, 3D profiles of virgin steel is shown and noted as **l**.

As shown in SEM images, the rise of surface roughness not only originates from scratches but also from wear particles accumulating on steel surfaces (Fig. 2). Comparing with virgin steel, EDS analysis of wear particles at steel balls of steel/steel, steel/SiC, steel/Si_3N_4 showed an evident increase of oxygen. For steel/steel, this oxygen increase mainly comes from the presence of Fe_3O_4 because wear particle shows a new peak at 672 cm^{-1} by Raman spectroscopy[23]. However, wear particle of steel/Si_3N_4 contains both a-Fe_2O_3 and Fe_3O_4 because characteristic Raman peaks[24] of a-Fe_2O_3 are detected at 222, 289, 408, 1315 cm^{-1}. Concerning the peak at 1585 cm^{-1}, it corresponds to carbon G-band, which is commonly detected in the composite of a-Fe_2O_3 and carbon[25]. From the result of EDS, a transfer of Si, N

and Al elements from Si_3N_4 side to steel also contribute to compose wear particles. In the Si_3N_4 disk, Al_2O_3 is used as a binder. Na, P elements are expected to originate from castor oil. Respecting steel/SiC, accompanying the increase of oxygen content on a steel ball, Si content increases too. This indicates that element transfers from SiC to steel. However, by Raman (Fig. 3, carbon D, G band are also detected, which means wear particle of steel/SiC is mainly constituted by the composite which contains carbon, silicon, and oxygen. Regarding steel/aC:H, the wear particle covers the Fe signal from the substrate by the strong contribution of carbon and oxygen elements. Furthermore, carbon D, G bands are detected by the Raman spectrum for wear particles. It suggests that wear particle on steel ball is generated by taking carbon from aC:H and under shearing, the wear particle turns partially graphitic.

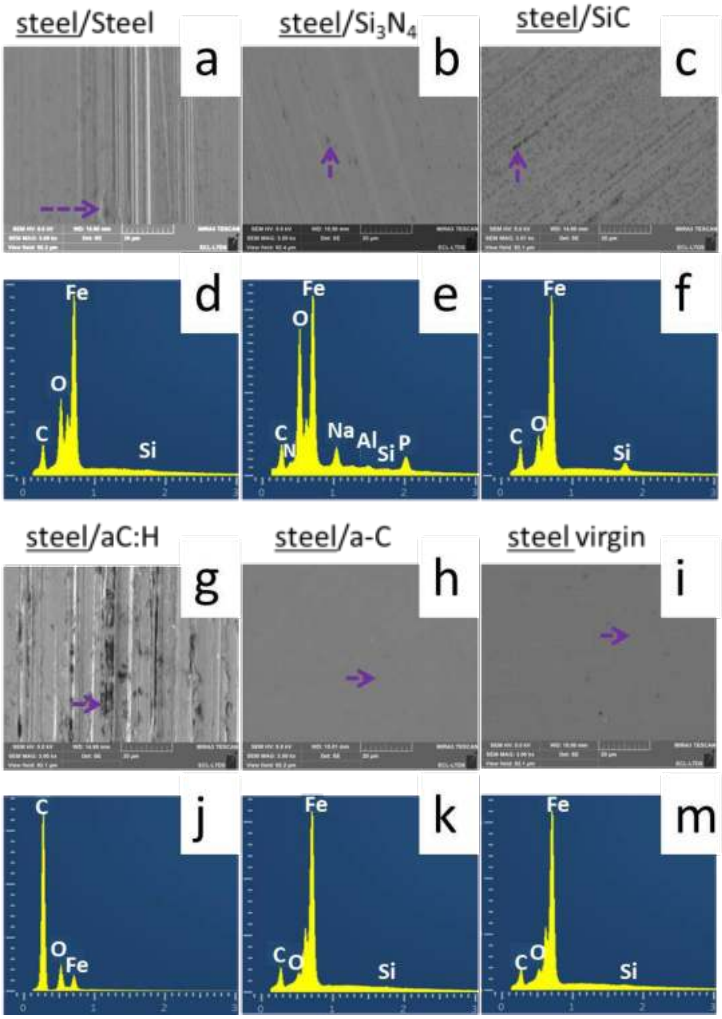

Fig. 2 SEM images of steel ball wear scar under magnification of 3000x: **a** steel/steel, **b** steel/Si3N4, **c** steel/SiC, **g** steel/aC:H, **h** steel/a-C, **i** virgin steel. EDS images of points marked in SEM: **d** steel/steel, **e** steel/Si3N4, **f** steel/SiC, **j** steel/aC:H, **k** steel/a-C, **m** virgin steel.

Being different from other tribo-pairs, steel/a-C leaves no detectable wear particle on steel ball. And the EDS image of steel wear scar displays similar composition and content as virgin steel. So is Raman. Only signals from the steel substrate can be detected in wear scar. Those similarities originate from the information depth of EDS and Raman that is around 1 micron. Therefore, they are not sensitive enough to capture the chemical change on the steel surface.

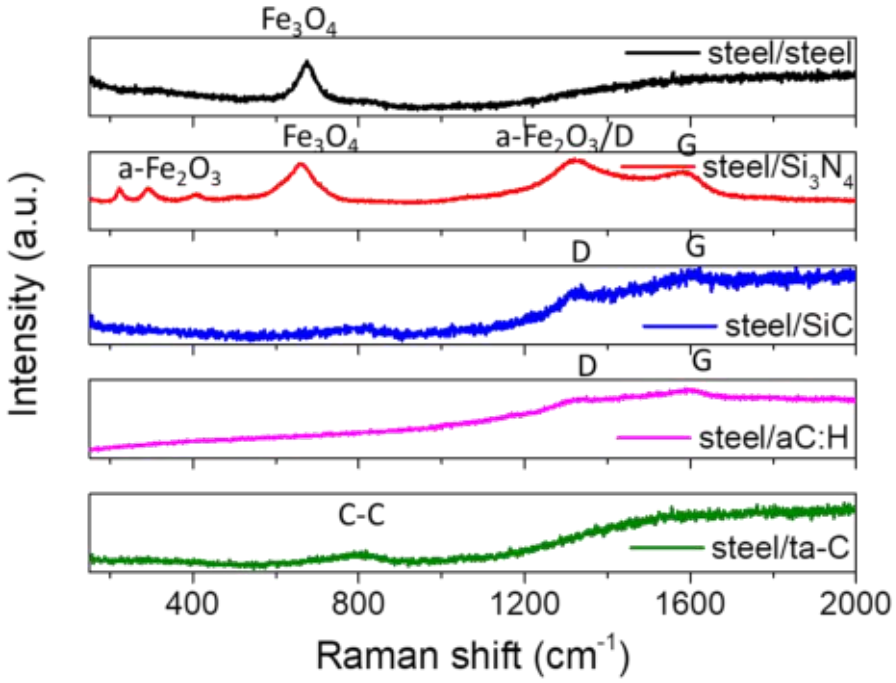

Fig. 3 Raman spectra of wear particles marked in SEM images.

Therefore, XPS analysis is performed on a steel/a-C pair. To have an accurate peak position and tentatively, spectra of steel are calibrated by indexing the peak of FeO_x at 530.0 eV[26] (Fig. 4). After friction, the carbon content of steel wear reaches 54.7 % while outside it is only 41.5% (Table 3). This strong increase in total carbon content is mainly due to the increase of C-C/C=C, C-O, C=O contents. Especially, the content of C-O contribution doubles its value compared to outside wear. It is more precise to take bonds between C and O from C_{1s} than O_{1s} because, at C_{1s} peak, the bonds between C and O are separated while the C-O-C peak overlaps with C=O one at around 532.2 eV, and C-OH shares a similar position with O-C=O at around 533.3 eV[27,28]. However, the result on O_{1s} is clear to demonstrate the change of bonds between Fe and O. For instance, the content of iron oxide shrinks from 18.0% to 10.2% while the content of FeOH remains similar inside and outside the wear scar. Iron oxide is known as the reactive sites to grow the FeOH group on them due to the hydration effect[29].

This phenomenon is likely arising from the diminution of iron oxide layer thickness although a certain amount of iron oxide is still present at the upmost layer to grow FeOH groups. Meanwhile, some water is detected after friction on the steel side. Even though the source of water remains unknown, the existence of water suggests that the surface of the steel wear scar is hydrophilic. It is also a statement that steel surfaces cannot be fully covered by castor oil molecules since castor oil is insoluble in water.

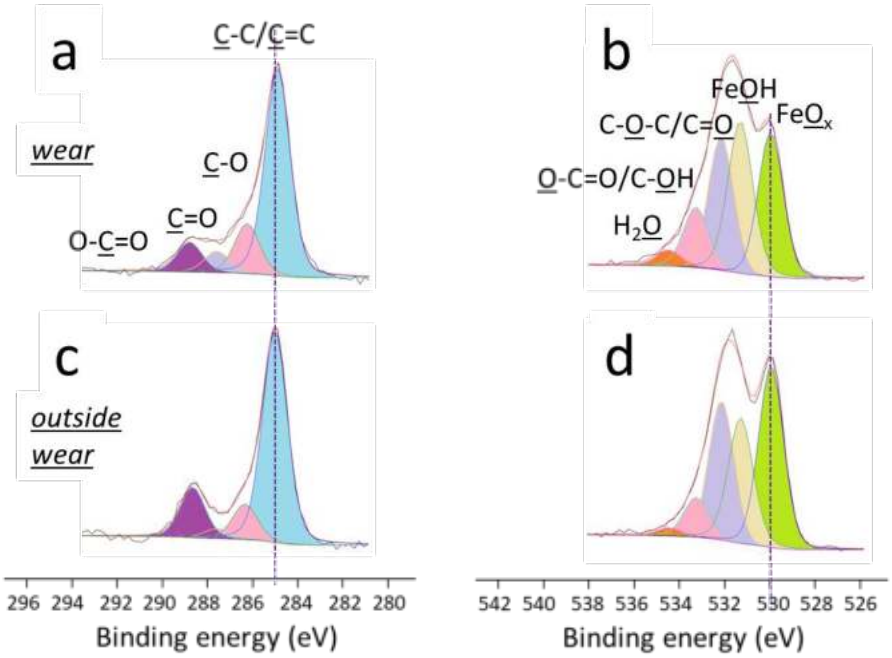

Fig. 4 High-resolution C_{1s} spectra of **a:** steel wear scar **c:** outside of steel wear scar. High-resolution O_{1s} spectra of **b:** steel wear scar **d:** outside of steel wear scar.

On a-C side, due to lacking other reference peak, spectra are calibrated by fixing the binding energy of the major peak of C_{1s} to 284.8 eV. A slight increase of C_{1s} content of 1.6% has been detected inside of wear scar comparing with outside (Fig. 5). It is mainly due to the increase of C-C/C=C and C-O contributions. The greatest difference is the FWHM of C-C/C=C. Inside wear, it is 1.4 eV while outside of wear scar its value is 1.2 eV. Such enlargement of C-C/C=C could be due to the existence of both C-C and C=C bond in the C_{1s} peak (it is reminded here that 68% percent of C_{1s} signal comes from a thickness less than 2.5 nm (diamond is used here to estimate mean free path). When the C *KLL* Auger peak is analyzed, a 68% signal is only from the first 0.8 nm. The first derivation of the C *KLL* Auger peak demonstrates a D value increase and a characteristic shoulder present in the graphitic form. Here D value is defined as the binding energy difference between the highest and

lowest points, which augments with a rise of C=C content[7]. Carbon graphitization in the first 1nm depth confirms that the enlargement of the C-C/C=C peak is linked with the fact that C=C bonding is more pronounced at the extreme surface after friction.

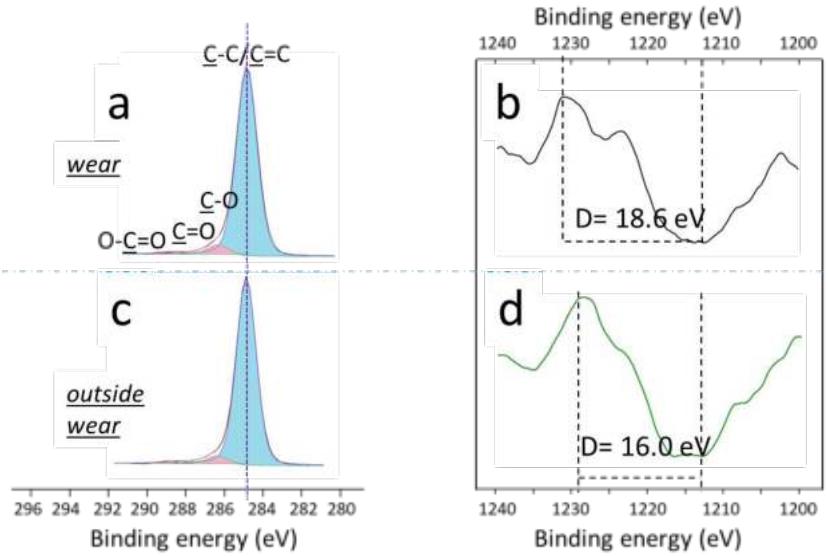

Fig. 5 High-resolution C_{1s} spectra on a: a-C wear scar c: outside of a-C wear scar. The first derivation of C *KLL* Auger peak b: a-C wear scar d: outside of a-C wear scar.

Table 3: Fitting details of the steel side.

Steel wear	C_{1s}				O_{1s}				
Percentage-%	54.7				36.1				
Peaks	C-C /C=C	C-O	C=O	O-C=O	FeO_x	FeOH	C=O /C-O-C	O-C=O /C-OH	H_2O
Positions-eV	284.9	286.2	287.6	288.8	530.0	531.3	532.2	533.3	534.5
FWHM-eV	1.3	1.3	1.3	1.3	1.3	1.3	1.3	1.3	1.3
Percentage-%	36.8	8.8	3.7	5.4	10.2	11.2	9.0	4.5	1.2
Steel outside	C_{1s}				O_{1s}				
Percentage-%	41.5				48.7				
Peaks	C-C /C=C	C-O	C=O	O-C=O	FeO_x	FeOH	C=O /C-O-C	C-OH	H_2O
Positions-eV	285.0	286.3	287.6	288.6	530.0	531.3	532.2	533.3	534.5
FWHM-eV	1.3	1.3	1.3	1.3	1.3	1.3	1.3	1.3	1.3
Percentage-%	28.5	4.8	1.3	6.8	18.0	12.8	13.0	4.1	0.9

Table 4: Fitting details of a-C side.

Steel wear	C_{1s}				O_{1s}
Percentage-%	93.2				6.8
Peaks	C-C/C=C	C-O	C=O	O-C=O	
Positions-eV	284.8	286.3	287.5	288.8	
FWHM-eV	1.4	1.2	1.2	1.2	
Percentage-%	87.7	4.0	0.8	0.7	
Steel outside	C_{1s}				O_{1s}
Percentage-%	91.6				8.4
Peaks	C-C/C=C	C-O	C=O	O-C=O	
Positions-eV	284.8	286.3	287.5	288.8	
FWHM-eV	1.2	1.2	1.2	1.2	
Percentage-%	87.0	3.5	0.4	0.7	

5.2.3. The key to superlubricity in castor oil

Importance to maintain low roughness. As mentioned before, only when a-C is used as a counterpart, the roughness of steel can be maintained at around 5 nm. Sliding steel against other materials always increases steel roughness. The trigger of roughness increase can have 3 origins:

- Iron oxides accumulate in wear scar, such as steel/steel.
- Material transfer from counterpart to steel, like in the case of steel/SiC and steel/aC:H.
- Combination of those two above, for example, steel/Si_3N_4.

Due to the sharp increase of local roughness, lambda value is cut off for at least one half comparing with the case of steel/a-C. This leads to lubrication conditions to be more severe. In former experiments, sliding Si_3N_4 against a-C in castor oil has shown the possibility to reach superlubricity when lambda is around 0.5, where liquid film separation may still play a part. The further decrease of lambda minimizes the impact of liquid film and results in contacts among asperities become dominant. Therefore, friction increases. However, previous calculations have shown that the impact of liquid film would be negligible in maintaining superlow friction because its contribution to CoF is lower than 10^{-4}. Therefore, the contact between asperities is essential to maintain the CoF in the millirange.

Table 5: Film thickness and lambda calculation for each tribo-pair.

	Steel/Steel		Steel/Si3N4		Steel/SiC		Steel/aC:H		Steel/a-C	
CoF at 1.1 h	0.055		0.031		0.085		0.044		0.004	
	Ball	Disk	Ball	Disk	Ball	Disk	Ball	Disk	Ball	Disk
Sa before test–nm	5.5	4.4	5.5	12.4	5.5	9.6	5.5	5.0	5.5	11.2
Sa after test–nm	91.8	14.0	13.4	12.4	19.7	19.7	125	23.0	5.2	9.0
Liquid film thickness-nm	5.4		4.7		4.5		5.0		4.7	
Lambda at 1.1 h	0.06		0.26		0.16		0.04		0.45	

Importance of chemical terminations. Setting aside the influence of roughness, chemical terminations on a-C and aC:H are found to be different. The major difference comes from the presence of HO-C=O functional groups, located at 289.1 eV and is commonly observed for fatty acid[30] (Fig. 6). Its location greatly differs from the -O-C=O group on steel since O-C=O chemisorbs on steel by forming carboxylates[30] while HO-C=O group interacts with aC:H by hydrogen bonds[31]. Since castor oil is a triglyceride of fatty acid and doesn't contain any free acid group, decomposition of castor oil into fatty acid is expected. Fatty acid chains have been reported to show good affinity to aC:H surface. Even without shearing, fatty acid chains naturally adsorb on aC:H[32]. Thus, contact between self-mated aC:H surfaces are expected to take place between self-assembled fatty acid layers for aC:H. In our case, aC:H has been transferred to steel surface. Such material transfer doesn't deplete hydrogen in transfer film[33]. After establishing this carbon transfer film, the contact between steel/aC:H changes into hydrogenated carbon layer against aC:H coating, where self-assembled fatty acid takes over and sliding occurs between them (Fig.7).

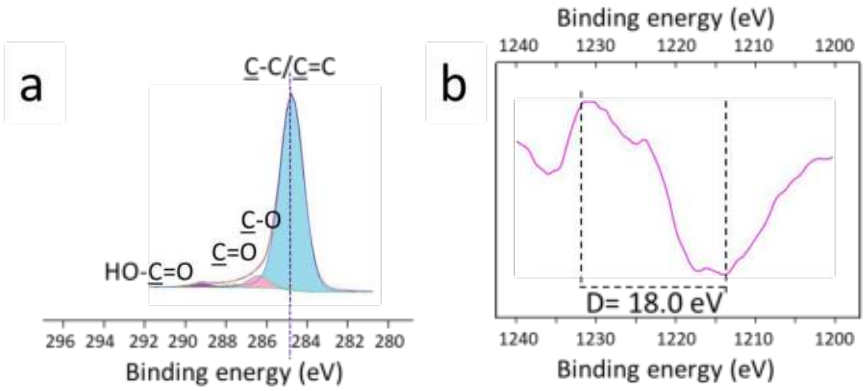

Fig.6 High-resolution C_{1s} spectra of **a** aC:H wear scar. The first derivation of C_{KLL} auger peak **b** aC:H wear scar. Here the FWHM of C-C/C=C is 1.4 eV and the D value is 18 eV, which are similar to the case of a-C after friction. This relatively high content of C=C is not expected to be induced by friction since outside of aC:H wear (not shown here), similar FWHM and D value are observed.

When a-C is used as a counterpart, the O-C=O peak is located at 288.8 eV and becomes nearly invisible (Fig. 5). This indicates that only a very small amount of O-C=O is chemisorbed onto a-C. Other than full fatty acid chains being adsorbed to a-C surface[31], fatty acid chains tend to fully decompose then occupying a-C surface with its fragments[14]. Accordingly, the advantage of replacing aC:H with a-C is to avoid forming self-assembled monolayers with long fatty acid chains since long hydrocarbon chain vibrates and are inter-digitalized during shear, that results in higher energy dissipation[34]. On the opposite, in the case of steel/a-C, the carbon very top surface becomes graphitic with less than 10% oxygen atoms (mainly as C-OH bonds at the edges). The sliding between terminated methyl groups of chemisorbed fatty acids and basal planes of graphitic carbon and/or OH terminations is expected to be very low.

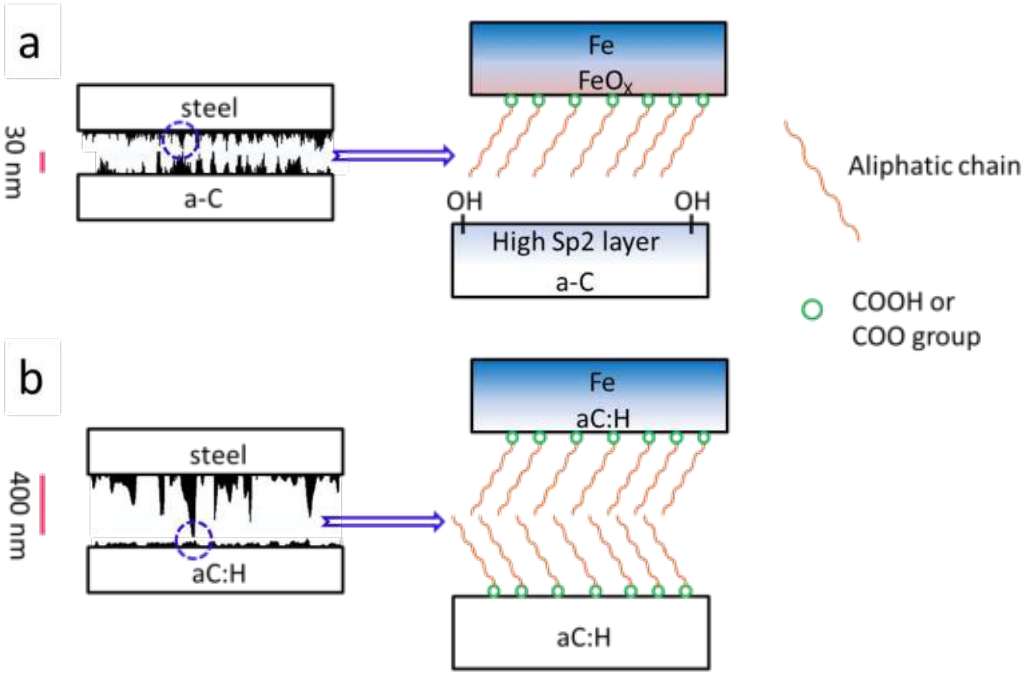

Fig. 7 Schematic images of asperities distribution after friction: a: steel/a-C b: steel/aC:H. graphs on the right side represent different contact mechanism of asperities as a function of tribo-pair.

5.2.4. Conclusions

Tribological behavior in castor oil is highly dependent on the nature of tribo-pairs. Steel/a-C is the only candidate to reach superlubricity in castor oil among the other 5 tested pairs. The occurrence of superlubricity is accompanied by the generation of ultra-smooth wear scar, which is ascribed to the high hardness of a-C which hinders iron oxide accumulation on the steel surface and the surface passivation of a-C by castor oil fragments avoids cold weld and material transfer to increase local roughness.

5.3. References

[1] Wilson, R; Van Schie, BJ; Howes, D (1998). "Overview of the preparation, use and biological studies on polyglycerol polyricinoleate (PGPR)

[2] Bryan, Cyril P. (1930). The Papyrus Ebers, Translated from the German Version By Cyril P. Bryan London: Geoffrey Bles. p. 44. Archived from the original on 2013-09-21.

[3] Zofchak, Albert; John Obeji & Michael Mosquera, "Use urethane polymers of castor oil skin and personal care product compositions"

[4] Said, G., Daniel, P., Badr, K., Mohamed, I., & Zoubida, C. (2016). Chemical characterization and oxidative stability of castor oil grown in Morocco. *Moroccan Journal of Chemistry*, *4*(2), 4-2.

[5] Quinchia, L. A., Delgado, M. A., Reddyhoff, T., Gallegos, C., & Spikes, H. A. (2014). Tribological studies of potential vegetable oil-based lubricants containing environmentally friendly viscosity modifiers. *Tribology International*, *69*, 110-117.

[6] M. Chen, K. Kato, K. Adachi, The comparisons of sliding speed and normal load effect on friction coefficients of self-mated Si3N4 and SiC under water lubrication, Tribol. Int. 35 (2002) 129-135.

[7] J.C. Lascovich, S. Scaglione, Comparison among XAES, PELS and XPS techniques for evaluation of sp^2 percentage in aC: H, Appl. Surf. Sci. 78 (1994) 17-23.

[8] Chang, Q., Rudenko, P., Miller, D. J., Wen, J., Berman, D., Zhang, Y., ... & Erdemir, A. (2017). Operando formation of an ultra-low friction boundary film from synthetic magnesium silicon hydroxide additive. *Tribology International*, *110*, 35-40.

[9] Erdemir, A., Ramirez, G., Eryilmaz, O. L., Narayanan, B., Liao, Y., Kamath, G., & Sankaranarayanan, S. K. (2016). Carbon-based tribofilms from lubricating oils. *Nature*, *536*(7614), 67-71.

[10] X. Chen, C. Zhang, T. Kato, X.A. Yang, S. Wu, R. Wang, N. Masataka, J. Luo, Evolution of tribo-induced interfacial nanostructures governing superlubricity in aC: H and aC: H: Si films, Nat. Commun. 8 (2017) 1-13.

[11] Thermo Fisher Scientific Inc., Carbon, (2013-2020). https://xpssimplified.com/elements/carbon.php (accessed June 3, 2020).

[12] Pimenta, M. A., Dresselhaus, G., Dresselhaus, M. S., Cancado, L. G., Jorio, A., & Saito, R. (2007). Studying disorder in graphite-based systems by Raman spectroscopy. *Physical chemistry chemical physics*, *9*(11), 1276-1290.

[13] P. Excoffon, Y. Marechal, Infrared spectra of H-bonded systems: saturated carboxylic acid dimers, Spectrochimi. Acta A Mol. Spectrosc. 28 (1972) 269-283.

[14] T. Kuwahara, P.A. Romero, S. Makowski, V. Weihnacht, G. Moras, M. Moseler, Mechano-chemical decomposition of organic friction modifiers with multiple reactive centres induces superlubricity of ta-C, Nat. Commun. 10 (2019) 1-11.

[15] J.W. Ager III, S. Anders, A. Anders, I.G. Brown, Effect of intrinsic growth stress on the Raman spectra of vacuum-arc-deposited amorphous carbon films, Appl. Phys. Lett. 66 (1995) 3444-3446.

[16] A.A. LUBRECHT, An introduction to elastohydrodynamic lubrication, Mechanical Engineering and Development Master Degree Course, INSA de Lyon, 2009.

[17] G. Stachowiak, A.W. Batchelor, Engineering tribology, Butterworth-Heinemann, Oxford, 2013.

[18] J. Xu, K. Kato, Formation of tribochemical layer of ceramics sliding in water and its role for low friction, Wear 245 (2000) 61-75.

[19] S. Makowski, F. Schaller, V. Weihnacht, G. Englberger, M. Becker, Tribochemical induced wear and ultra-low friction of superhard ta-C coatings, Wear 392 (2017) 139-151.

[20] L. Pastewka, S. Moser, M. Moseler, Atomistic insights into the running-in, lubrication, and failure of hydrogenated diamond-like carbon coatings, Tribol. Lett. 39 (2010) 49-61.

[21] X. Chen, T. Kato, M. Nosaka, Origin of superlubricity in aC: H: Si films: a relation to film bonding structure and environmental molecular characteristic, ACS Appl. Mater. Interfaces 6 (2014) 13389-13405.

[22] M.D.B. Bouchet, C. Matta, B. Vacher, T. Le-Mogne, J.M. Martin, J. Von Lautz, T. Ma, L. Pastewka, J. Ostchik, P. Gumbsch, M. Moseler, Energy filtering transmission electron microscopy and atomistic simulations of tribo-induced hybridization change of nanocrystalline diamond coating, Carbon 87 (2015) 317-329.

[23] Molchan, I. S., Thompson, G. E., Lindsay, R., Skeldon, P., Likodimos, V., Romanos, G. E., ... & Schubert, T. J. (2014). Corrosion behaviour of mild steel in 1-alkyl-3-methylimidazolium tricyanomethanide ionic liquids for CO 2 capture applications. *RSC Advances*, *4*(11), 5300-5311.

[24] Sirivisoot, S., & Harrison, B. S. (2015). Magnetically stimulated ciprofloxacin release from polymeric microspheres entrapping iron oxide nanoparticles. *International journal of nanomedicine*, *10*, 4447.

[25] Yu, B. Z., Liu, X. L., Zhang, H. G., Jing, G. Y., Ma, P., Luo, Y., ... & Fan, H. M. (2015). Fabrication and structural optimization of porous single-crystal α-Fe 2 O 3 microrices for high-performance lithium-ion battery anodes. *Journal of Materials Chemistry A*, *3*(32), 16544-16550.

[26] Biesinger, M. C., Payne, B. P., Grosvenor, A. P., Lau, L. W., Gerson, A. R., & Smart, R. S. C. (2011). Resolving surface chemical states in XPS analysis of first row transition metals, oxides and hydroxides: Cr, Mn, Fe, Co and Ni. *Applied Surface Science*, *257*(7), 2717-2730.

[27] Beamson, G. (1992). High resolution XPS of organic polymers. *The Scienta ESCA 300 Database*.

[28] Gutić, S., Dobrota, A., Gavrilov, N., Baljozović, M., Pašti, I., & Mentus, S. (2016). Surface charge storage properties of selected graphene samples in pH-neutral aqueous solutions of alkali metal chlorides-particularities and universalities. *Int. J. Electrochem. Sci*, *11*(10), 8662-8682.

[29] Jang, J. H., Dempsey, B. A., & Burgos, W. D. (2007). Solubility of hematite revisited: Effects of hydration. *Environmental science & technology*, *41*(21), 7303-7308.

[30] Loehlé, S., Matta, C., Minfray, C., Le Mogne, T., Iovine, R., Obara, Y., ... & Martin, J. M. (2015). Mixed lubrication of steel by C18 fatty acids revisited. Part I: Toward the formation of carboxylate. *Tribology International*, *82*, 218-227.

[31] Kano, M., Martin, J. M., Yoshida, K., & Bouchet, M. I. D. B. (2014). Super-low friction of ta-C coating in presence of oleic acid. *Friction*, *2*(2), 156-163.

[32] Simič, R., & Kalin, M. (2013). Adsorption mechanisms for fatty acids on DLC and steel studied by AFM and tribological experiments. *Applied Surface Science*, *283*, 460-470.

[33] Chen, X., Zhang, C., Kato, T., Yang, X. A., Wu, S., Wang, R., ... & Luo, J. (2017). Evolution of tribo-induced interfacial nanostructures governing superlubricity in aC: H and aC: H: Si films. *Nature communications*, *8*(1), 1-13.

[34] Mikulski, P. T., & Harrison, J. A. (2001). Packing-density effects on the friction of n-alkane monolayers. *Journal of the American Chemical Society*, *123*(28), 6873-6881.

Chapter VI

6. Superlubricity of fatty acids

6.1. Improving C_{18} fatty acid lubrication performances: investigating the role of C=C and OH function groups in the aliphatic chain

6.1.1. Experimental parts

Three main fatty acid sources compose the structure of castor oil: ricinoleic acid (RA), oleic acid (OA), and linoleic acid (LA). It is interesting to compare their tribological performances and if they can reach superlubricity under boundary lubrication since decomposition of castor oil and surface functionalization serves as the main causes to reduce friction. Here, steel balls and Si_3N_4 disks are used for this research. Their properties are listed below (Table 1).

Table 1: Mechanical parameters of materials.

	Suppliers	Production method	Diameter-mm	Elastic modulus - GPa	Poisson's ratio	Hardness - Gpa
Steel pin	Rocholl GmbH	-	200	210	0.3	8.3
Si_3N_4 disk	LianYunGang HighBorn Technology	Hot pressing	-	310	0.27	15.7

Experimental conditions are presented in Table 2:

Table 2: Experimental conditions associated with tests in 3 different fatty acids. Those 3 fatty acids are bought from Sigma-Aldrich with purity higher than 99%.

Tribometer type	Reciprocating
Lubricant	Ricinoleic acid, oleic acid, linoleic acid
Temperature	50-100 °C
Sliding speed	3 mm/s
Maximum Hertzian contact pressure	Around 295 MPa

6.1.2. Results

Friction tests are conducted at selected different temperatures to get rid of the influence of viscosity change between the acids. Their viscosity-temperature properties are given in table 3. Among them, RA displays the most excellent lubricity with CoF starting at 0.03 while initial CoF for the two other lubricants is around 0.065 (Fig. 1a). More intriguingly, after 1.1 h of friction, CoF in RA decreases to 0.014 while CoFs in OA and LA stay above 0.05. Respecting wear scar, sliding oleic acid, long scratches are found on both steel and Si_3N_4. On the opposite, wear scars in RA and LA are nearly invisible by optical microcopy due to low contrast between the inside and outside of wear scar (Fig. 1b-g). With the help of interferometry, a steel wear scar in LA is found to be covered with 'bumps' with a maximum height of around 40 nm (Fig. 1k). The topography of steel wear scar in OA can be divided into 2 parts: near or far away from black scratch in optical image (Fig. 1b). Around the green rectangle, scratches have a greater difference between summits and valleys than parts near the purple one. For this reason, The Sa value given by (Fig. 1i) is 10.4 nm while the Sa value corresponding to (Fig. 1h) equals to 36.3 nm. The steel surface lubricated by RA shows no obvious positive scratch and scratches with negative heights which could act as a reservoir to retain lubricant (Fig. 1j). Sa is recorded as 4.9 nm comparing with Sa of 5.5 nm for virgin steel, showing that the steel surface is slightly polished.

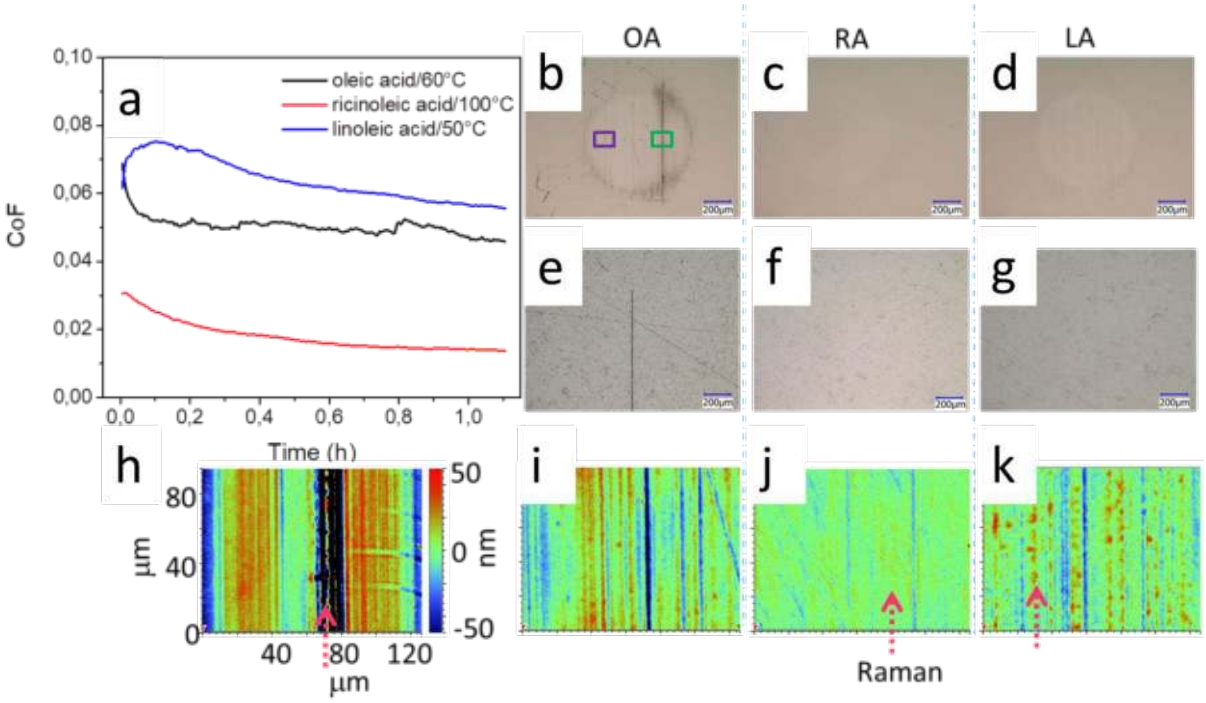

Fig. 1 a Friction evolution on the function of time for steel/Si_3N_4 in OA, RA, LA, here temperature changes with the lubricant used to ensure lubricants share similar viscosity. Optical images of steel wear scar after lubricated by **b** OA, **c** RA, **d** LA. The same arrangement from **e** to **g** for optical images of Si_3N_4 disk wear scar. 3D depth profiles of steel wear scar lubricated by **h**, **i** OA, **j** RA, **k** LA. Here h corresponds to the green rectangular in Fig. b while i represent purple rectangular. The pink arrow points at the area analyzed by Raman.

Table 3: Dynamic viscosities of oleic acid, linoleic acid and ricinoleic acid at different temperatures[1,2].

Viscosity-mPa·s	RA	LA	OA
100°C	11.1	3.3	5.0
80°C	24.8	4.6	7.1
60°C	42.0	8.0	11.1
50°C	73.2	10.3	14.3

The chemical compositions of wear debris present on steel surfaces are studied by SEM/EDS. When steel/Si_3N_4 is lubricated by OA, large wear debris is detected near the black scratch (Fig. 2a) and EDS shows N and Al which is not observed in steel surface outside of wear scar (Fig. 2e, h). Meanwhile, silicon peak becomes more pronounced suggesting material transfer from Si_3N_4 to steel side increasing steel surface roughness. Steel wear scar lubricated by LA shows wear particles covering more than half of the surface (Fig. 2c). Those wear particles contain a lot of oxygen compared with the EDS spectrum from outside wear (Fig. 2g) and the signal from the Si element is also stronger than the one from outside wear. This demonstrates that some material has been transferred from Si_3N_4 to the steel side and iron oxides probably accumulate in wear scar too. The steel surface lubricated by RA shows similar elements as outside wear scar and no visible wear debris has been observed (Fig. 2f).

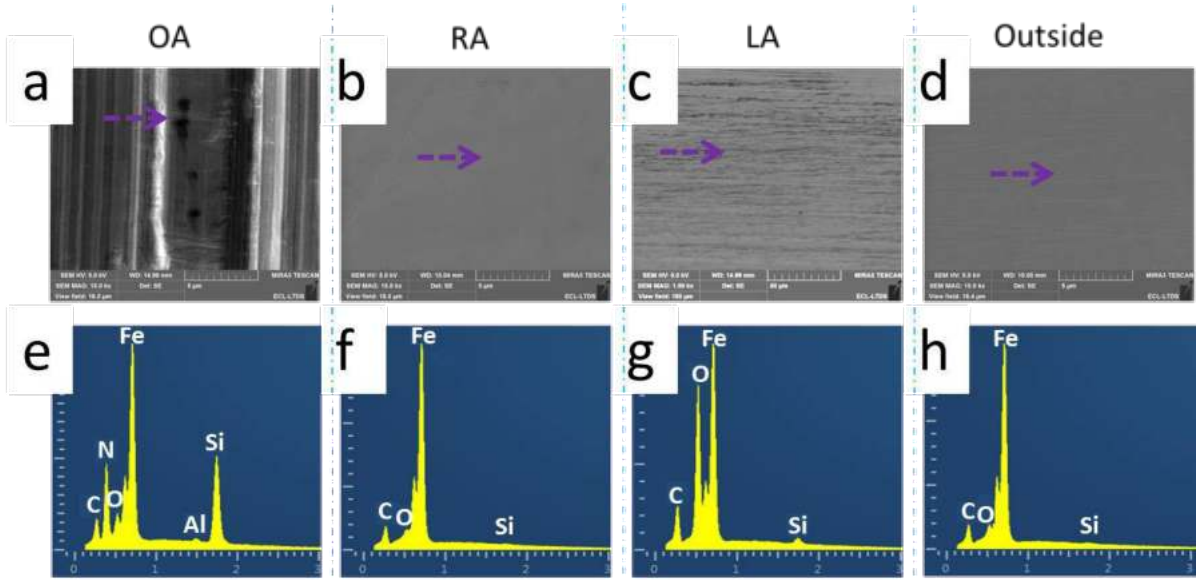

Fig. 2 SEM images and EDS analyses of steel wear scar lubricated by a,e OA b,f RA c,g LA under x15000 magnification, where d,h is an SEM image and EDS analysis of steel outside wear scar. Violet arrows refer to the area analyzed by EDS.

Raman spectra display more precise information on wear particle structure. The spectrum of steel wear scar lubricated by OA shows peaks at 222, 289, 408, and 1315 cm^{-1} (Fig. 3) characteristic of hematite α-Fe_2O_3[3] and a peak at 672 cm^{-1} belonging to magnetite Fe_3O_4[4]. Apart from the iron oxides, carbon G peak representing bond stretching of carbon sp2 atoms[5] is detected at 1586 cm^{-1}. To conclude, wear particles in OA are mainly composed of a-Fe_2O_3, Fe_3O_4, and carbon. Raman data is slightly different from EDS analyses, after all, the electron probe in EDS is much smaller than the photon beam. a-Fe_2O_3 and Fe_3O_4 are also detected in the steel wear particles when lubricated by LA, indicating that iron oxides accumulate on steel surface too. Worn steel surface lubricated by RA shows similar Raman spectra than outside of wear track.

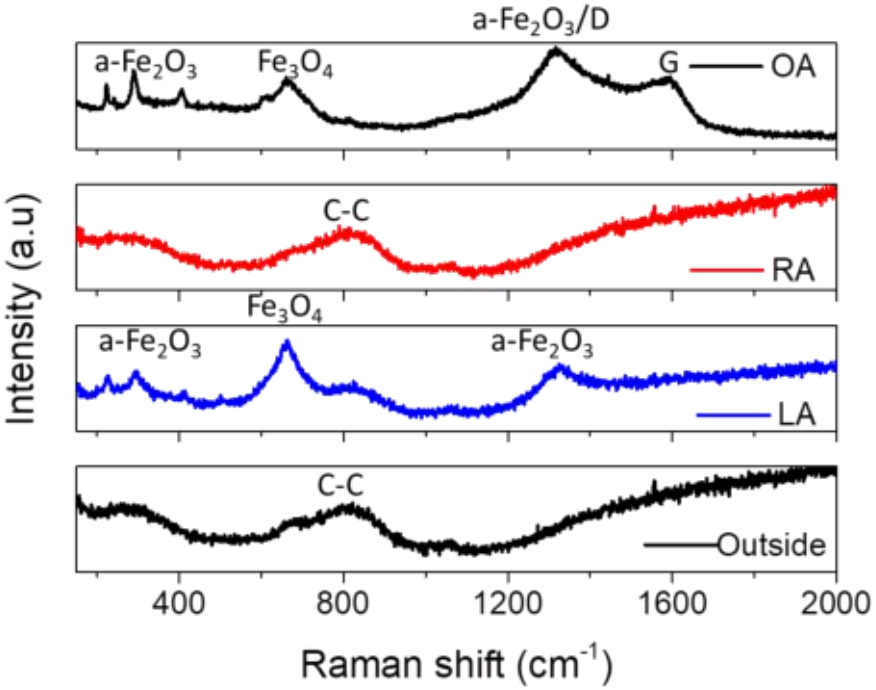

Fig. 3 Raman spectra of steel wear lubricated by OA, RA and LA. Raman spectrum performed outside of wear is also presented for comparison.

XPS is used here to investigate the upmost layer chemistry of steel lubricated by OA and RA. Because steel wear scar lubricated by OA is not homogenous, the part marked in violet is the analyzed area (Fig. 1b). In this area, no Si and N signals are detected and the main components are C, O, and Fe. Compared with the outside of wear scar, oxygen content increases by 4% (Table 4), and this rise in oxygen content is associated with an increase of FeO_x signal. Interestingly, compared with outside steel wear scar and after accurate calibration with iron oxide O_{1s} peak, the position of C-C/C=C shows a 0.2 eV energy shift to lower binding energy suggesting that more C=C signal detected inside wear scar. Fatty acid chains could serve as a C=C source and even if there is only one double bond in the fatty acid chain, this strongly suggests that fatty acid chains are absorbed on wear scar of steel. The absence of O_{1s} photopeak of H_2O at 534.5 eV BE for steel lubricated by oleic acid also suggests that OA chains occupy steel surfaces and modify surface towards hydrophobicity state and therefore, water is not adsorbed on the surface (Fig. 4b). On the contrary, steel lubricated by RA is covered by OH groups and thus conserves water by forming hydrogen bonds (Fig. 4d). These water molecules can originate from the dehydration of the OH-containing alkyl chain of RA, producing another conjugated double bond. This observation is consistent with the fact that RA[6] dissolves in water but OA[7] does not. Moreover, with steel

lubricated by RA, the C-O bond content is twice that of steel lubricated by OA and reaches 6.2%.

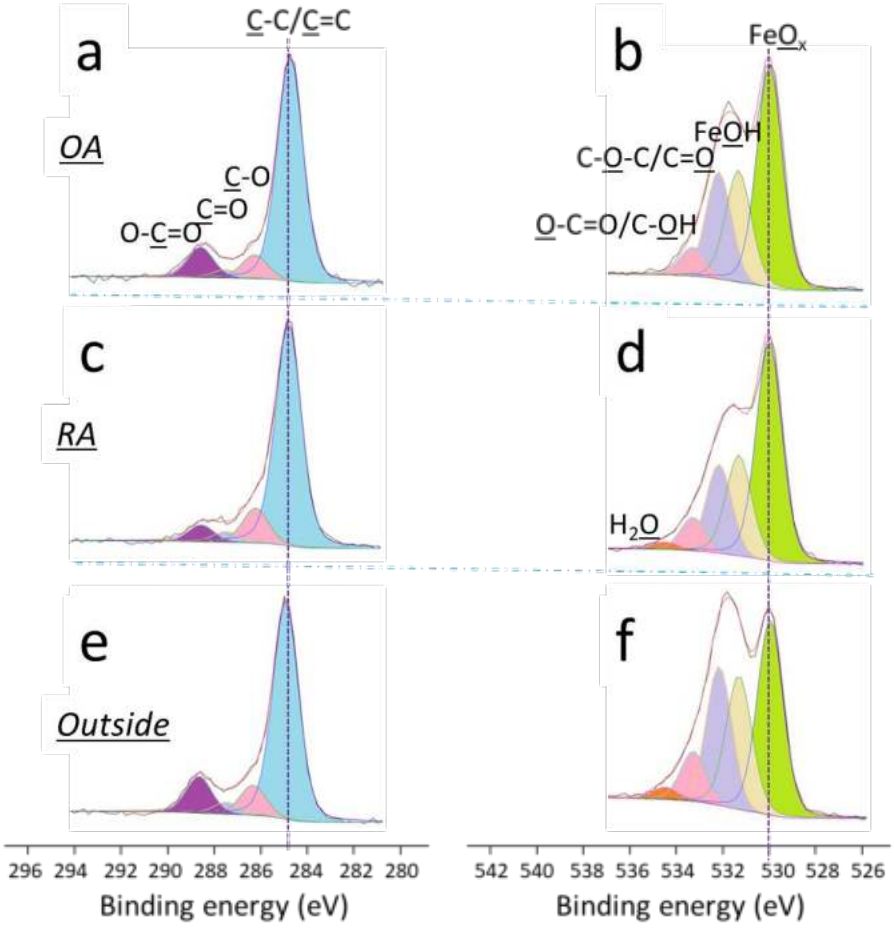

Fig. 4 High-resolution C_{1s} and O_{1s} peaks of steel scar lubricated by **a**,**b** OA **c**,**d** RA. Here, C_{1s} and O_{1s} peaks of outside steel wear are also presented in **e**,**f**, respectively. Spectra are calibrated by indexing FeO_x peak at 530.0 eV[8].

Table 4: Fitting details of XPS on steel.

Steel in OA	C_{1s}				O_{1s}				
Percentage-%	44.3				43.7				
Peaks	C-C /C=C	C-O	C=O	O-C=O	FeO_x	FeOH	C=O /C-O-C	O-C=O /C-OH	H_2O
Positions-eV	284.8	286.3	287.6	288.6	530.0	531.3	532.2	533.3	534.5
FWHM-eV	1.3	1.3	1.3	1.3	1.3	1.3	1.3	1.3	-
Percentage-%	34.7	3.7	1.3	4.6	21.4	9.2	10.3	2.8	-
Steel in RA	C_{1s}				O_{1s}				
Percentage-%	51.8				36.3				

Peaks	C-C /C=C	C-O	C=O	O-C=O	FeO_x	FeOH	C=O/ C-O-C	O-C=O /C-OH	H_2O
Positions-eV	284.9	286.3	287.6	288.6	530.0	531.3	532.2	533.3	534.5
FWHM-eV	1.3	1.3	1.3	1.3	1.3	1.3	1.3	1.3	1.3
Percentage-%	40.7	6.2	1.9	3.0	18.1	8.3	6.7	2.5	0.7
Steel outside	C_{1s}				O_{1s}				
Percentage-%	50.0				39.7				
Peaks	C-C /C=C	C-O	C=O	O-C=O	FeO_x	FeOH	C=O/ C-O-C	O-C=O /C-OH	H_2O
Positions-eV	285.0	286.4	287.5	288.7	530.0	531.3	532.2	533.3	534.5
FWHM-eV	1.3	1.3	1.3	1.3	1.3	1.3	1.3	1.3	1.3
Percentage-%	36.7	5.1	2.0	6.2	15.0	10.2	9.7	3.8	1.0

In summary, RA surpasses the lubricity of OA and LA for steel/Si_3N_4 contact. It avoids not only material transfer by adhesive wear from Si_3N_4 to steel but also prevents large scale accumulation of iron oxides, increasing local roughness. XPS results strongly suggest that RA chains are adsorbed on the steel surface and may dehydrate, producing more doubles bonds. However, having an OH group on the fatty acid chain changes the way of how fatty chains absorb on steel. A simulation is preferred here to understand how the RA molecule is absorbed on steel and why it shows better performance than OA and LA.

6.1.3. Superlubricity

A temperature decrease from 100°C to 80°C in the test result in a sharp reduction of steady CoF from 0.014 to 0.005 in a superlubricious state (Fig. 5), further reduction of the temperature to 60°C leads to a steady CoF of 0.003. Initial CoFs also decrease when decreasing temperature. Being opposite to this tendency, the temperature decrease leads to a significant enlargement of steel wear scar diameter while the steel surface becomes slightly rougher. Nevertheless, the lambda ratios calculated at all temperatures stay below 1 even though liquid film thickness is calculated to be 8.4 nm at 60°C,

From Fig. 5, it is clear that liquid film thickness still plays a role in reducing friction even under boundary lubrication. This could suggest that a liquid film is present between contacts. Considering lambda is less than 1, a complete liquid film is unlikely to be present in contact but a discontinuous liquid film could partially support the load and separate the contact

between asperities. However, previous calculations have shown that any liquid film of RA, even very thin, always provides a friction coefficient below 0.002 (Table 5). However, below 5 nm film thickness, the definition of viscosity in the film is very questionable, because only 2 or 3 molecules are involved in the thickness and both of them are attached at the surface.

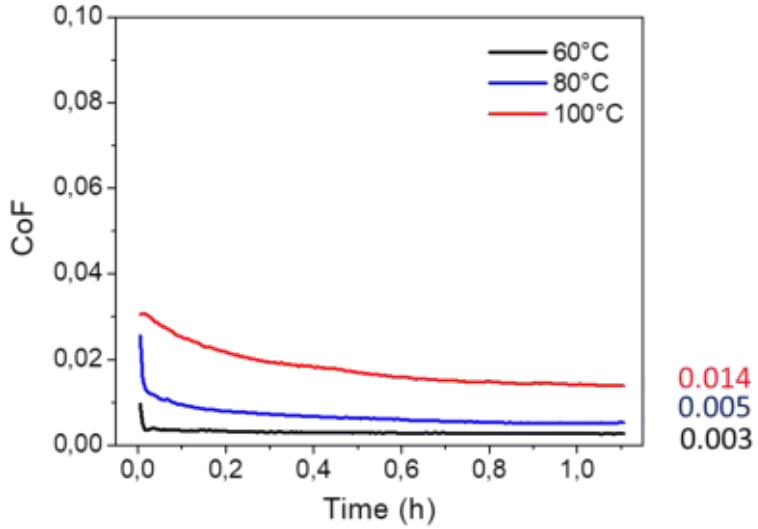

Fig. 5 Friction curve of steel/Si_3N_4 sliding in RA under different temperatures.

Since liquid film partially separates contacts between asperities, the shearing strength between asperities should stay as low as possible. Combining the tribological performances of RA, OA, and the difference between their molecular structures, OH groups in RA fatty chain are found to have the key role to maintain low friction. OH group cannot only form a hydrogen bond network to prohibit interdigitation[9] but also provides easy shear hydrogen terminations [10]. Combining "liquid" nanofilm separation and low friction of OH heads on RA on asperities, superlubricity is achieved (Fig. 6).

Table 5: Summary of film thickness, lambda and information about wear scar after friction. Here, the visco-pressure coefficient of RA is taken as the same value as castor oil[11], which means 12.3 1/GPa at 100°C, 13.5 1/GPa at 80°C, 14.4 1/GPa at 60°C.

	RA-60°C		RA-80°C		RA-100°C	
Theretical CoF of liquid film	2×10^{-3}		10^{-3}		5×10^{-4}	
CoF at 1.1 h	0.003		0.005		0.014	
	Ball	Disk	Ball	Disk	Ball	Disk
Wear diameter -µm	737	-	788	-	810	-
Hertzian diameter-µm	678		678		678	

Wear curvature radius- mm	102.7		106.4		112.1	
Sa before test- nm	5.5	12.4	5.5	12.4	5.5	12.4
Sa after test- nm	6.2	12.4	5.5	12.4	4.9	12.4
Film thickness- nm	8.4		5.8		3.4	
Lambda	0.61		0.43		0.26	

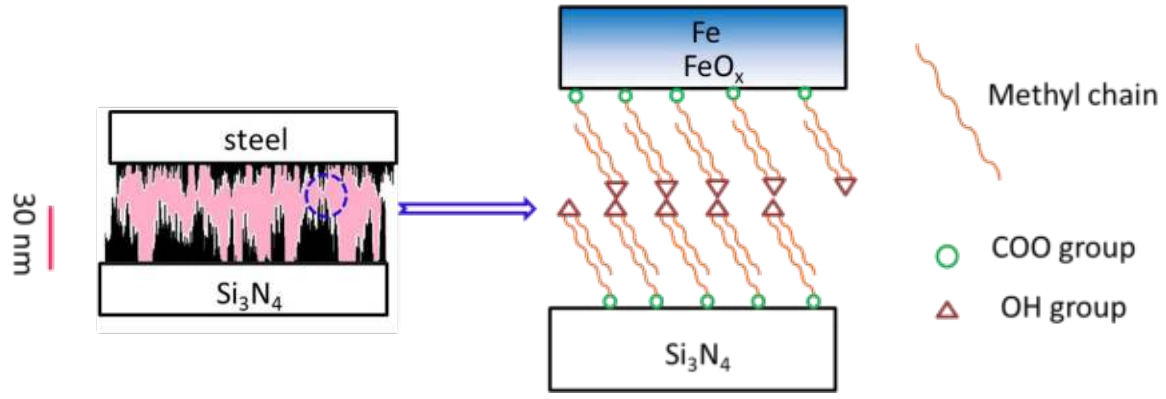

Fig. 6 Superlubricity model of steel/Si_3N_4 lubricated by RA. The peak area on the left graph represents the liquid film of RA. The graph on the right side shows the contact between asperities. It is possible between RA chains on two surfaces, there exists a water layer. However, from our current analysis, the source of water cannot be decided. Further study is required.

6.1.4. Conclusions

This work has demonstrated the superior lubricity of RA over OA and LA for a steel/Si_3N_4 tribo-pair. Under the same viscosity, replacing OA, LA by RA cut down friction by a 2/3 ratio. The low friction of RA is accompanied by the generation of homogenous and smooth wear. This tremendous difference between RA and other fatty acids originates from its unique hydroxyl group, possibly acting as low 'friction brushes'. Cooperating with suitable nanometer-thick liquid film, superlubricity has been achieved when the temperature is below 80°C.

6.2. References

[1] Rabelo, J., Batista, E., Cavaleri, F. V. W., & Meirelles, A. J. (2000). Viscosity prediction for fatty systems. *Journal of the American Oil Chemists' Society*, *77*(12), 1255-1262.

[2] André, E., & Vernier, C. (1932). Some Physical Properties of Pure Ricinoleic Acid: The Refractive Index, Specific Gravity, and Viscosity. *Journal of Rheology (1929-1932)*, *3*(3), 336-340.

[3] Sirivisoot, S., & Harrison, B. S. (2015). Magnetically stimulated ciprofloxacin release from polymeric microspheres entrapping iron oxide nanoparticles. *International journal of nanomedicine*, *10*, 4447.

[4] Molchan, I. S., Thompson, G. E., Lindsay, R., Skeldon, P., Likodimos, V., Romanos, G. E., ... & Schubert, T. J. (2014). Corrosion behaviour of mild steel in 1-alkyl-3-methylimidazolium

[5] Ferrari, A. C. (2007). Raman spectroscopy of graphene and graphite: Disorder, electron–phonon coupling, doping and nonadiabatic effects. *Solid state communications*, *143*(1-2), 47-57.

[6] Seidell, A. (1941). Solubilities of Organic Compounds. New York: D. Van Norstrand Co.

[7] EPA, U. (2010). Estimation Program Interface (EPI) Suite.

[8] Biesinger, M. C., Payne, B. P., Grosvenor, A. P., Lau, L. W., Gerson, A. R., & Smart, R. S. C. (2011). Resolving surface chemical states in XPS analysis of first row transition metals, oxides and hydroxides: Cr, Mn, Fe, Co and Ni. *Applied Surface Science*, *257*(7), 2717-2730.

[9] Ewen, J. P., Gattinoni, C., Morgan, N., Spikes, H. A., & Dini, D. (2016). Nonequilibrium molecular dynamics simulations of organic friction modifiers adsorbed on iron oxide surfaces. *Langmuir*, *32*(18), 4450-4463.

[10] Long, Y., Bouchet, M. I. D. B., Lubrecht, T., Onodera, T., & Martin, J. M. (2019). Superlubricity of glycerol by self-sustained chemical polishing. *Scientific reports*, *9*(1), 1-13.

[11] Stachowiak, G., & Batchelor, A. W. (2013). *Engineering tribology*. Butterworth-Heinemann.

Chapter VII

7.Summaries and perspectives of Ph.D. work

Table 1 shows tribological systems tested in this work that can reach superlubricity. Superlubricity was not observed with other ceramic materials like ZrO_2, Al_2O_3, SiO_2 in glycerol…….and data are not provided in this manuscript.

Table 1: Experimental conditions of superlubricity achieved in this Ph.D. work. V represents the lubricant volume, T temperature, P_{max} initial Hertzian contact pressure. $P_{average}$ stands for average contact pressure calculated at the end of the test after measuring wear scar areas. v is sliding speed. For ta-C(x), x is the measured hardness. Lambda is the ratio between liquid film thickness and composite roughness.

Tribo-pair Pin/disk	Lubricant	LV-µL	T-°C	P_{max}-MPa	$P_{average}$-MPa	v-mm/s	Lambda	**CoF**
Steel/aC:H	-	-	24	565	-	0,2	-	**0,010**
aC:H/aC:H	-	-	24	565	-	0,2	-	**0,006**
SiC/aC:H	-	-	24	565	-	0,2	-	**0,004**
Si_3N_4/aC:H	-	-	24	565	-	0,2	-	**0,003**
The first 4 cases are conducted in ultra-high vacuum with a pressure of 500 nPa.								
Steel/ta-C Hardness(ta-C):55GPa	Glycerol	50	50	577	264	3	0,93	**0,004**
Steel/SiC	Glycerol	50	50	598	112	3	0,40	**0,007**
Steel/SIC	Glycerol+0.3 wt%hypericin	50	50	598	144	3	0,14	**0,009**
			80	598	89	3	0,17	**0,007**
Si_3N_4/ Si_3N_4	Glycerol	50	120	750	99	3	0.40	**0.009**
			150	750	80	3	0,26	**0.006**
a-C/ Si_3N_4 Hardness(a-C):30GPa	Castor oil	50	100	295	148	3	0,67	**0.005**
					151	1.5	0,39	**0.01**
ta-C/ Si_3N_4 Hardness(ta-C):55GPa	Castor oil	50	100	295	170	3	0,62	**0,008**
Steel/a-C Hardness(a-C):30GPa	Castor oil	50	100	295	179	3	0.45	**0,004**
Steel/ Si_3N_4	Ricinoleic acid	50	60	295	166	3	0,61	**0,003**
			80	295	146	3	0,43	**0,005**

7.1. Vacuum

In a vacuum, superlubricity can only be achieved if one side of the friction pair is covered by aC:H coating. The hydrogen content inside a:C:H coating has a key role to keep superlubricity for a long time. In this thesis, aC:H sample contains 36 atomic % of hydrogen. All counter-parts (aC:H, steel, SiC, and Si_3N_4) can be used to reach superlubricity. For Si_3N_4/aC:H tribo-pair, a nano-meter thick carbonaceous layer is detected on Si_3N_4 after friction. Superlubricity is established by sliding two highly-hydrogenated graphitic carbon surfaces after a film transfer (Fig. 1). No evident surface polishing is observed.

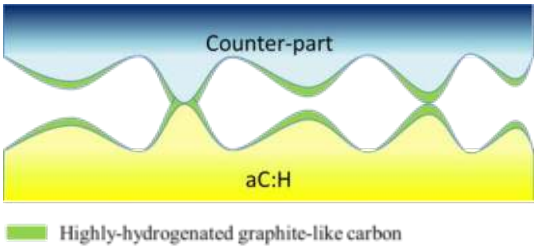

Fig. 1 Schematic image of superlubricity in a vacuum.

7.2. Glycerol

Glycerol has demonstrated excellent lubricity for a long time. It is first attributed to its perfect Newtonian behavior and an amazing low viscosity-pressure coefficient that ensures weak shear strength of glycerol EHL film. This situation is very well described by the thermal EHL theory and such systems can provide friction coefficient well below 0.01 in polished steel/steel configuration. However, when the glycerol liquid film is thinner at the nm scale, the situation becomes more complex and surprising. In this case, solid contacts take place between asperities and, with the help of dissolved dioxygen, glycerol is chemically decomposed in a myriad of oxygenated products including aldehydes, acids, quinones, etc. Water can also be generated in the contact. These degradation compounds can attack the substrates producing chemical wear and polishing effect mainly on the ball surface that is always in contact. Interestingly the polished worn area is not flat but has a radius of curvature well higher than the radius of the ball. (Fig. 2). This case is very different from high-speed tests using Si-based ceramics with water described in the literature. In this latter case, huge chemical wear leads to a collapse of the contact pressure down to the MPa range, and lubrication is simply provided by hydrodynamic lubrication of water mixed with colloidal silica. Similar properties have been reported of water-lubricated ceramics but at high sliding speed ($\geq$ 60 mm/s)[1,2,3]. It is important to highlight that at 3 mm/s sliding speed, water cannot polish Si_3N_4 and surfaces are becoming rougher and rougher after friction (result not presented in this thesis). In all our tests, the apparent contact pressure stays above 100 MPa (see table 1), and wear is low (wear rate per meter less than 600 $\mu m^3/m$). The calculated EHL film thickness is typically in the range of 2-5 nm and lambda ratios are well below unity. Now a question is rising: except for the test of steel/ta-C in glycerol where lambda is around 1[4]; can we ignore the possibility of a nm-thick EHL film lubrication in all other tests. For steel/SiC

and Si_3N_4//Si_3N_4 contacts in glycerol, lambda is around 0.3 and superlubricity is achieved. Taking a glycerol molecule size of 0.62 nm, a 2-nm thick EHL film would be only 3 molecule-thick (including two adsorbed layers). In these conditions, the viscosity of the trapped fluid has no meaning, and molecules are immobile and cannot stay in a liquid state[5]. For example, for steel/SiC in glycerol at 50°C in a steady-state regime, superlubricity can be achieved and frictionless species like silica and graphitic materials are detected. But increasing temperature up to 120°C results in a sharp rise of friction. Furthermore, no graphitic materials are observed and the content of silica becomes negligible.

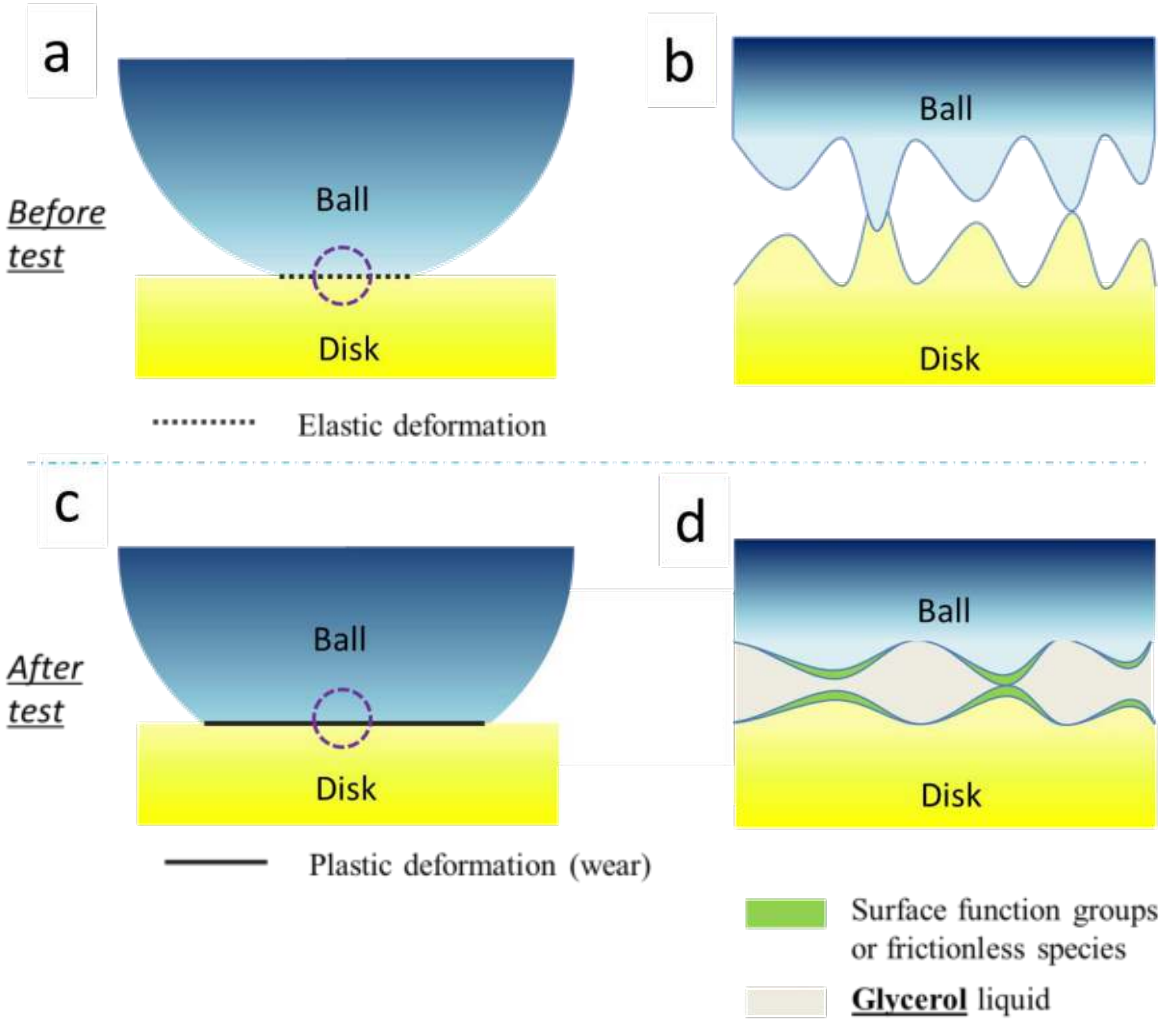

Fig. 2 Schematic pictures of superlubricity realized by glycerol: **a** tribo-pair contact before sliding, **b** contact between asperities with plastic deformation a, **c** tribo-pair contact when superlubricity is established, **d** contact between asperities at the end. The wavelength of roughness has changed and the contact remains more in elastic conditions.

Apart from the polishing of the contact area, another interesting effect takes place concerning the roughness. Most of the time the roughness level decreases but more interestingly the slope of asperities decreases also so that the surface asperities are less sharp (see Fig 2d compared with Fig 2b).

Setting aside the two advantages mentioned above, glycerol is capable to functionalize the upmost surface by tribochemical reactions. Since it is rich in OH groups, it can terminate the steel surface atoms with FeOOH, a low friction lamellar species. In suitable conditions, SiC surfaces are finished by silica layers. Most strikingly, glycerol can react with Si_3N_4 to generate aromatic frictionless CN species.

7.3. Glycerol+hypericin

In the end, thanks to the polarity of glycerol, hypericin can dissolve in glycerol. With the help of glycerol, hypericin can flow into the contact zone and stay. A great affinity between hypericin and steel has been witnessed while lubricated by glycerol+hypericin mixture. The presence of hypericin can easily be confirmed by Raman on steel. On the other hand, with a suitable condition, glycerol does not exclude graphite out of the contact zone. This makes it an ideal solvent and carrier for carbon species.

7.4. Castor oil

Similar to glycerol, the low viscosity-pressure coefficient of castor oil can also limit the shear strength in the liquid film. Synergy has been found between castor oil and ta-C in realizing superlubricity: in castor oil, carbon atoms of the upmost layer of ta-C can rehybridize into sp^2 carbon (Fig. 3b). Friction is drastically reduced due to this highly sp^2 hybridized carbon layer probably covered itself with castor oil fragments.

It is worthy to mention that ta-C is necessary to achieve superlubricity in castor oil. This is probably due to the presence of long fatty acid chains that cannot chemisorb on the ta-C surface while materials like aC:H or steel easily react with fatty acids. Therefore, the inter-digitalization of methyl groups is avoided with ta-C. This assumption required further confirmation.

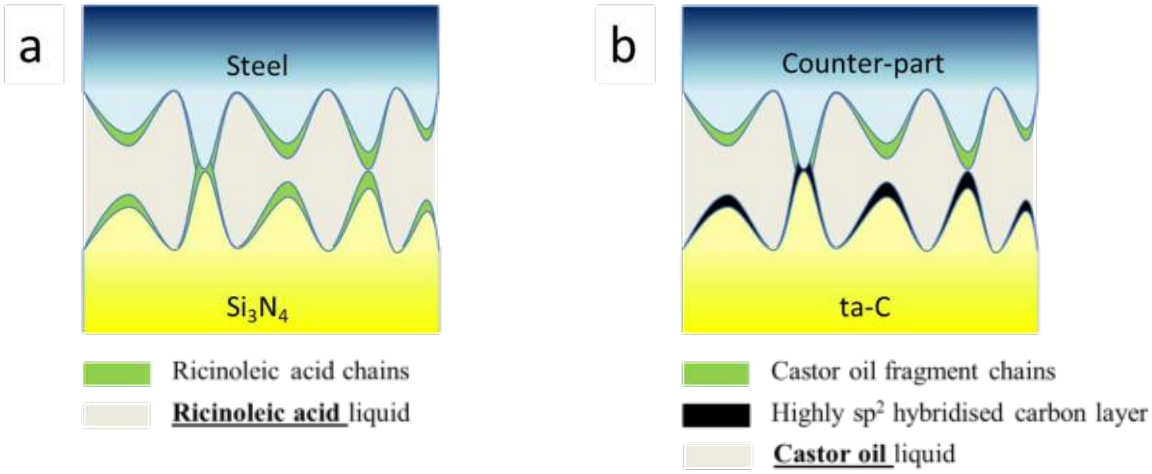

Fig. 3 Schematic image of superlubricity realized by: **a** ricinoleic acid **b** castor oil

7.5. Ricinoleic acid

Superlubricity can be achieved by sliding steel/Si_3N_4 tribopair lubricated by ricinoleic acid. Comparing its performance with oleic acid in the same conditions, it appears that OH groups present in ricinoleic acid are essential for reducing friction. A possible explanation has been given: shearing occurs on OH groups between ricinoleic acid chains (Fig. 3a) whereas shearing occurs between methyl groups with oleic acid.

7.6. General mechanism

This thesis is always guided by the idea that shearing would better take place between frictionless lamellar species. Following this idea, superlow friction cases can be sorted into 2 types:

- Substrates themselves contain frictionless species like highly hydrogenated aC:H. In this scenario, the key to maintaining friction is to find a suitable environment for hydrogen to function and ultrahigh vacuum is needed for aC:H. In terms of tribo-pair, as long as aC:H is on one side, the other side can be either steel, SiC, Si_3N_4, or aC:H. Another case is SiC samples used in this study, which contains some graphitic materials embedded in the structure. Unfortunately, they are located inside holes of SiC and they don't have direct access to the contact surfaces. Thanks to glycerol, graphitic materials are brought into contact and reduce friction between asperities. Here, glycerol also facilitates the growth of the silica layer on SiC.

- For materials that don't have frictionless species themselves. In this case, the in-situ formation of frictionless species or low friction function groups is required. Starting with frictionless species, through a tribo-chemical reaction between glycerol and Si_3N_4, graphene-nitride nanolayers are formed on Si_3N_4, which passivates Si_3N_4 surfaces and make sure that contacts take place between graphene-nitride nanolayers. Surface passivation can be also realized by adopting a-C instead of ta-C in castor oil and this because sp^2 -rich carbon surface not only prohibits the formation of interfacial C-C bond [6] but also provides more active sites for castor oil fragments to occupy respecting to sp^3 rich carbon surface. As for low friction function groups, OH groups are certainly beneficial for decreasing friction no matter it exists in the form of FeOOH or on the aliphatic chain of the fatty chain. For instance, for self-mated FeOOH, no orbital overlap will occur between them thanks to its hydrogen heads.

It's noteworthy that all superlubricity cases reached in this study are accompanied by the generation of ultra-smooth surfaces and no solid wear debris (some surfaces are naturally smooth but others are polished during shear). The case of hypericin is an exception. The lubricant can still play a role in boundary lubrication but does not resemble full liquid film separation (EHL lubrication). Certain amounts of lubricant may be still necessary to activate tribo-chemical reaction and full surface passivation in this region.

7.7. Perspectives

This thesis has identified several favorable scenarios for reaching liquid superlubricity:

1. **Introducing nm-thick liquid film into contact.**
   Based on a statistic point of view, solid contacts among asperities serve as the main cause of friction under boundary lubrication. However, thanks to both surface polishing and enlargement of curvature radius of the ball in the contact area, it is now feasible to extend boundary lubrication regime to mixed or elasto-hydrodynamic ones where the benefit of nanometer-thick liquid film becomes significant. Unfortunately, enlargement of wear curvature radius also leads a rise in wear volume. However, by realizing sustained surface polishing, liquid film can enter contact surfaces with reasonable wear volumes. Moreover, *in situ* polishing doesn't require extra sample preparation and is preferred for practical use. In this thesis, glycerol fluid, *also called viscous water*, has shown excellent polishing ability for steel and ceramics materials.

At the opposite, ethylene glycol or water isn't able to polish steel and ceramics under the same conditions. The mystery of glycerol polishing mechanism requires further investigation in particular to better understand the role of decomposition products.

2. **Forming OH-terminated top surfaces.**

   In fact, nascent surfaces of steel, SiC, Si_3N_4 contain some OH functions on their extreme surface before friction. However, friction will rapidly remove them because wear depths in our tests are around dozens of nanometers. Thus, the ability to *in situ* form a maximum of H-/OH functions in the wear scar is crucial for decreasing friction. This thesis demonstrates that lubricants such as glycerol, castor oil and ricinoleic acid molecules which naturally contain OH functions favor the saturation of the dangling bonds generated across the interfacial zone by OH bonds. Even though superlubricity realized by OH functions is still influenced by experimental conditions, their presence on surfaces drives superlubricity to be achieved when lambda is well below unity.

3. **Forming frictionless 2-D species on surfaces**.

   Frictionless 2-D species were generated by either tribochemical reaction between glycerol and Si_3N_4 or rehybridization of sp^3 carbon into sp^2 carbon for DLC. Even though sp^2 carbon content is crucial for tribological performance of DLC, the increase of C=C/C-C ratio in fatty acid chain doesn't always have a positive effect on friction reduction. For instance, at the same viscosity of lubricants, steel/DLC lubricated by linoleic acid shows a higher CoF than the one lubricated by oleic acid.

This work has exhibited the advantage of *in situ* forming nitrogen containing aromatic species, where Si_3N_4 acts as the nitrogen source. It is intriguing to check if other nitrogen source like CN_x coating, melamine can react with glycerol and form graphene nitride layer.

On the other hand, castor oil cooperating with DLC has shown an extremely low friction. Other vegetable oils like olive oil, coconut oil, sunflower oil etc. are also worthy to be studied.

In terms of surface polishing, even though water doesn't polish steel and ceramics in our conditions, it would be interesting to test mixtures of glycerol.

7.8. References

[1] Chen, M., Kato, K., & Adachi, K. (2001). Friction and wear of self-mated SiC and Si3N4 sliding in water. *Wear*, *250*(1-12), 246-255.

[2] Ferreira, V., Yoshimura, H. N., & Sinatora, A. (2012). Ultra-low friction coefficient in alumina–silicon nitride pair lubricated with water. *Wear*, *296*(1-2), 656-659.

[3] Jahanmir, S., Ozmen, Y., & Ives, L. K. (2004). Water lubrication of silicon nitride in sliding. *Tribology Letters*, *17*(3), 409-417.

[4] Long, Y., Bouchet, M. I. D. B., Lubrecht, T., Onodera, T., & Martin, J. M. (2019). Superlubricity of glycerol by self-sustained chemical polishing. *Scientific reports*, *9*(1), 1-13.

[5] Baudry, J., Charlaix, E., Tonck, A., & Mazuyer, D. (2001). Experimental evidence for a large slip effect at a nonwetting fluid− solid interface. *Langmuir*, *17*(17), 5232-5236.

[6] Bouchet, M. I. D. B., Martin, J. M., Avila, J., Kano, M., Yoshida, K., Tsuruda, T., ... & Asensio, M. C. (2017). Diamond-like carbon coating under oleic acid lubrication: Evidence for graphene oxide formation in superlow friction. *Scientific reports*, *7*(1), 1-13.